AN EIGHT TESLA SUPERCONDUCTING MAGNET FOR CYCLOTRON STUDIES

By

Jong-Won Kim

A DISSERTATION

Submitted to
Michigan State University
in partial fulfillment of the requirements
for the degree of

DOCTOR OF PHILOSOPHY

Department of Physics and Astronomy

1994

ABSTRACT

8 TESLA SUPERCONDUCTING MAGNET FOR CYCLOTRON STUDIES

By

Jong-Won Kim

Superconducting magnets have become broadly used for cyclotrons due to advantages of compactness and lower operation costs compared to conventional magnets. To gain benefits of higher magnetic fields beyond the 5 tesla cyclotron magnets which are under operation in several laboratories including the MSU/NSCL, a test magnet which can produce fields higher than 8 tesla was constructed. Our goal was to develop the coil construction technique, to use the magnet as a test stand, and to pursue a conversion to a cyclotron in the future.

The basic magnet design has the characteristics of a superconducting isochronous cyclotron. Because of the large magnetic forces in high field coils, the coil design has been intensively studied with computations and experiments. When construction was completed, the magnet proved to produce fields higher than 8 tesla at 4.4 K. Magnet properties such as spring constants of link assemblies and magnetic off-centering forces, magnet inductances, and heat leak to 4 K were measured and compared with computations. Magnetic fields were also measured along a radial line at a fixed angle, and compared to 3-d field calculations made with the TOSCA program.

Using the 8 tesla magnet to generate a broad range of radially flat fields from 2 to 8 tesla, emittance measurements of an internal ion source would be possible in the

magnet's center region. Computations were made to yield a possible experimental scheme for the measurement.

An eventual use of the 8 tesla magnet could be a conversion to a cyclotron. In the design study presented in the appendix, the 8 tesla magnet is assumed to accelerate deuterons in a central field of 7.2 tesla. This would yield a deuteron energy of 35 MeV, i.e. a cyclotron K value of 70 MeV. To utilize the maximum field produced by the 8 T magnet (~8 tesla), an ion with a lower Q/A such as He^+ has been suggested as a design particle, yielding a K value of approximately 90 MeV.

ACKNOWLEDGMENTS

The 8 tesla magnet was completed by the collective effort of the NSCL accelerator group. Credit for the successful completion is due to each person who has been involved in the project. Most of all, Guenter Stork deserves a great deal of my appreciation for his skillful magnet design and assembly. The machine shop personnel have also been a great help throughout the project.

Prof. Henry Blosser, who initiated this project and has supervised all the way with his great enthusiasm, has influenced my life as well as this project. His advice and encouragement during my thesis project are very much appreciated. It is also a pleasure to acknowledge my gratitude to Dr. Albert Zeller who joined this project at the beginning, and has given much valuable advice.

I want to thank Dr. Felix Marti, Mr. Dave Johnson and Prof. Mort Gordon for many invaluable discussions during the cyclotron group meetings. In addition, I am indebted to Prof. Jerry Nolen, Prof. Aaron Galonsky, Prof. Michael Dubson, and Prof. Julius Kovacs for their comments and help on my thesis as guidance committee members. Fellow graduate students, Leung-Sheng Lee and Jeff Schubert, have been greatly helpful in the construction of the 8 tesla coils. Special thanks go to colleagues in the accelerator group, Jim Bailey, Dong-o Jeon, Bo Zhang for fruitful conversations and discussions about accelerator physics and our future. Finally, my family and relatives deserve my greatest thanks for their constant love and support.

Contents

List of Tables

List of Figures

Chapter 1

Introduction

With the advent of superconducting magnet technology, cyclotrons have become more compact and more cost effective by using much higher magnetic fields than previous room temperature cyclotrons. Present superconducting cyclotron magnets use an 'average' field[1] of about 5 tesla [Tri90] compared with 1-2 tesla fields for room temperature cyclotrons. Construction costs as well as operating costs have been reduced approximately 50% by this doubling or tripling of the average field strength along with the resulting 10 to 20 fold reduction in magnet weight. A further field increase from 5 to 8 tesla is likely to yield a similar benefit. This will, however, entail tighter tolerances resulting from smaller space, and will thereby bring more challenges in design and construction of cyclotron subsystems. The use of 8 tesla in a future cyclotron will be a significant step in the development of smaller, and less costly cyclotrons.

The major goal of this project is to construct a magnet which would operate reliably at 8 tesla with a general structure appropriate for an isochronous cyclotron. The Harper hospital cyclotron, using a current density of 13,000 amp/cm^2 at approximately 5 tesla, is a present landmark in this direction [Blo89]. The selection of 8 tesla rather than some higher fields is due to the critical current limit of the NbTi superconductor at 4.2 K. To achieve even higher fields (as in the 10 tesla magnets

[1] 'average' field is the azimuthal average of the magnetic field at a given radius

of the LHC at CERN [Kat90]), one would need to move to a different basic magnet concept involving either: 1) a complicated cryogenic system to reduce the operating temperature to 1.8 K, or 2) Nb_3Sn superconductor at 4.2 K. Both of these alternatives would likely cost substantially more than the well established NbTi technique at 4.2 K. Therefore, 8 tesla has been selected as the goal of the present project.

The 8 tesla magnet, shown schematically in Figure 1.1, has been designed to serve both as a cyclotron and as a multipurpose test stand to study cyclotron related phenomena. This thesis presents details of the design and construction of a superconducting magnet, and the measurements of its properties and fields. Future uses of this magnet as a cyclotron and as an emittance measuring apparatus are described in the appendix.

The design process for this magnet involved many numerical studies of possible alternative configurations of coil and magnet as described in chapter 2. Calculations of magnetic fields and forces in the coil were used to compare the advantages of different options, and the design parameters were finalized.

High field superconducting coils demand a careful evaluation of coil stresses. Maximum stresses have been calculated and reduced to an acceptable level using preloads on the superconductor and on the banding. In particular, tensile and shear stresses were reduced so that quenches induced by large stresses were avoided.

The coil shape was fully determined after magnetic fields and stress calculations were completed, and then dimensions and maximum operating current of the superconductor were selected. Quench simulations and hardware considerations were undertaken simultaneously to ensure that the design parameters are acceptable.

As the computational study progressed, the mechanical magnet design was begun based on previous experience in construction of superconducting cyclotrons. Some

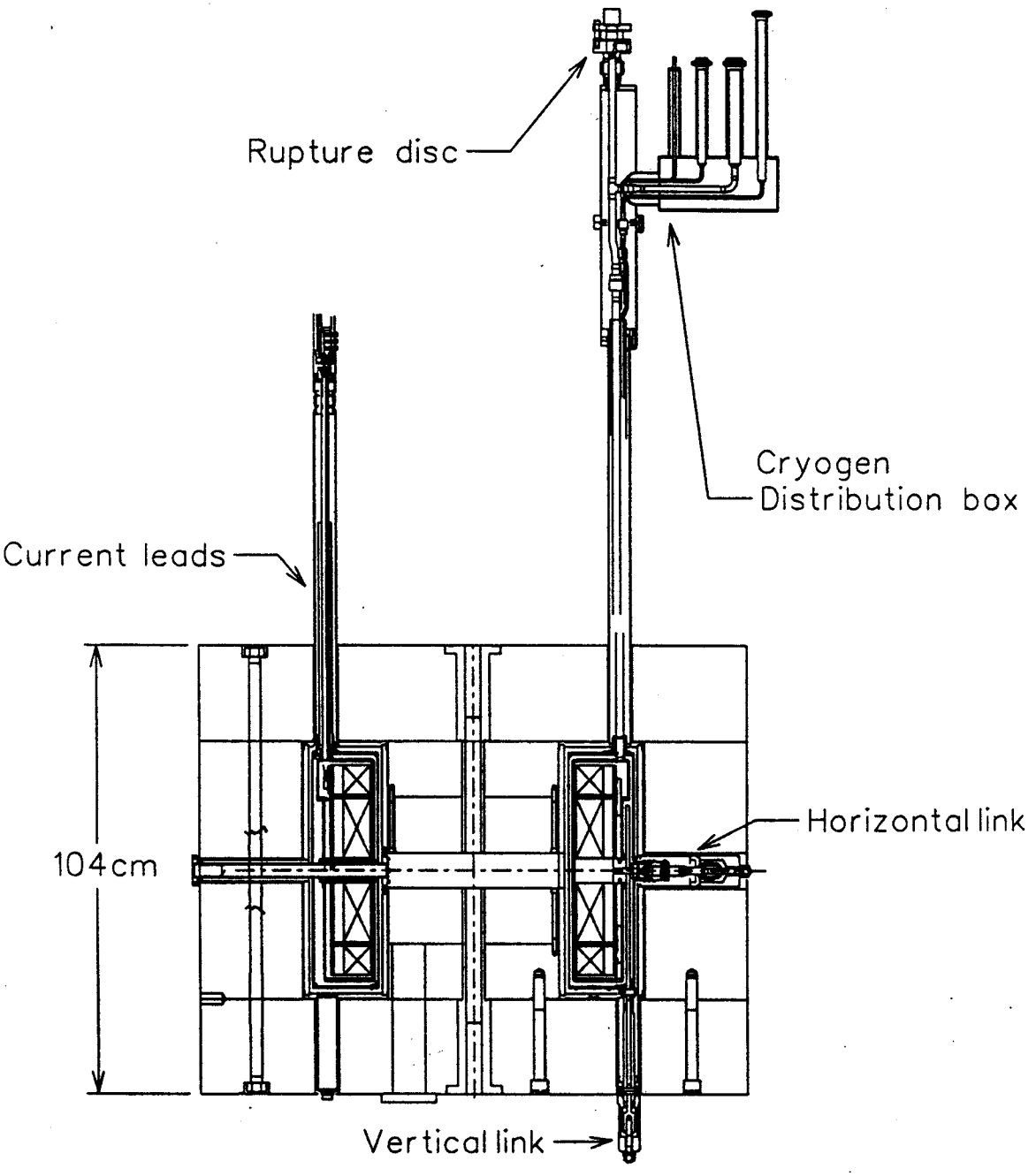

Figure 1.1: A schematic view of the 8 tesla magnet. Some details of the mechanical design as a superconducting magnet are shown.

prototype components such as support links were experimentally tested to obtain the optimal design configurations.

Coil winding was one of major works in this project. Coil failures due to mistakes in the winding process have not been unusual in the history of superconducting magnets [Gre81][Des79]. After a few months of preparations, it took about two months to complete the winding of all four coils. The coils were then tested in a large commercial liquid helium (LHe) dewar to find possible faults in the winding process. Both small and large coil pairs worked properly. The test was an important step in moving the project forward. In chapter 3, details of the construction of the 8 T magnet, its test, and features of magnet system are presented.

After completing the magnet assembly, properties such as spring constants of support links and magnet inductances were measured, as described in chapter 4. The magnetic field was mapped for different excitations. The measurements were made at a fixed angle, and were compared with 3-D calculations by TOSCA [Tos]. Field measurements and their analyses are provided in chapter 5.

A possible first use of the magnet may be to measure ion source emittance using the radiofrequency (rf) extraction in a broad field range of 2-8 tesla. Preparing for that, some computations have been made, and also a rf resonator to extract ions from the source has been tested. These results are presented in the appendix. The central region of the emittance test assembly is designed to spread the beam for differing rf starting times. A three slit system could then roughly distinguish three parameters: rf starting time (τ), and radial phase space (r,p_r). Complications, however, related to initial ion energy and plasma meniscus require some experimental data before the present slit system described in the appendix is further optimized. Calculations in the appendix could serve as a guide for future computational and experimental studies of ion source emittance measurements.

A preliminary study of possible conversion of the 8 tesla magnet to a cyclotron is also presented in the appendix. A single particle and fixed energy machine is assumed in computations. A deuteron was used as a projectile, and the central region of the 8 tesla magnet was designed to operate at the third harmonic of the cyclotron frequency in a central field of 7.2 tesla with 50 kV dee voltage.

Chapter 2

Design of the 8 tesla magnet and its components

The design studies of the 8 tesla (T) magnet are presented in this chapter. Several magnet design options are compared to show their pros and cons. In parallel with the computations, experimental tests have been performed on magnet components to obtain realistic design parameters.

I Initial Design Considerations

A Design parameters of the 8 T magnet

The 8 tesla field was adopted due to the fact that the current density in a NbTi coil at higher fields is severely limited (assuming the NbTi superconductor is used at 4.2 K; the peak field in the conductor is 7.9 tesla when the peak field in the magnet gap is 8 tesla). The critical current of typical NbTi superconductors drops nearly 50% when the field increases from 8 to 9 tesla (for instance the critical current of the 8 T magnet conductor at 4.2 K is 650 A at 8 tesla, and 360 A at 9 tesla). To show economical reasons of choosing an 8 T magnet, cost comparisons for 7 T, 8 T, and 9 T magnets are made in Table 2.1, including the costs of the yoke and of the superconductor. The following is assumed in calculations: (1) the magnetic rigidity is fixed to be 1.5

Table 2.1: Cost comparisons of the 7 T, 8 T, and 9 T magnets

Magnet	J (average in coil)	Yoke	Superconductor	Total cost
7 T	17,000 A/cm^2	8.7 ton, \$ 35 k	39,000 ft \$ 32 k	\$ 67 k
8 T	12,400 A/cm^2	8.0 ton, \$ 32 k	46,000 ft \$ 37 k	\$ 69 k
9 T	7,300 A/cm^2	10.7 ton, \$ 43 k	63,000 ft \$ 50 k	\$ 93 k

tesla·m, (2) the yoke thickness is determined by the requirement of the same fringe field at the yoke edge. (3) the maximum current is 400 A for all three magnets. The material costs to build a 9 T magnet are sharply increased from the cost of an 8 T magnet, and a 7 T magnet is less compact than an 8 T magnet.

The pole radius is about 20 cm which is convenient to accommodate the diagnostic devices for beam studies. This radius will also allow the magnet to become an interesting nuclear physics cyclotron in the future. The cyclotron K_b at 20 cm and 8 tesla is approximately 100 MeV so that E/A for Q/A=0.25 is 6 MeV/n. A cyclotron of this energy range would be a useful tool for studying high angular momentum states in nuclei using heavy ion reactions [Nuc].

The basic coil structure is a layer type winding without connection joints inside the coil. There are in total four coils: two small and two large. A small coil pair is serially connected, and so is the large coil pair, in order to produce the median plane symmetry. The resulting two current system allows the small and large coils to be independently energized as in other cyclotrons (K1200, K500, Agor, Chalk River, etc.) to obtain different field shapes from different coil excitations. This field shaping by using different current ratio on the two coils is a unique feature of superconducting cyclotrons; which allows them larger dynamic range than conventional room temperature cyclotrons for different ions and their energies. The superconducting coils are potted with epoxy which results in compactness and high current density. The sta-

Table 2.2: Design parameters of the 8 T magnet

Coil	total four coils: two small and two large coils potted with Stycast 2850 FT, 48 layers for each coil large coil : 2904 turns, small coil : 1363 turns Cu/NbTi= 1.9, bare wire : 1.0 × 2.1 mm
Banding	304 stainless steel wire, 1.1×2.0 mm 2.35 cm thick overall Clam shell on the outside of the banding: 3 segments of solid 304 stainless steel, 0.58 cm thick
Current	400 A for both coils at 8.2 tesla J_{large}= 13,028 amp/cm^2, J_{small}=12,434 amp/cm^2
Pole	radius= 21.2 cm, pole gap= 8.1 cm
Yoke	1020 SAE steel, 8 tons, radius=63.8 cm, height=104 cm

bility of potted coils at 8 tesla is a main concern of this project. Because of the high stresses, stainless steel is used on the outside of the coils to reinforce the coils. The magnet has a pillbox type yoke as in many superconducting cyclotrons. The overall design parameters of the 8 T magnet are displayed in Table 2.2.

The maximum current density of superconducting wire depends on manufacturing technology as well as on inherent critical currents of superconductors. The critical current density of some round NbTi wires is larger than 40,000 amp/cm^2 (average in conductor, Cu/Sc ratio=1.6) at 8 tesla, 4.2 K [Als]. However, a maximum operating current of about 20,000 amp/cm^2 (average in conductor) at 8 tesla, 4.4 K was chosen after considering the design current density of other working magnets. The maximum current of 400 A at 8 tesla was decided according to considerations such as heat leakage and magnet inductances as described in section 2.I.K.

B Magnetic fields

The field profiles need to be defined to determine the specific coil configuration. The ion source emittance measurement, which is planned to be one of the first uses of the

magnet, works optimally with a radially flat magnetic field in the required range of 2-8 tesla. In addition, the isochronous fields for heavy ions are nearly flat (a final energy of 6 MeV/n needs only a 500 gauss increase at a full radius of ~20 cm when the center field is 8 tesla). The magnetic fields can also be further shaped by manipulating pole tip configurations in conjunction with the two coil currents as in other isochronous cyclotron magnets.

Compact superconducting cyclotrons basically have split solenoid coils with median plane symmetry, and two image coils are serially connected (room temperature penetrations for the beam and for diagnostic elements must pass through the coil at the solenoid split). A single current system is suitable for fixed (or slightly variable) energy cyclotrons accelerating a few different ions with use of trim coils to shape the magnetic fields. However, in order for a cyclotron to widely vary its projectiles and their energies, subdivisions in the main superconducting coil are commonly used to enhance control of the magnetic field shape, reducing the power needed for room temperature trim coils. The coils could be multiply divided in principle, but their field forms tend to become redundant. One split with two controllable currents is a natural choice in terms of cost, and provides adequate variation of field forms with coil excitations. The split location is then the parameter which needs to be optimized. In this study, three locations were investigated: one third from the top or the bottom, and at the middle of the coil. Figure 2.1 shows the field forms from each coil when a current density of 13000 amp/cm^2 is used. These are calculated by a program which integrates the Biot-Savart formula for each turn assuming median plane symmetry. The lower the split location is, the steeper the field slope is at the edge of the pole. The location of the split is basically determined according to the uses intended for the particular magnet. The coils of K500, K1200, for instance, have bottom and top splits, respectively. The AGOR cyclotron magnet on the other hand has the split

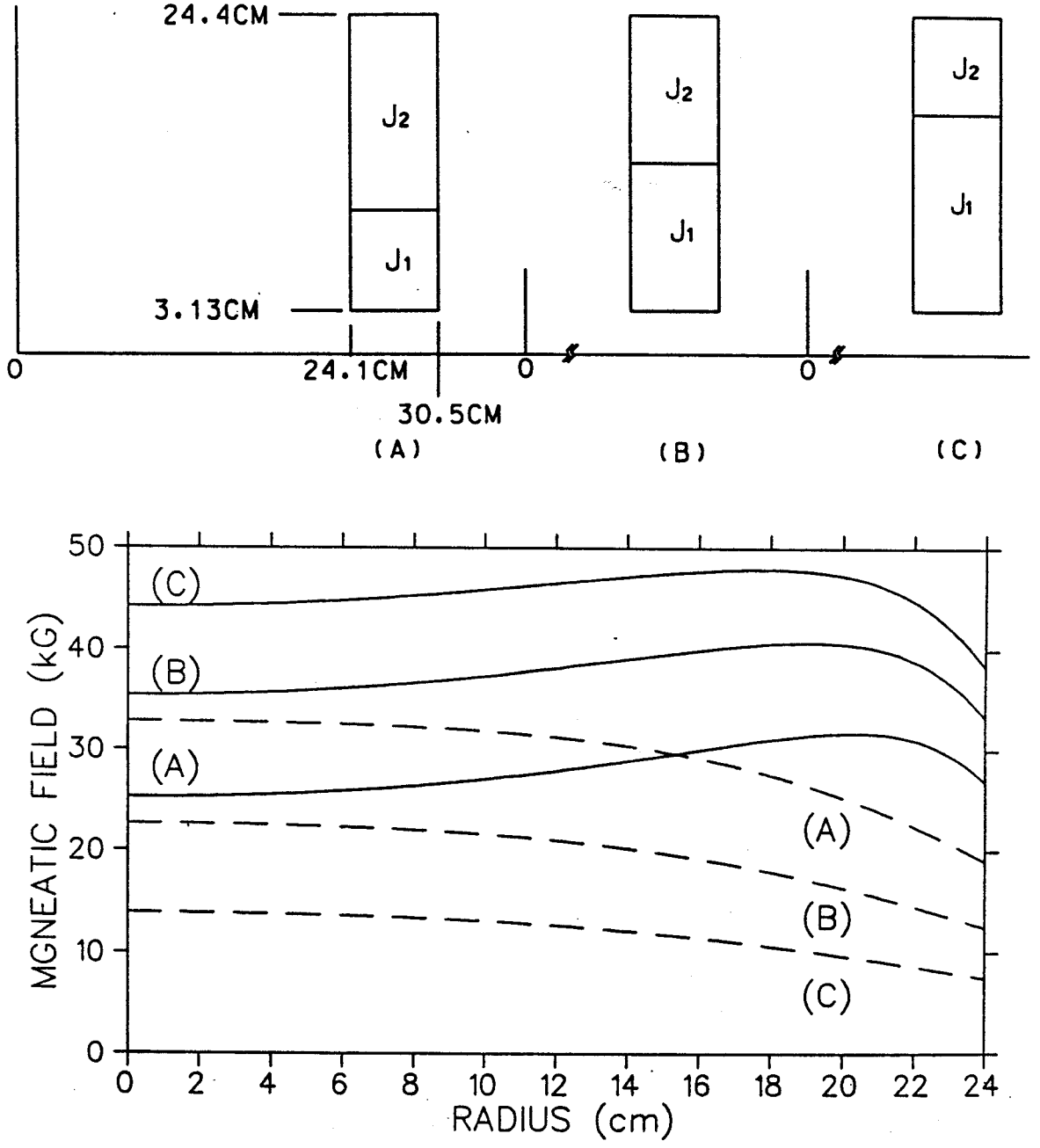

Figure 2.1: A quarter of coil cross-sections and magnetic field forms are shown for three different splits in the coils (median plane symmetry is assumed). A current density of 13,000 (amp/cm^2) is used. The solid lines are the field forms of the inner coil (J_1), and the dashed lines are those of the outer coil (J_2). The split in the 8 T coil is (c).

coils separated further to accelerate protons as well as heavy ions [Com88]. For the 8 T magnet, we chose the top split since calculations indicate that the magnetic fields fit better to the radially flat profiles at low excitations with the top split.

The capability of field shaping could be enhanced by using a reverse current in one of the two coils. The K1200 magnet, for instance, uses reverse current in the outer small coils when light ions are accelerated. The field form by this reverse current is helpful in generating isochronous fields for light ions, which can be inferred from Figure 2.1. This scheme, however, was not accepted for the 8 T magnet because of the desire to keep the coil design simple. In order to realize the reverse current scheme, there needs to be a complex mechanical support structure to clamp the outer coils against electromagnetic forces which are directed away from the median plane.

Since we have taken into consideration the eventual conversion of the 8 T magnet into a cyclotron, the magnet has the characteristics of an isochronous cyclotron in its magnetic field calculations; the pole tips have separate sectors. This is simulated by a stacking factor of 0.5 on the pole tips using the program POISSON [Men87], which means that the sector structure occupies 50% of the total volume. (The program POISSON solves electrostatic or magnetostatic problems in a 2-d Cartesian or 3-d cylindrical geometry by 'successive point over-relaxation method'.) The magnetic fields are fitted to flat profiles for three different excitations, and displayed in Figure 2.2. The pole tip is contoured in the valley region as in other superconducting cyclotrons to shape the fields. Even with a two coil system, it is difficult to make the magnetic field fit the flat profile in a broad field range with a single pole tip configuration. Trim coils usually employed for minute adjustments of field shapes are not considered because of the complexity of the system; sets of pole tips will be used instead to trim the profiles of the specific fields covering the range of 2-8 tesla.

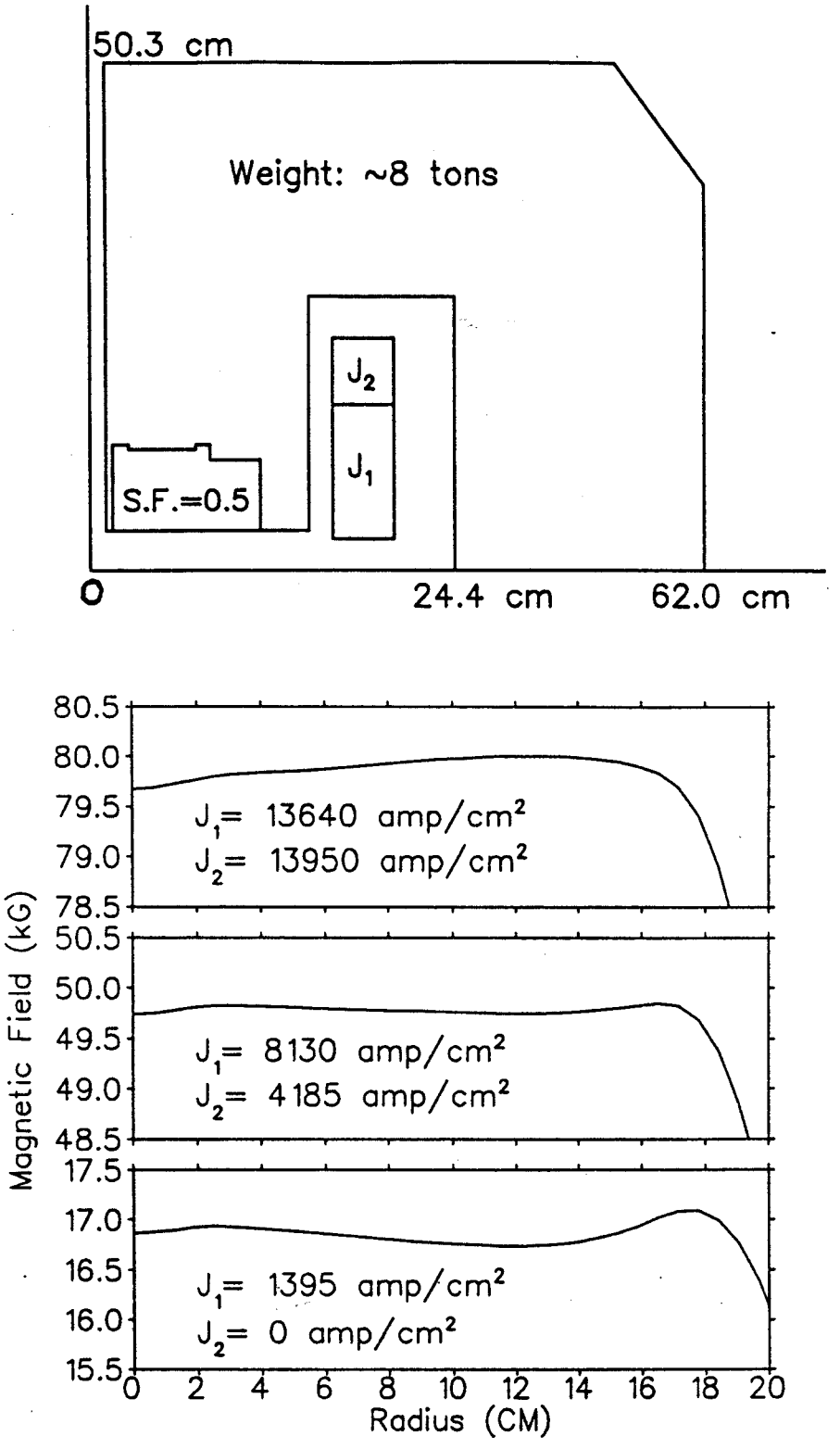

Figure 2.2: The magnetic fields are profiled to have a flat radial dependence covering the required range of 2-8 tesla. The flat profiles radially are chosen for ion source emittance experiments. The pole tips are contoured in the valley region as in other isochronous cyclotrons.

C 'Tightly banded coils' vs 'Free coils'

The most probable quench origin of superconducting solenoid coils is in the innermost layer where magnetic fields and stresses are maximum. If the coil is left on the winding form, a large shear stress occurs at the innermost layer due to the counter-force of friction on the coil form versus the axial magnetic force. The shear stress on that layer is then a likely cause of quenches (shear stresses in the coil originate from field variations, $\partial B_r/\partial r$ and $\partial B_z/\partial z$).

Besides the shear stress, differential thermal contractions produce tensile stress on the interfaces of different materials. When the coils cool down to 4 K, the estimated tensile stress on the Formvar insulator amounts to 4000 psi. This thermal stress in combination with the shear stress generates stress concentration sites on the interfaces, which could be potential quench origins.

Two different coil winding methods were considered in order to minimize stress problems in the coil. They are: the 'free coil' method, and the 'tightly banded coil' method. The difference between these two types depends on whether the innermost layer is free from the winding form or tightly clamped to the winding form by winding and banding preloads. (The free coils are also often banded; however, the innermost layer is clear from the bobbin.)

Tightly banded coils have some advantages over free coils, and are widely used. One main advantage is that the coil construction is much easier because the coil does not have to be removed from the winding form. In these coils, however, the shear stress can easily exceed the shear strength of the epoxy bonds in the potted coils. Cracks and de-bonds of epoxy joints induced by large shear stress can cause magnet quenches at lower than design current, which can result in severe coil training.

In addition, frictional coil motions on the bobbin can easily cause repetitive

quenches in tightly banded coils; the axial magnetic force compresses the coil, and frictional motion occurs at the interface between the coil and bobbin, with the inverse motion occurring when the coil de-excites. Two different approaches have been used to circumvent this problem. The first is to satisfy the equation below so that the frictional force prevents any axial coil motion on the interface.

$$\mu F_r > F_a, \tag{2.1}$$

where μ is the frictional constant, F_r is the residual radial force on the coil/bobbin interface, and F_a is the axial magnetic force in the coil at the highest excitation. However, this approach has difficulties at very high fields in that the preloads required to produce a sufficiently large F_r can be excessive. For instance, over 15,000 psi of winding preloads and 30,000 psi of banding (2.54 cm thick aluminum) preloads on a 1.3 cm thick stainless steel bobbin are needed to meet this condition for the 8 T magnet. These high pretensions are not easy to apply in the actual winding, and also they are limited by the yield strengths of each material.

A partial free coil method uses lower preloads, but ones which are high enough to always keep the residual radial stress on the boundary compressive [Ant89]. In this approach, the innermost layer will slide on the bobbin, and a smooth slip plane is necessary to avoid sudden motions which can generate more heat than can be diffused away. This approach may not work as expected, because it is difficult to ensure smooth sliding. For the 8 T magnet, a design based on this method has a winding tension of 10,000 psi on a 1.3 cm thick stainless steel bobbin, and a banding tension of 25,000 psi by aluminum wire with an overall thickness of 2.54 cm. Stress distributions with these preloads were calculated with a finite element analysis program developed in this lab [Dek], and are shown in Fig.2.3. The calculated shear stresses are larger than the shear strength of the epoxy or the Formvar insulator bonds. However, these stresses are overestimated in the calculation due to the constrained boundary

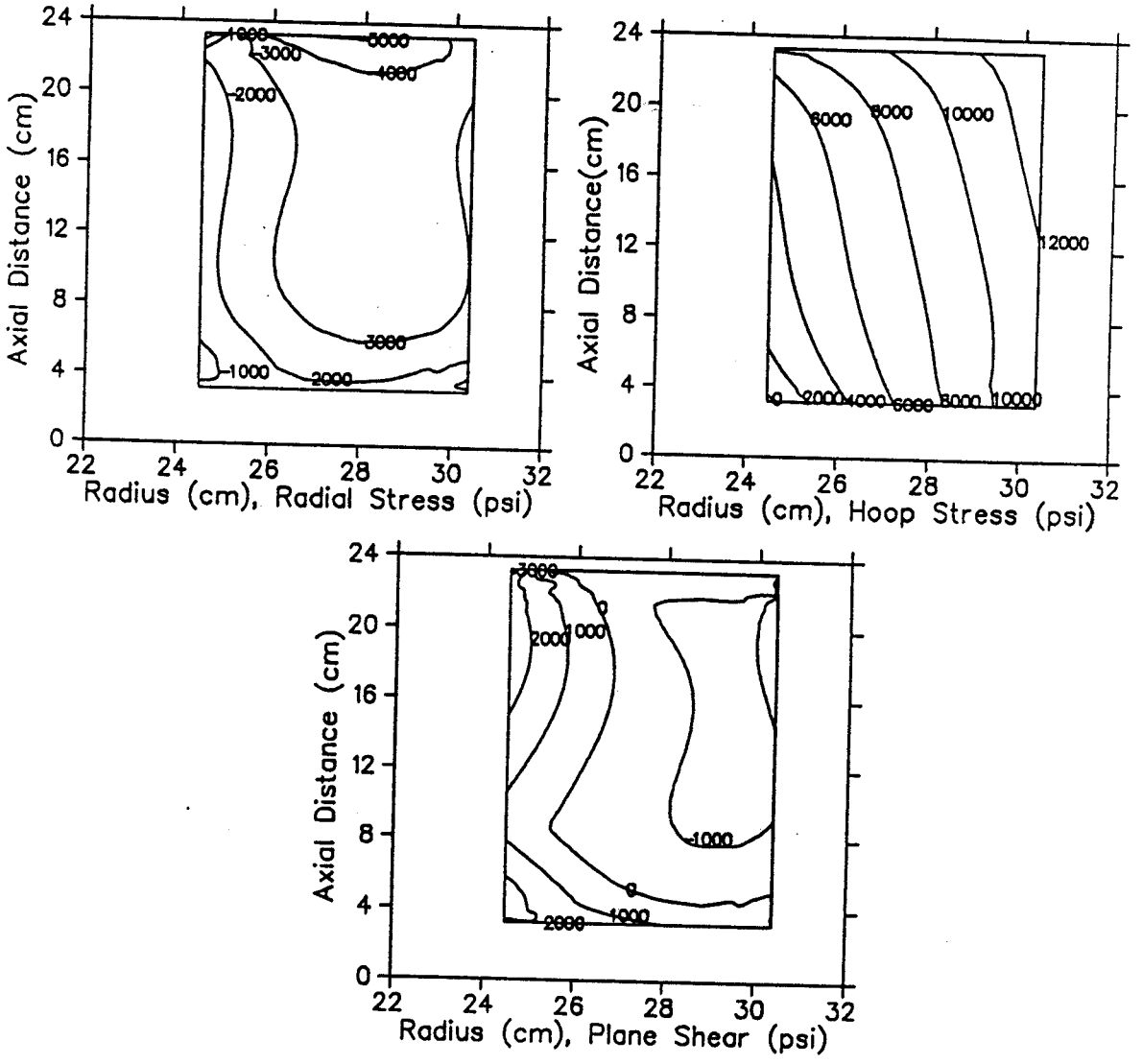

Figure 2.3: Two dimensional stress distributions are calculated by the finite element program for a tightly banded coil. The winding tension applied on the wire is 10,000 psi with a stainless steel bobbin of 1.3 cm thick, and the banding preload is 25,000 psi by aluminum wires with a total thickness of 2.54 cm. The sign convension is that tensile stresses are positive, and compressive stresses negative.

these stresses are overestimated in the calculation due to the constrained boundary condition at the interface (slip motions are not allowed on the boundary; the program at present is not able to handle the boundary condition realistically). The radial and hoop stress distributions are similar to those calculated by STANSOL [Joh76] in regions away from the boundary. (The program STANSOL computes forces in an infinitely long azimuthally symmetric, cylindrical structure in which the radial dependence of the magnetic field is inserted numerically using data from the z slice of the real coil at which the field is the highest.)

Free coils are basically accomplished by removing the contact of the innermost layer with the bobbin. There are two different methods to fulfill this idea; 1) the coil is wound like the tightly banded coil, but with lower pretensions so that the coil lifts off the bobbin at low excitation to become a free coil at high excitation, or 2) the coil is wound on the winding form, and then the form is removed after completing the winding. The shear stress and frictional motions due to contact with the bobbin are then eliminated; the coil deforms freely, and finds its natural shape. There are however other constraints to coil deformation, such as the banding and the median plane support. The banding constrains mostly outer layers of the coil where magnetic fields are low so that some frictional motions can be tolerable. The median plane support usually has smooth slip surfaces to reduce the frictional heat.

For a free coil which has the same dimensions as the 8 T coil with a winding preload of 5000 psi, and a banding preload of 10,000 psi by aluminum wires with a total thickness of 2.54 cm, shear stress was calculated assuming that the coil is bonded (i.e. no sliding) to a solid stainless steel midplane structure (a usual boundary condition in the finite element program); results are shown in Figure 2.4. The maximum plane shear stress of 4000 psi at the inner corner is unsafe compared to the shear strength of the epoxy bond so that the bond may break, generating heat to initiate a quench

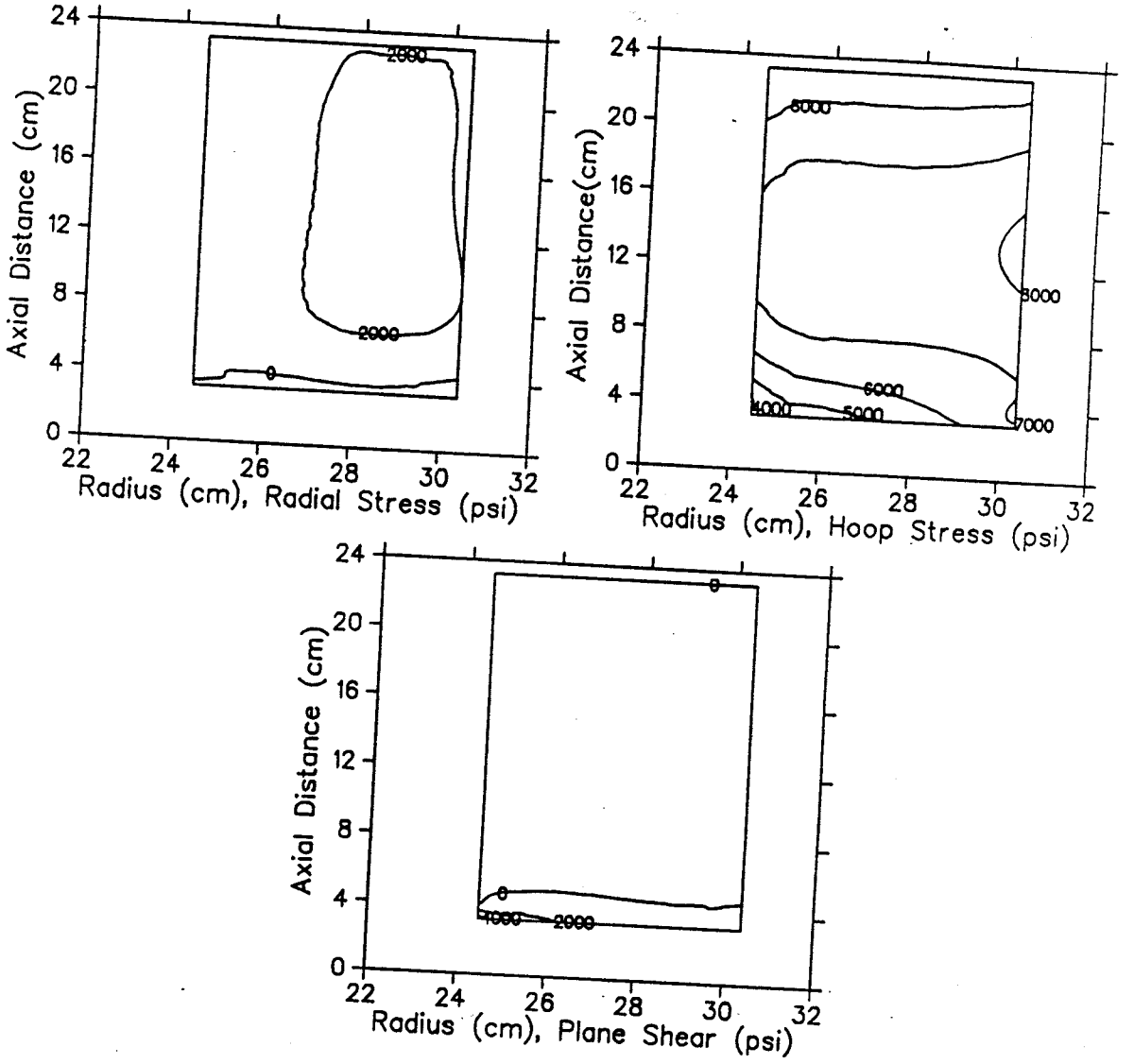

Figure 2.4: The stress distributions in a free coil at 8 tesla excitation calculated by the finite element program. The coil is assumed to be bonded to the solid stainless steel midplane structure. The winding preload is 5000 psi, and the banding preload is 10,000 psi by aluminium wires with a total thickness of 2.54 cm.

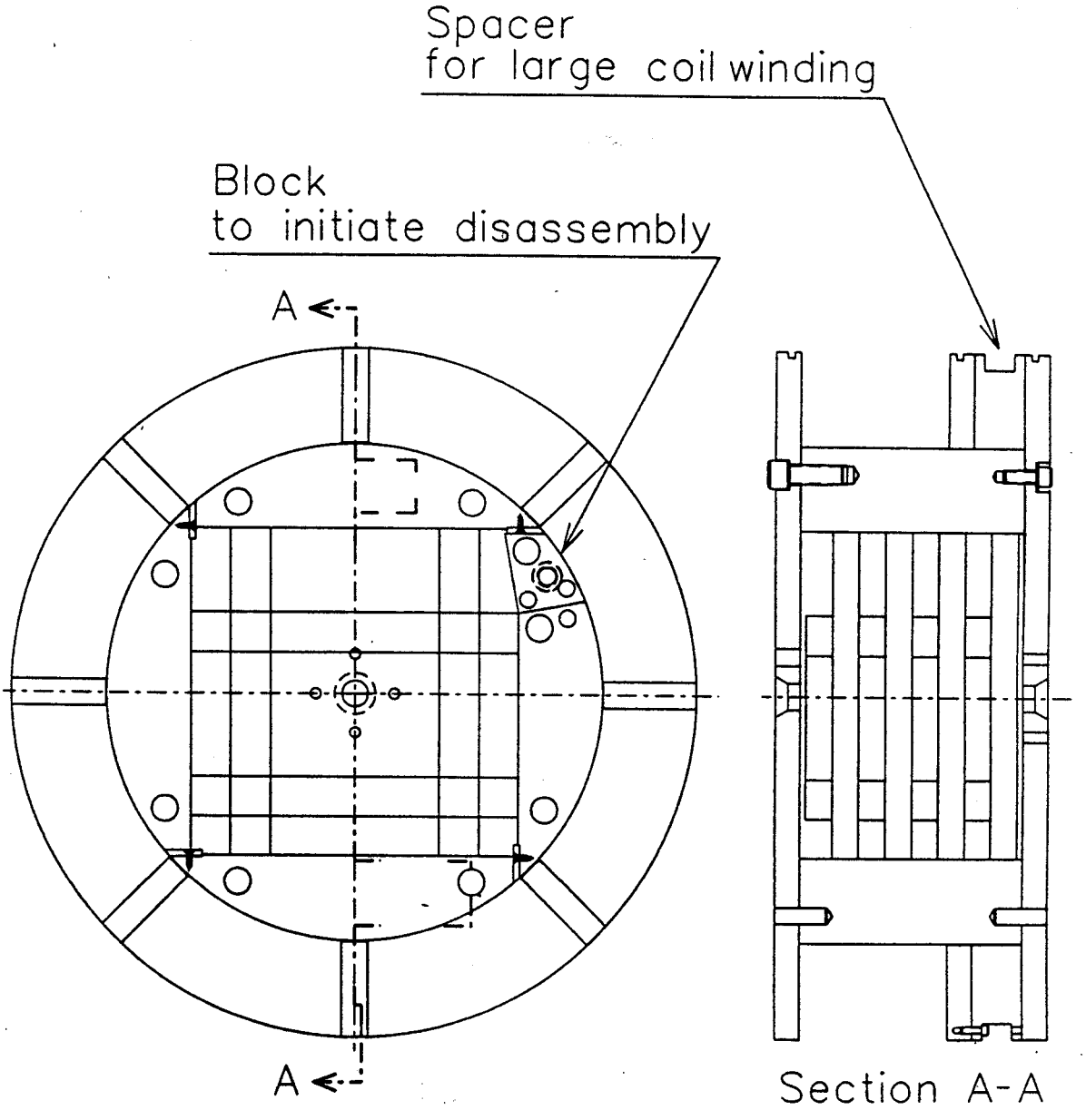

Figure 2.5: A removable winding form used for the 8 tesla coil construction to ensure removal of the coils from the bore tube.

motions at the coil/midplane interface but strong in the axial direction to support the coil to coil force was then conceived, (and was the structure actually used for the 8 T magnet as described in section 2.II.D).

After reviewing the difficulties of tightly banded coils in avoiding the shear stress and frictional motions, the free coil approach was chosen for the 8 T magnet. A removable winding form shown in Figure 2.5 was employed since this method ensures that the coil is completely free from the bore tube.

D Stress estimates for the 8 T coil

The total forces on each coil are calculated by the FORCE subroutine in the POISSON code group which integrates the Maxwell stress tensor [Jac75] around the boundary of the specified region. Calculated forces at the maximum design currents (I= 400 A for both coils) are shown in Figure 2.6. The average axial stress is 3000 psi on the median plane support, and 3600 psi on the plane between small and large coils.

By using a free coil instead of a tightly banded coil, shear stress on the innermost layer is avoided. However, the stress estimation becomes more complicated because the program has to simulate the process of the winding form removal. Some preloads are partially relaxed by this process since the zero radial stress boundary shifts from the inner surface of the winding form to the innermost layer of the coil. To estimate the stresses on the free coils, the program STANSOL is primarily used. (Since the highest hoop stress is the major concern, a z dependent stress analysis capable of calculating the axial and shear stresses was omitted.) The procedure to calculate the stress distributions in the coil including the effect of the winding form removal is as follows:

1) Compute the stress distributions with the winding form included when the winding

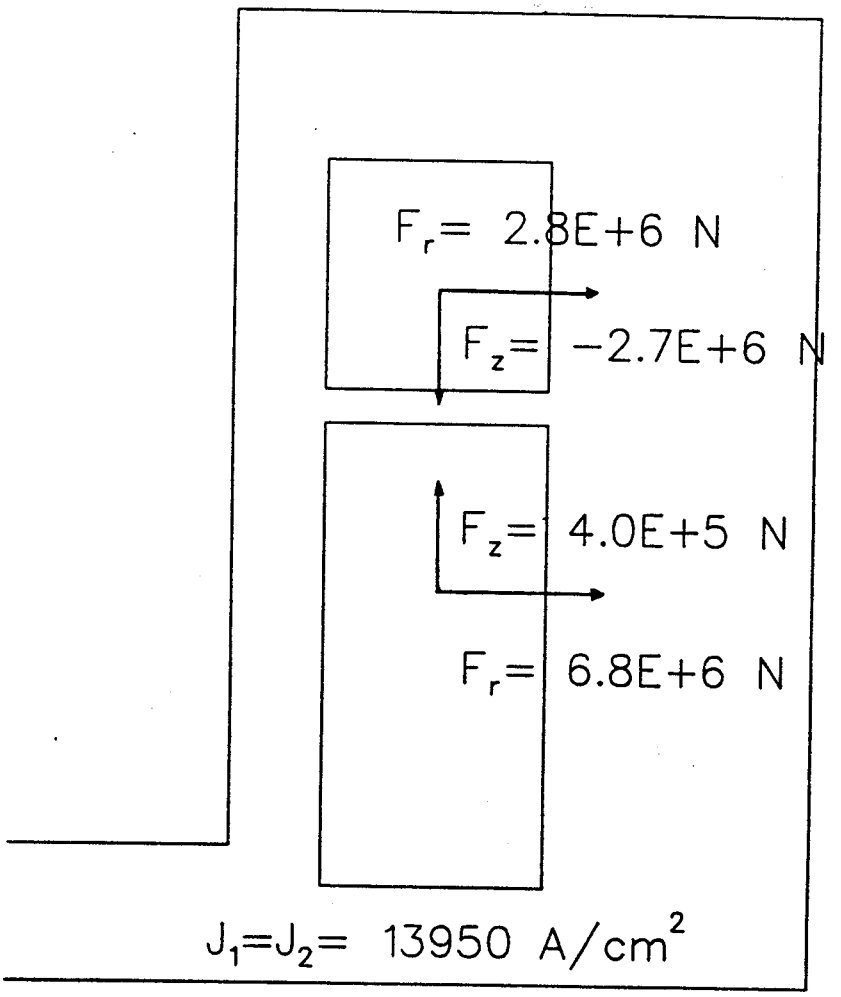

Figure 2.6: Total axial and radial forces on the inner and outer coils are calculated with the program POISSON at 8 tesla excitation with I=400 A. The axial stress on the midplane is 3000 psi.

and banding preloads are considered, and obtain the pressure exerted by the winding form on the innermost layer of the coil.

2) Modify the stress distributions to account for the radial force which is removed by removing the winding form. This can be simulated in STANSOL by computing the incremental effect of an inward radial pressure applied at the interface between coil and winding form with magnitude set to give zero net radial stress at this interface.

3) Subtract the stress distributions of 2) from 1), to obtain the stress distribution in the 'free coil', but before the coil cools down to 4 K.

4) Calculate the thermal and magnetic stresses

5) Add 3) and 4) to obtain the final stress distributions at 8 tesla.

Resulting stress distributions at each step are depicted in Figure 2.7. The maximum hoop stress in the conductor is near 16,000 psi, which is a comfortable value.

E Relaxation of preloads

In the actual coil, some relaxation of the preloads on the winding and banding was implied by measurements of the coil diameter before and after curing the epoxy. A change of 0.18 mm in the outside diameter of the banding was measured, and it was quite uniform for all four coils, regardless of location. Both a simple calculation and STANSOL indicated that the reduced diameter of the banding corresponded to release of the entire banding preload.

The simple estimate of the preload loss was made using a standard formula [Coo85] for the case of an infinite, homogeneous, linearly elastic cylinder; in this circumstance the hoop stress is

$$\sigma_\theta = \frac{Y}{1-\nu^2}\left(\frac{u}{r} + \nu\frac{du}{dr}\right), \tag{2.2}$$

where ν is Poisson's ratio, u is the displacement, and Y is Young's modulus. Since the banding is relatively thin and homogeneous, its radial displacement is approximately

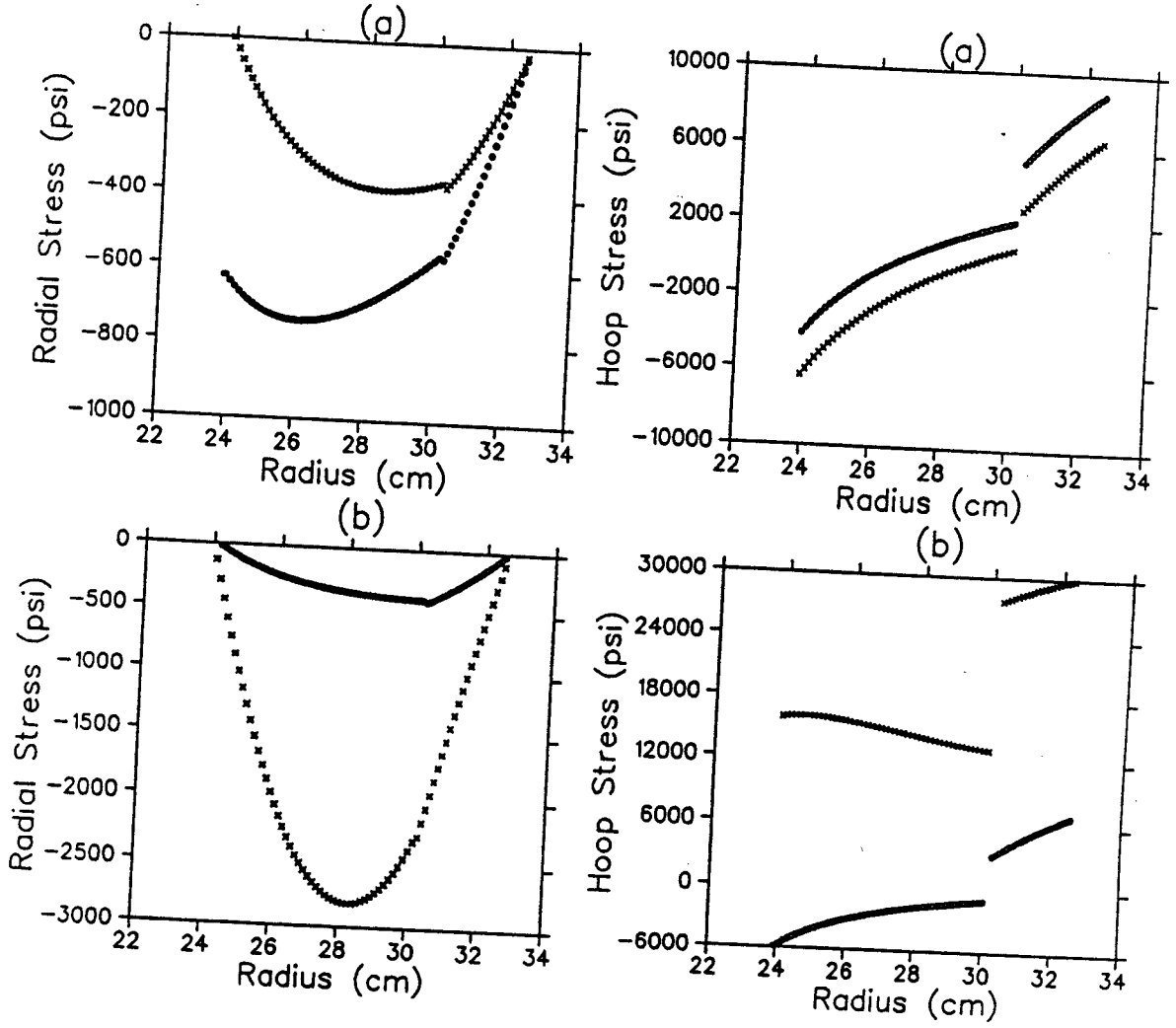

Figure 2.7: After the coils are wound and banded on the winding form, the stress distributions are depicted in (a) by circle. At this point, the interface between the coil and winding form at the radius of about 24 cm, is under compression by 620 psi. This stress is reset to the no winding form condition by applying an inward radial pressure of 620 psi at 24 cm, and then the distributions are as shown in (a) by cross. The stress distributions after cool down (circle) and full excitation (cross) are displayed in (b).

independent of radius so that the second term in parenthesis vanishes. With r=32.8 cm and u=0.09 mm, σ_θ is about 8300 psi; this figure corresponds closely to loss of the entire pretension on the banding.

Some of the winding preload in the coil, especially of the outer layers probably also relaxed in the curing cycle. However, this does not greatly affect the maximum hoop stress in the coil which occurs at the innermost layer. The maximum hoop stress without the banding preload reaches 20,000 psi vs 16,000 psi with the design preload.

In principle, if the hoop stress on the conductor is higher than the yield strength of the copper matrix (~15,000 psi), the copper may deform plastically while the filaments remain elastic because of their higher yield strength, which would mean that the filament would carry nearly all of the additional applied stress. The difficulty in accurately clarifying the situation is that the superconductors are twisted, giving an admixture of the characteristics of a spring rather than pure solid wires. As a result, the effective characteristic of stress versus strain is difficult to describe. (To avoid this poorly defined region, the stress level is normally kept below the yield strength of the matrix material.) Monolithic conductors like the one used for 8 T coils with low Cu to Sc ratio may be more tolerable to the high stress than the cable type conductor or a conductor with a large amount of stabilizer, since the superconductor (NbTi) itself can sustain much higher stresses without degrading the critical current [Ree83]. (The successful operation of the coil at fields in excess of design values as described in a later section implies a sharing of stress between NbTi and Cu in a way which leaves the critical current essentially at the level indicated by the manufacturer's tests.)

F Selection of banding material

To reduce the circumferential (hoop) stress on the conductor, induced by the strong radial magnetic force, circular superconducting coils are often 'banded' with highly

pre-tensioned wires. Two alternative banding materials are widely used 1) stainless steel to use its large elastic modulus, and 2) aluminum to utilize its high thermal shrinkage. Material properties of aluminum and stainless steel relative to those of the coil (which is dominantly copper) are: Young's modulus: $Y_{stainless\ steel} \simeq 30$ Mpsi, $Y_{aluminum} \simeq 11$ Mpsi, $Y_{copper} \simeq 16$ Mpsi, where 1 Mpsi= 6.9 GPa and 1 MPa= 145 psi ; $(L_{293}\text{-}L_4)/L_{293}$ (%): 0.306 for 304 stainless steel, 0.415 for aluminum, and 0.324 for copper [Bub].

The stainless steel banding suppresses the coil displacement by the magnetic force more effectively than aluminum due to the higher modulus, thus reducing the coil stress. This advantage of stainless steel is weakened by its smaller thermal shrinkage than copper so that a portion of any preload is relieved when the coil cools down to 4 K. Whether the stainless steel or aluminum banding is used for the 8 T magnet with the same preload and overall thickness, the maximum hoop stress on conductor is similar; 16,000 psi, 17,000 psi with the stainless steel and aluminum banding, respectively at 8 tesla. In the 8 T magnet, 'clam shells' of solid stainless steel (see section 2.II.D) surround the banding to support the coil from the outer surface, and for these, stainless steel banding may be advantageous because of matching in the thermal shrinkage at 4 K, and also because of ease in welding. The rectangular stainless steel wire was therefore chosen for the 8 T coil banding, whereas both large cyclotrons in this lab (K1200, K500) employ rectangular aluminum wires for banding. (Advantage in weight of aluminum banding could be an important factor for some applications.)

G Test of stainless steel cable as a banding material

Rectangular solid wires are usually chosen for the banding because they make the winding orderly. Stainless steel cable (largely used for aircraft) was also considered

Table 2.3: Transverse Young's modulus of the coil wound with aircraft cable as a function of the applied loads.

Load applied	Incremental Stress	Incremental Strain	Young's modulus(Y_b)
3060 Kg	630 psi	0.002	0.31 Mpsi
5080 Kg	680 psi	0.002	0.34 Mpsi
8640 Kg	680 psi	0.002	0.34 Mpsi
11,380 Kg	650 psi	0.002	0.32 Mpsi

and tested, since a commercial company (Cryomagnetics Inc.) was using it for their high field magnets. The elastic modulus of the cable itself was measured first. Because of the structural stretch, the effective modulus was small at the beginning of loading ($\simeq$ 10 Mpsi). As the cable was stretched out, the modulus reached 18 Mpsi.

A small test cylinder was wound with this cable to develop an orderly-layered winding technique and to measure the actual elastic modulus of multiple layers of such cable. The same tensioning equipment later employed for the 8 T coil winding was used to wind the coil on an aluminum form. After the winding was completed, the coil package was dipped into liquid nitrogen to shrink the aluminum form away for removal.

The elastic modulus of the coil was measured with the help of the MSU Dept. of Forestry. Only the axial modulus was measured since the measurement of the radial modulus requires a complicated loading system inside the coil. Table 2.3 shows the differential elastic modulus for the applied loads. The axial stiffness is similar to that of hard wood and smaller by two orders of magnitude than the modulus of the parent material.

If the radial stiffness of the banding can be kept the same as that of the solid stainless steel banding, an axially soft banding would be beneficial for the superconducting coil since the shear stress due to the banding can be reduced. When the

SC-coils are energized, the axially soft banding would compress or expand together with the coil, rather than risking the SC-coils sliding on the interface and generating heat. In practice, the outer layer of the SC-coil contacting the banding is not likely to be the quench origin because of lower magnetic fields than in the inner layer. The axial softness advantage, therefore, was not considered as a dominant factor in selecting banding material, and rectangular 304 stainless steel wire was chosen.

H Effect of transverse Young's modulus of banding on frictional coil motion

Although the shear stress due to banding may not cause coil performance degradation because of lower magnetic fields than in the inner layer, it would be a good feature to reduce overall shear stress in the coil by employing an axially soft banding. The larger transverse Young's modulus of banding (Y_b) is, the higher shear stress is generated if the banding is perfectly bonded to the coil. In reality, however, coil sliding occurs when the banding is not soft enough to follow the axial coil displacement, reducing the residual shear stress. Based on a simple model, Y_b is quantitatively related to the coil sliding motion against the banding for the 8 T coil case.

It is assumed that both the coil and banding are bonded on the z=0 plane, and that the radial magnetic pressure (P_r) from the coil uniformly pushes the banding; i.e. P_r is a constant (see the illustration below). The static frictional pressure is then μP_r, and the resulting axial frictional force on dz in the banding is $\mu P_r 2\pi r dz$, where μ is a frictional coefficient, and r is the radius at the interface. Another assumption is that this axial frictional force acts as a body force, which could be justified by a thin banding. The axial stress in the banding (σ_z) with a cross-sectional area of $2\pi(r+t/2)t$, is then given as a linear function of z, where t is the banding thickness

(r≫t);

$$d\sigma_z = \frac{\mu P_r 2\pi r}{2\pi(r+t/2)t}dz \simeq \frac{\mu P_r}{t}dz, \qquad \sigma_z = \frac{\mu P_r}{t}(l-z), \tag{2.3}$$

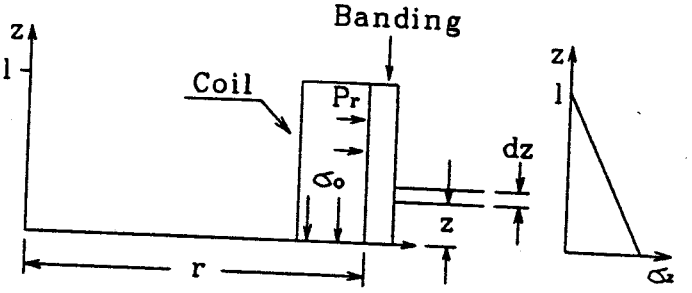

The axial banding displacement (u) is obtained from the relationship of stress and strain, $\sigma_z = Y_b du/dz$, and from Eq.2.3;

$$u(z)_{band} = A(lz - \frac{z^2}{2}), \quad where \quad A = \frac{\mu P_r}{t}\frac{1}{Y_b}, \tag{2.4}$$

By the similar procedure, the axial coil displacement is related to the axial magnetic force as written below;

$$u(z)_{coil} = \frac{1}{Y_{coil}}\frac{1}{l}\sigma_0(l - \frac{z^2}{2}) = B(lz - \frac{z^2}{2}), \quad where \quad B = \frac{\sigma_0}{lY_{coil}}, \tag{2.5}$$

where σ_0 is the axial stress on the median plane (~3000 psi at 8 tesla), l is the coil height, and Y_{coil} is the transverse Young's modulus of the coil. In deriving Eq.2.5, a uniform axial body force in the coil is assumed. As a result, the axial coil displacement is underestimated since the axial magnetic force is generally larger for larger z rather than a constant in a split solenoid.

Eq.2.4, 2.5 are applied to the large coil of the 8 T magnet at 8 tesla, which has a 2.54 cm thick banding. When the transverse Y_b is 0.3 Mpsi, A is about $7\times10^{-4}cm^{-1}$ (t=2.54 cm, l= 14 cm, P_r= 2000 psi, and μ=0.3, where a universal μ value is used since the frictional coefficient usually depends on many uncontrollable variations such as surface conditions, see reference [Ken80]), and B is $2\times10^{-5}cm^{-1}$, which means that the banding displacements by the frictional force would match with the coil displacements by the axial magnetic force. The cable banding described in the previous section which has Y_b= 0.3 Mpsi would therefore move together with the coil, and solid stainless steel banding which has Y_b= 30 Mpsi would not. When the transverse Young's modulus is between 0.3 and 30 Mpsi so that A is close to B, it would be difficult to predict the coil/banding behavior because of uncertainties in μ and in the model.

I Magnet quench simulations

Quench phenomena have been extensively studied by many researchers [Dre82] [Kad85] [Kur88]. Using these techniques, the design parameters of the 8 T coil and conductor were evaluated in the circumstance of coil quenching. Quench scenarios were simulated using the program QUENCH [Wil68] to evaluate the coil behavior. (QUENCH solves the heat diffusion and the coupled circuit equations to obtain physical parameters as a function of time.)

Quenches in superconducting coils can be subdivided into two classifications: 1) short sample limited, and 2) energy deposited. A 'short sample limited' quench occurs when the coil current reaches the critical current of the conductor whereas an 'energy deposited' quench occurs when a mechanical disturbance in the coil generates heat larger than the critical energy.

The maximum operating current of the coil is determined relative to the short sample critical current, and defined as the current margin, m_i in Eq.2.6, which comes

Table 2.4: Critical current data of the 8 T conductor from Supercon Inc. for T= 4.22 K. The measurement was made on a strand used for the small coil.

B (Tesla)	I_c (A)
5.0	1500
6.0	1219
7.0	939

from reference [Dev90].

$$m_i = \frac{I_c(T_0) - I_{op}}{I_c(T_0)}, \tag{2.6}$$

where I_c is the critical current, and I_{op} is the operating current. Since $I_c(4.4K)$ of the 8 T magnet conductor is 580 A and $I_{op}(4.4K)$ is about 400 A at 8 tesla, m_i is 31%. (In this estimation, the critical current at 8 tesla is obtained by linear extrapolation since the measured data provided by Supercon Inc. ends at 7.0 tesla as shown in Table 2.4.) For comparison this margin is considerably higher than the 10% of the SSC dipole's m_i and somewhat above the 25% of the HERA dipole's m_i [Dev90]. Current margin is, of course, an expensive parameter when many magnets have to be built because of the higher cost of the conductor and the larger magnet size. In both the SSC and HERA magnets, the winding technique was carefully perfected in many prototypes so that the smaller margin could be used without jeopardizing the overall design safety factor. (The design m_i of the 8 T magnet reaches 0% at a main field of 8.7 tesla at 4.4 K, where I= 450 A, and the maximum magnetic field in the coil is 8.5 tesla.)

The second type of quench, due to energy-deposit, is initiated by disturbances such as wire motion or epoxy cracks, which cause the temperature at the quench origin to increase, resulting in reduced critical current, resistive dissipation, and consequent

thermal runaway. An important question is the amount of energy needed to initiate a quench. The analyses below of the critical energy and critical normal volume closely follow the method described in reference [Dev90]; underlying concepts are detailed in chapter 5 of M. Wilson's book [Wil83].

A minimum energy deposit can be obtained from the critical energy density and minimal normal volume at the operating current and temperature. The critical energy density is an integral of the specific heat between operating and critical temperature as defined in (2.7).

$$E_c = \int_{T_o}^{T_c} dTC(T), \tag{2.7}$$

where C(T) is the volumetric specific heat. A minimal normal volume (V_{min}) is needed to continue to propagate the normal region [Wil83]. If the normal region is smaller than V_{min}, it diffuses away, and a superconducting state is restored. The minimum energy deposit can be then defined as below from reference [Dev90]);

$$W_c = E_c V_{min} = \sqrt{\frac{2D_{th}}{\rho}} \frac{E_c^{3/2} A^2}{I}, \tag{2.8}$$

where the D_{th}=k/C is thermal diffusivity of conductor, k is thermal conductivity, ρ is resistivity, A is cross section area of conductor, and I is the current at quench. At 8 tesla and 400 amps, T_c is approximately 4.9 K, and using the specific heat data from reference [Wil83], E_c = 1200 J/m^3, and W_c= 14μJ; i.e. a tiny fraction of the total magnetic field energy density of 70 MJ/m^3 at 8 tesla (E_c = 477 J/m^3, and W_c= 2.5μJ for the SSC prototype dipole [Dev90]).

Some electromagnetic energy of the coil is stored as strain energy (although most of the energy is in the magnetic field). If the epoxy (or insulator) cracks, this stored strain energy is released as heat. The elastic energy stored in volume V under stress of σ is

$$U = \frac{1}{2} \frac{\sigma^2}{Y} V \tag{2.9}$$

When the elastic energy release equals the minimum energy deposit, the coil quenches. Then, V_{min} to propagate the normal region is

$$V_{min} = 2\frac{YW_c}{\sigma^2} \tag{2.10}$$

Assuming that the insulation on the wide face of the conductor cracks, the minimum crack length in order to initiate a coil quench can be written as follows;

$$l_{min} = \frac{V_{min}}{wt}, \tag{2.11}$$

where t is the thickness of the Formvar insulator ($\simeq$ 0.05 mm for the 8 T magnet conductor), and w is the conductor width ($\simeq$ 2.0 mm). With σ= 4000 psi and Y= 300,000 psi for Formvar insulator, it is calculated that V_{min}= 0.07 mm^3, l_{min}= 0.7 mm. These small values imply that tiny cracks can easily trigger a quench.

Once a quench has started, the QUENCH program calculates the ensuing spread of the quench region. Two different cases may be assumed: 1) both large and small coil pairs quench at the same time, 2) one coil quenches first, followed by the other coils. The second case is more frequent, and worse than the first because the current transfer from the quenched coil pair to the other coil pair due to the inductive coupling at first increases the current in that coil above its normal value. It is, however, unlikely that only one coil will quench and the other will stay in a superconducting state for a long period of time, considering that the liquid helium would run out quickly. The delay time was difficult to estimate without experimental information. The QUENCH results presented in Figure 2.8 assume, for example, a 2 second delay between the large coil and the small coil quenches; either coil becomes fully normal in less than a second after the start of the quench (as shown in the normal volume verse time plot in Figure 2.8). The small coil energy dissipation of 0.3 MJ in a 2 second period is sufficient to increase the average small coil temperature to 60 K. The assumed 2

second delay thus should be certainly long enough to initiate the large coil quench by disturbing liquid helium, and if the actual delay is less, the current build up is reduced. (The hot spot temperature and IR drop increases for a longer delay, but not significantly: for instance, V_{max}= 4.7 kV, and T_{max}= 380 K with a 6 second delay.)

In these simulations, the quench is assumed to be initiated at the inner corner of the coil, and the transverse propagation velocity is assumed to be 5% of the longitudinal velocity (along the conductor), which is in the range of 0.1-10% usually used for potted coils. (The definition of the velocity ratio can be found in reference [Wil83].) Another assumption in the present calculation is that the stored energy is dissipated in only one of the serially connected image coils while the other coil remains in a superconducting state. In actual operation, the image coil may or may not quench before a significant amount of stored energy is dissipated in the quenched coil, which is difficult to predict. If the other coil quench follows immediately, the I^2R dissipation will be shared, leading to lower hot spot temperature as well as lower voltage to ground at the center tap – the single coil quench considered here is therefore a worst case situation.

The hot spot temperature of 350 K shown in Figure 2.8 would not be expected to degrade any coil material, but thermal differentials could conceivably cause damage such as cracks. Measurements of hot spot temperature for potted coils in other laboratories however indicate that these coils comfortably survive much higher temperatures [Dev89]; experiments at BNL for instance showed that the hot spot temperature of 800 K caused no damage [MeB].

The left center plot in Figure 2.8 shows that the maximum IR drop reaches 4.5 kV, and the consequent voltage drop between layers is about 100 V, which can be easily sustained due to the wire insulation and epoxy paper. If the quench is entirely in one coil of a pair as assumed, a real voltage to ground of one half of the IR drop

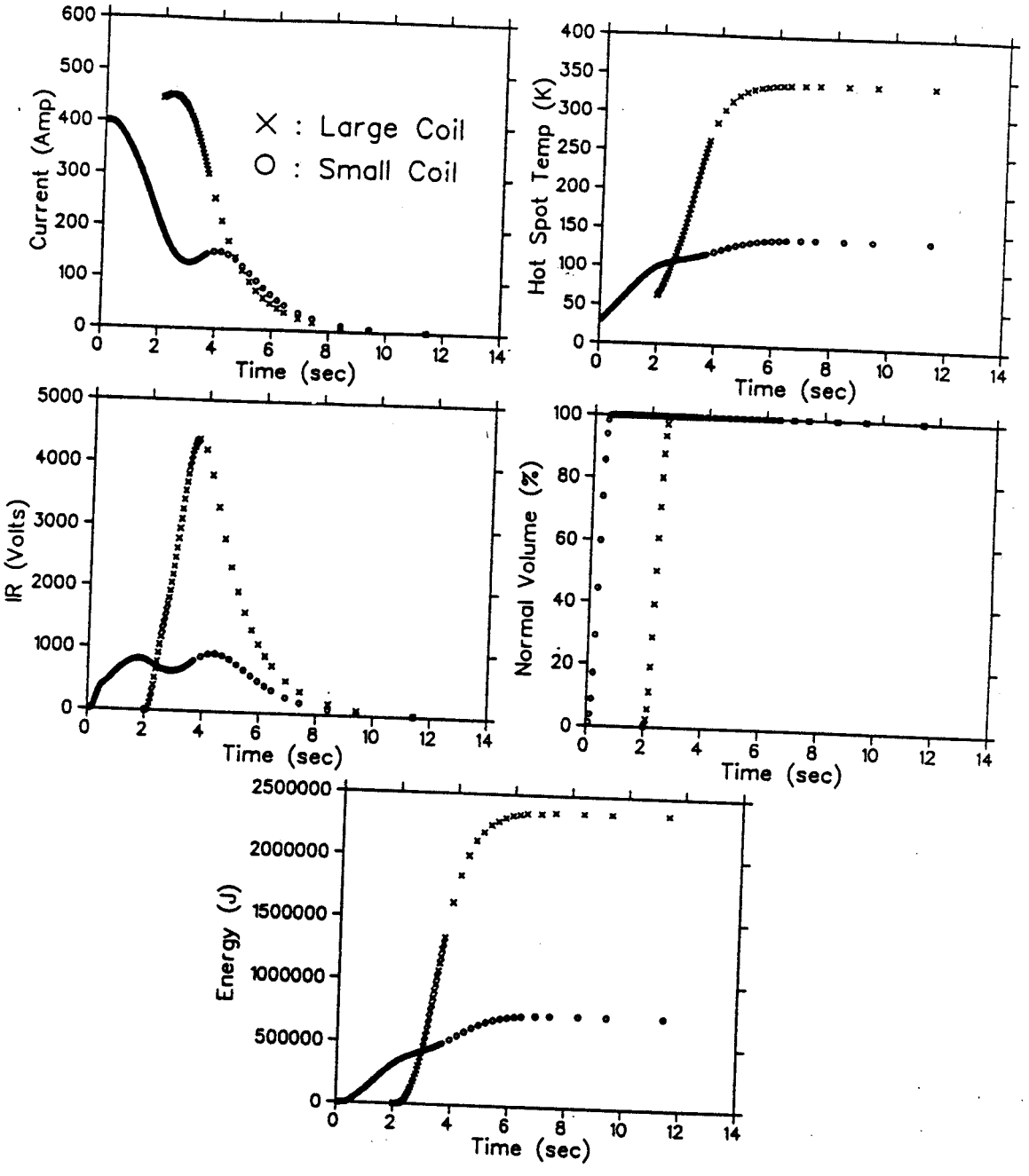

Figure 2.8: When the large coil is assumed to quench two seconds after the small coil, the physical parameters are calculated as a function of time by QUENCH. The hot spot temperature and IR drop across the coil seem to be in the acceptable range. The energy in the bottom graph is the I^2R dissipation.

(i.e. 2.3 kV) will appear at the median plane interconnection between the two coils, and the insulation on this interconnection was designed to handle this voltage.

J Effect of an aluminum bobbin in a quench

In high field solenoids for high energy physics experiments, high-conductivity aluminum is often used as the bobbin material in order to spread quench energy broadly through the coil [Gre84]. Another important attribute of aluminum comes from its higher thermal contraction relative to copper; an aluminum bobbin thus shrinks away from the coil when cooling down to 4 K, or the coil lifts off the bobbin at low excitations. (Instead of plain aluminum, a bimetal which has the aluminum side toward the coil, and the stainless steel side as part of the helium tank, was an option considered for the 8 T magnet since aluminum is rather difficult to weld as an ultravacuum tight structure.) A schematic view of a coil of this type and a circuit diagram are shown in the upper part of Figure 2.9. The two coils and the bobbin constitute three coupled circuits as shown at the upper right of Figure 2.9, and with this model the system was studied analytically. For these studies, inductances of the circuits were obtained from stored energies calculated by POISSON; results are given in Table 2.5.

The effect of the aluminum bobbin during a magnet quench as analyzed by the program QUENCH is shown in the lower part of Figure 2.9. The stored energy, unfortunately, shifts to the aluminum bobbin rather slowly because of the poor magnetic coupling between the bobbin and the coil. The bobbin temperature does not even reach 10 K before the normal zone has propagated through the coil (due to the large Δr of the 8 T coil compared to typical high energy solenoids). Even at this level, the bobbin heating may trigger a quench in the series connected median plane image coil of the quenched coil, but the triggering is not fast enough to greatly improve the quench behavior.

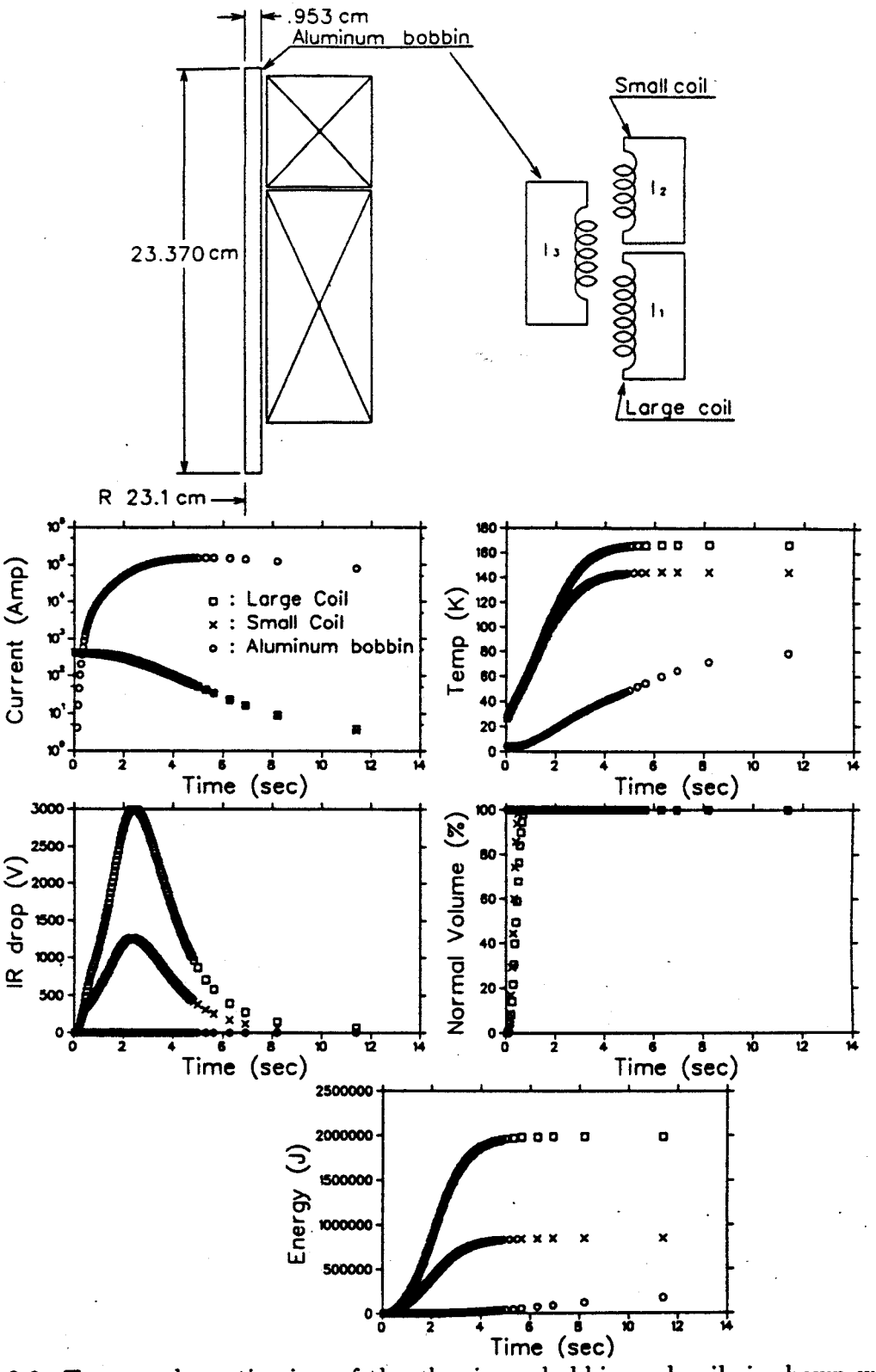

Figure 2.9: Top: a schematic view of the aluminum bobbin and coils is shown with a circuit diagram. Lower: QUENCH code results when both coils are assumed to quench simultaneously. The inductances are tabulated in the row of Table 2.5 labeled 'present'. Because of the poor magnetic coupling, the aluminum bobbin is not an important gain in protecting the coils during a quench.

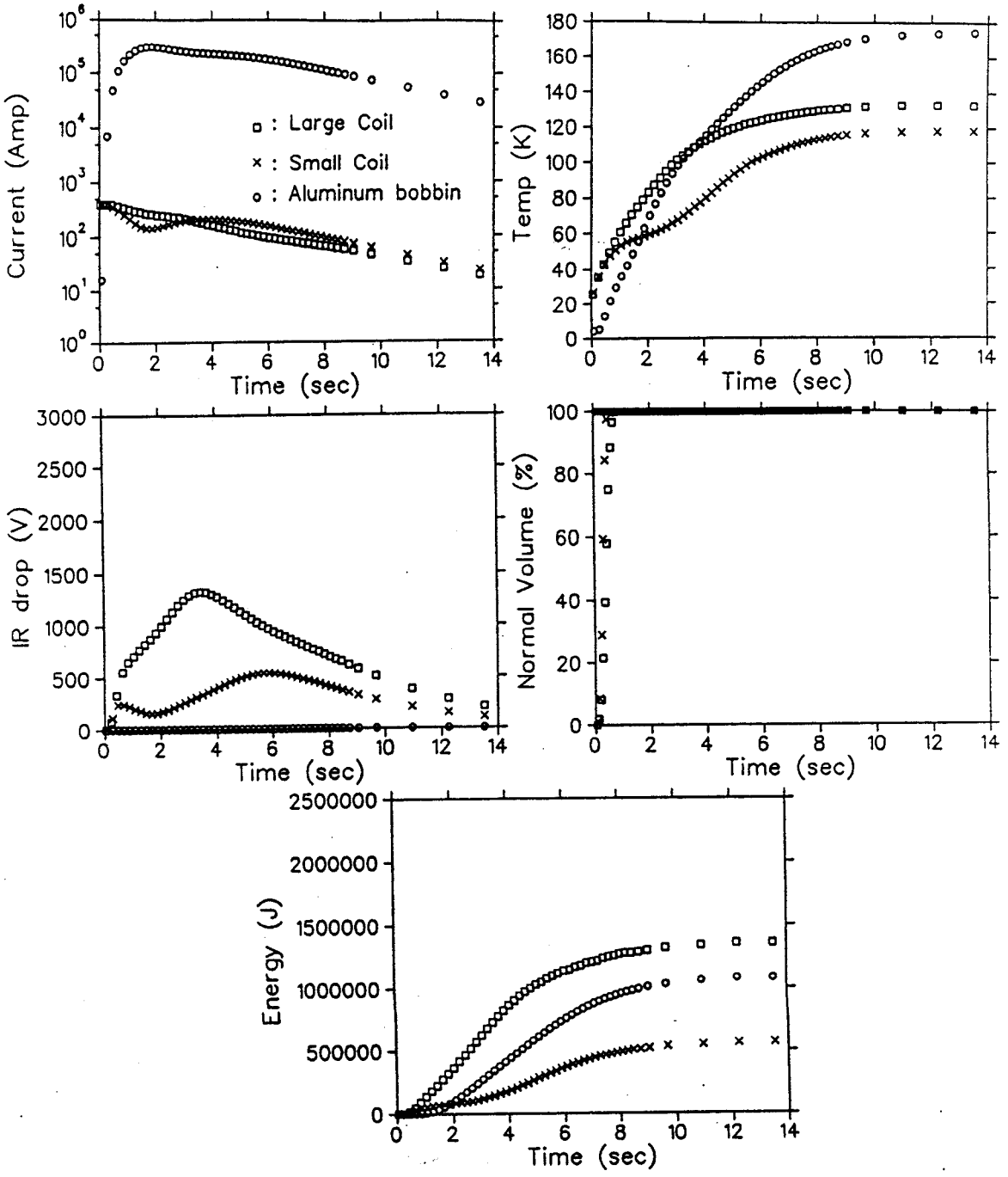

Figure 2.10: With the larger $k_{13}(=\frac{M_{13}}{\sqrt{L_1 L_3}})$ and k_{23} assumed in the last row of Table 2.5, (which can be achieved by radially thinner coils than the 8 T coils) a large portion of the stored energy is transferred to the aluminum bobbin. A reduction of hot spot temperature and IR drop is noticeable, when compared with those in Figure 2.8 & 2.9

Table 2.5: Self inductances of the coils and aluminum bobbin, and mutual inductances computed with POISSON. The row labeled 'Present' displays the inductances for the Figure 2.9 coil configuration. In the 'Assumed' line, the mutual inductances of the coils to the bobbin are assumed to be larger, such as might be achieved with thin coils as described in the text.

	L_1(large coil)	L_2(small coil)	L_3(Al bobbin)	M_{12}	M_{23}	M_{13}
Present	21.6	6.47	1.2×10^{-5}	4.91	0.0017	0.0043
Assumed	21.6	6.47	1.2×10^{-5}	4.91	0.0068	0.011

For the aluminum bobbin to function effectively as a quench protection, the magnetic coupling coefficient ($k=\frac{M_{12}}{\sqrt{L_1 L_2}}$) should be close to 1, which can be realized by a thin coil ($\Delta r \ll r$, where Δr is the coil thickness, and r the mean radius of the coil), but not in radially thick coils such as in the 8 T magnet. To quantitatively show the effect of magnetic coupling on energy transfer, a second calculation was made with the 8 T coils assumed to be closely coupled to the bobbin by larger mutual inductances as given in the row labeled 'Assumed' of Table 2.5; quench analysis results in this situation are shown in Figure 2.10. The energy shift is faster so that the hot spot temperature and the voltage drop are noticeably reduced. The bobbin heating speeds up the quench propagation by inducing a quench in regions remote from the quench origin before the quench propagates through the coil, which reduces the danger of overheating in the region of the quench origin. This is a quench protection strategy known as 'quench back' [Gre84] which is frequently used in large high energy physics detector solenoids. (Heaters can serve a similar purpose in an active fashion, and are employed for long, series connected magnets such as the SSC and HERA [MeB87].)

Reviewing the above results, it was concluded that the shorted circuit element given by high-conductivity aluminum does not appreciably improve the quench behavior of the 8 T magnet. Additionally, the use of the large differential thermal contraction of aluminum to free the coil is unnecessary if a removable winding form

is used. A stainless steel (304) helium vessel and a removable winding form were therefore chosen for the 8 T magnet because of ductility at low temperature, ease of welding, and low cost compared to a bimetal bore tube.

K Selection of design operating current

The 400 A design operating current of the 8 T magnet was decided after considering the coil behavior during a quench, which is acceptable at 400 A and the trade-off between heat leak and coil quench response. Larger operating currents (and smaller inductances) allow faster coil response to voltage changes at the expense of larger heat leaks through the current leads. For these magnets, current leads usually dominate the total 4 K heat leak since the heat leak of an optimized, 4 K to 300 K, gas cooled current lead is approximately 1 mW/A [Lec86]. Experience from other magnets was also a factor in the operating current decision, including taking into account the effect of the wire size on the conductor preload and on the winding time. The 400 A of the 8 T coil is in fact between the 200 A of the Harper cyclotron and the 700 A of the K500, and similar to the 500 A current of the S800 spectrograph.

L Stray magnetic fields

Stray fields from high field magnets can be hazardous to human beings, and also to electronic devices, vacuum pumps, etc. in the vicinity. A design goal for the 8 T magnet was then to reduce the stray field strength to less than 30 gauss beyond the radius of two meters. (This choice was arbitrary since the requirements of stray field reduction rely on the particular application and location of the magnet; NSCL research cyclotron magnets as an example have much higher fringe fields.)

Two different methods for controlling the fringe field were considered. The first method uses sets of reverse current coils located on the outside of the yoke to reduce

the stray fields, which is known as active shielding [Haw90]; the upper part of Figure 2.11 shows a typical active shielding configuration. The second method simply makes the return yoke of the magnet sufficiently thick to reduce flux leakage to specified tolerance levels.

A disadvantage of the active shielding method is that the main coils need additional amp-turns to compensate for the reverse magneto-motive-force from the shield coils. More importantly, a complicated magnet structure could be costly for either room temperature or superconducting reverse current coils. Most magnets then use yoke shielding due to its effectiveness and simplicity, even though a significant mass increase is unavoidably entailed. For the 8 T magnet, yoke sizes were adjusted to satisfy our stray field requirement using a simple cylindrical yoke and calculating the field with the code POISSON. To further minimize mass, the yoke could be contoured (corners rounded, etc) to give a more uniform flux density [Ish87]; the result would however be a much more complicated shape than the simple pillbox shape, and this makes such a flux optimization design not economically attractive.

A simple cylindrical yoke with thickness to give stray fields meeting the design specification at 8 tesla is shown in Figure 2.12, and compared with the active shielding results of Figure 2.11. The thicker yoke does not greatly increase the absolute mass due to the small magnet size.

Costs of the two options are compared considering only additional steel and superconductors, and tabulated in Table 2.6 for the magnet configurations of Figures 2.11 & 12. For the 8 T magnet, the active shielding scheme costs significantly more, and the yoke shielding option was therefore chosen.

Another important external field design characteristic is the magnetic force exerted by the external field on nearby magnetic objects. To assess this problem the radius

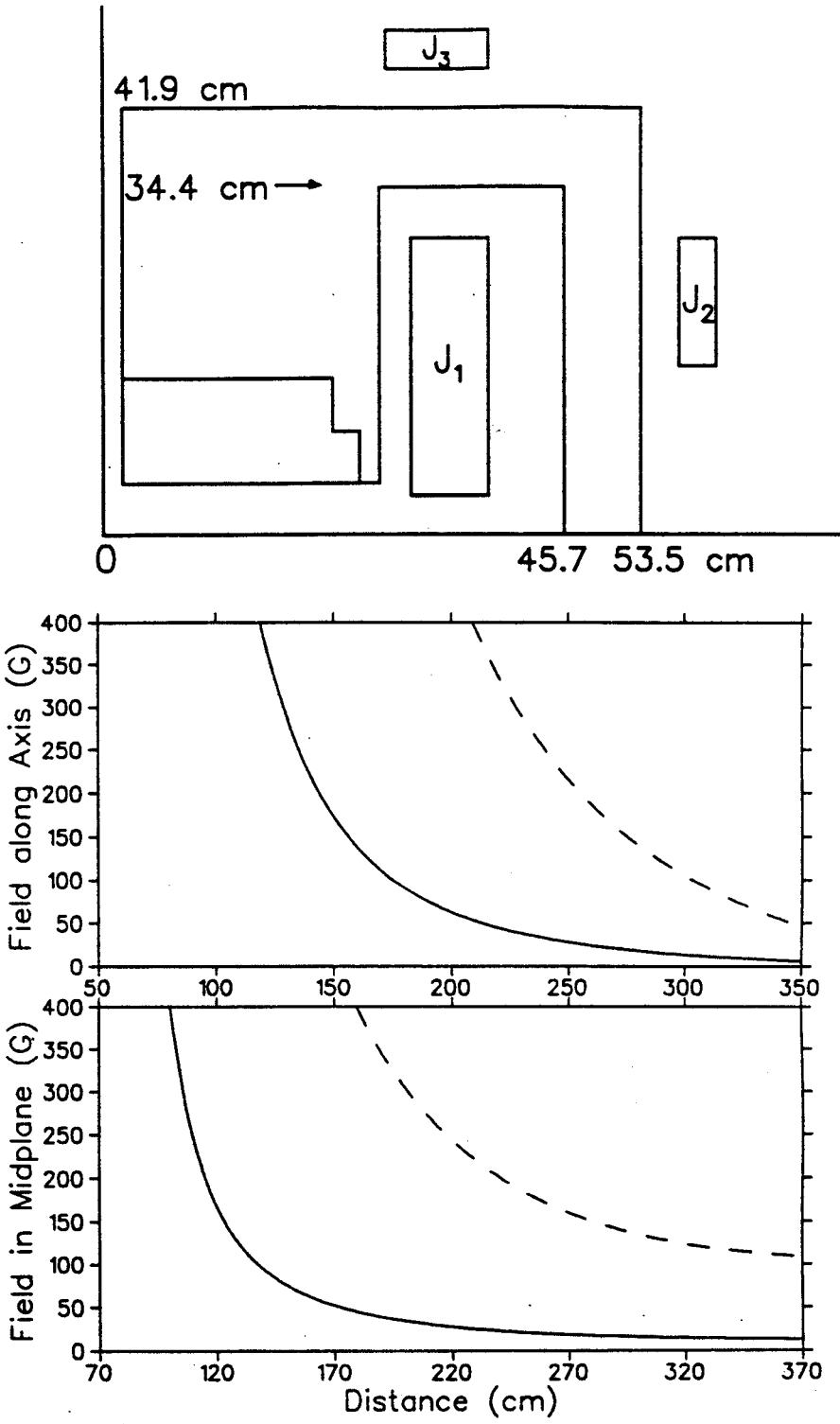

Figure 2.11: A cross section of a quarter of the magnet is shown with reverse current coils on the outside of the yoke, which is known as active shielding. The stray fields are reduced in both radial and axial directions. The current densities of each coil are: J_1= 13,950 amp/cm^2, J_2= -13,950 amp/cm^2, and J_3= -7750 amp/cm^2. The dashed line is the field without reverse current coils, and the solid line with these coils in use. The yoke is thinner than the yoke shielding case.

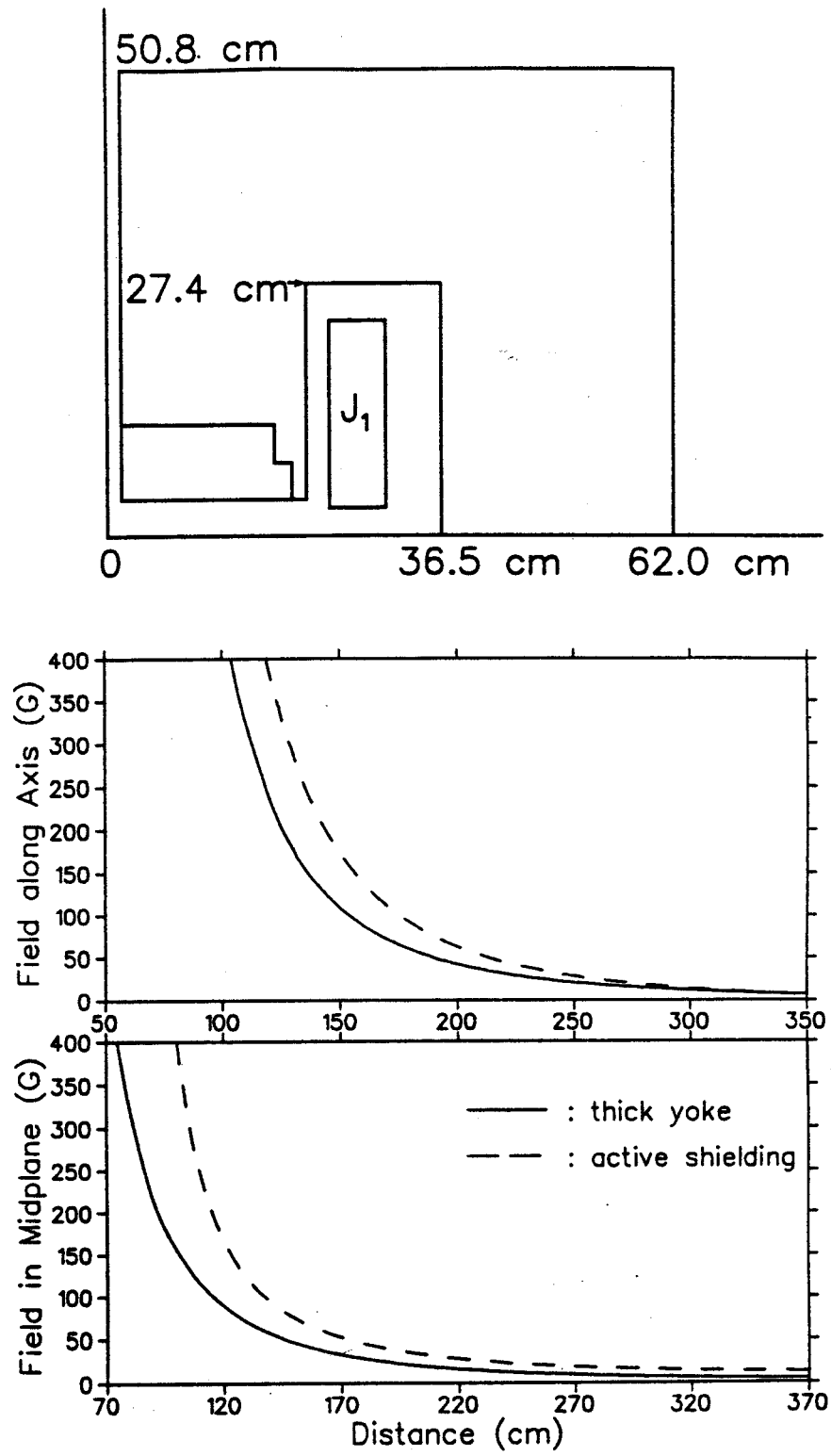

Figure 2.12: The yoke is thickened to confine the flux. The current density is 13,950 amp/cm^2. The solid line is the field with a thick yoke, and the dashed line with the active shielding of Figure 2.11. Both stray fields roughly meet our criterion, with the active shielding significantly less effective close to the magnet.

Table 2.6: Cost comparison of yoke and active shielding of stray fields considering only additional steel and superconductors. Unit prices of steel and superconductor come from the 8 T magnet cost.

	thick yoke shielding	active shielding
Unit price	\$2 /lb	\$0.002/A ft
Addition	3.6 tons	400 A, 51,000ft
Cost	\$16,000	\$41,000

at which the magnetic force equals the gravitational force (the 'lifting' condition) was roughly estimated; for 'long' objects like a steel wrench, the lifting criterion on the field is given by Moon [Moo84].

$$B\frac{dB}{dx} \geq 5.4 \times 10^{-3} tesla^2/m \tag{2.12}$$

An experimental test of this effect was performed in the median plane, with the internal main field at 7 tesla; in this run, condition (2.12) was satisfied at a radius of 81 cm for an object with width/length$\simeq$ 0.2, whereas the measured lifting condition radius was approximately 90 cm.

II Design of magnet components

A Support links

The support link of a superconducting magnet should be strong enough to sustain possible off-centering forces, and it should be a poor heat conductor in order to reduce the heat influx into the liquid helium. The usual choices of materials satisfying both conditions are composites, whose fibers are available in various forms [Ree83]. Among them, S- and E-glasses are the most commonly used. The commercial products containing these fiberglasses are G-10 (E-glass), and Scotchply (S-glass, product of 3M). The properties of the two products are compared in Table 2.7. The S-glass/epoxy is usually preferred, as the ratio of strength to thermal conductivity of S-glass is about twice as high as that of E-glass [Ban91]. The K1200 and Harper hospital superconducting (SC-) cyclotrons and the SC-ECR ion source built in this lab have employed this product for their links.

Mechanical details of the support link system of the 8 T magnet are shown in Figure 2.13. The vertical links support both the helium tank and 80 K radiation shields. The weight supported by the top three links is about 800 kg.

The vertical links of other MSU SC-cyclotron magnets are usually attached to the top and bottom plates of the helium vessel. Unlike these, both horizontal and vertical links of the 8 T magnet are attached to the midplane ring since the coils are free from the inner bore tube, and welded onto the ring at the outer coil edge (see section 2.II.D). As a result, the narrow radial gap between the helium vessel and the heat shield restricts Scotchply links from being used for the vertical support since they are rather bulky as being wound into a belt shape. G-10 bars, which are radially thin and azimuthally wide when installed in the magnet, were chosen for the vertical links.

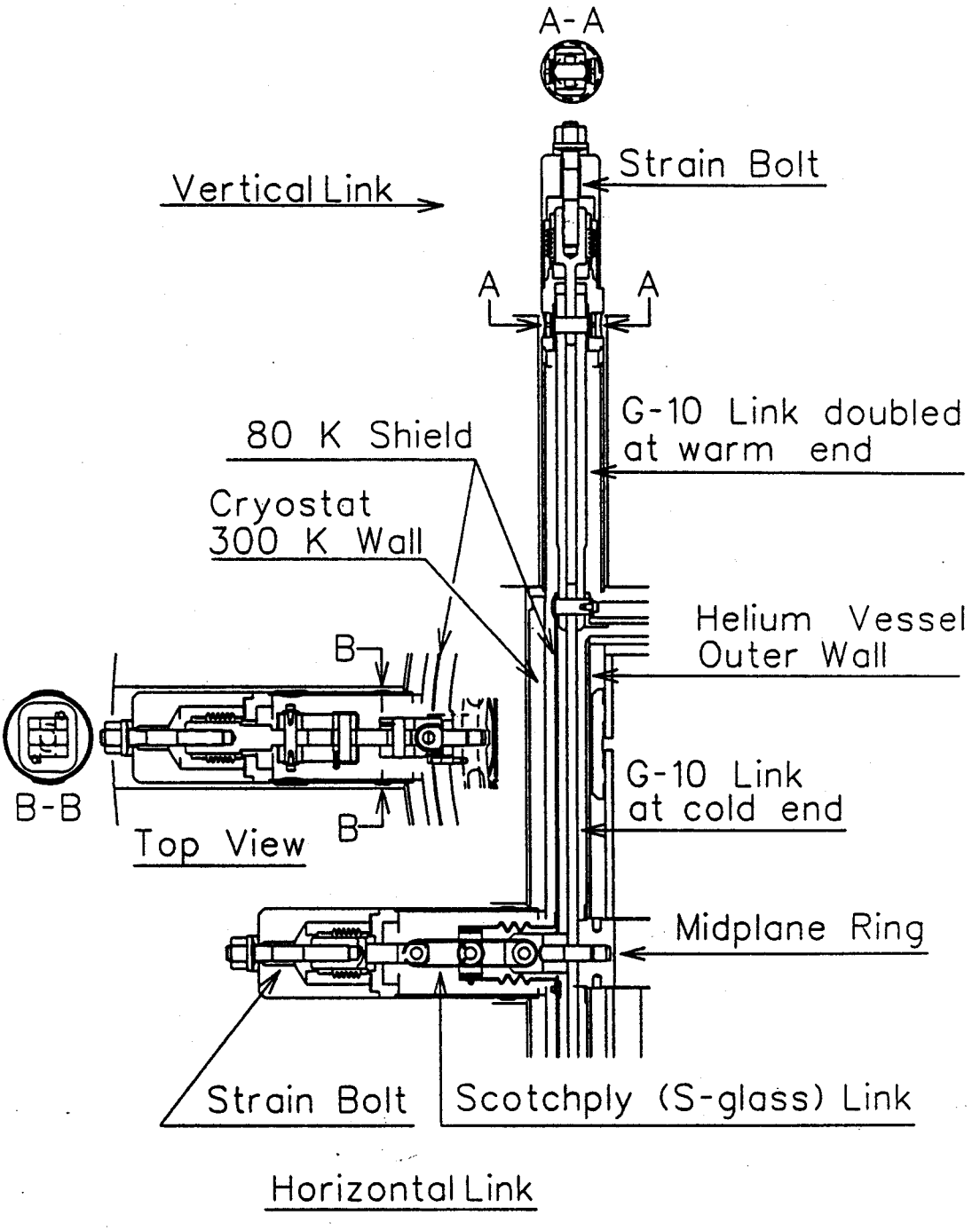

Figure 2.13: Horizontal and vertical link assemblies in the 8 T magnet. Both links are doubled at the warm end to match with the strength at the cold end. Strain bolts are employed to read the forces on the links.

Table 2.7: Comparison of G-10, and Scotchply

Properties	Temperature	Scotchply	G-10
Young's modulus	300 K	48.0 GPa	28.0 GPa
	4 K	N/A	35.9 GPa
Tensile strength	300 K	1790 MPa	415 MPa

In link assembly, the link pin at the warm end can be the weakest part. which takes 'double shear' stress (two shear planes in the pin, refer [Ger90]). Especially, the horizontal link pin is weaker than the vertical link pin because of the smaller pin diameter; 1.27 cm, 0.95 cm for the vertical and horizontal link pins, respectively. The shear stress at a tension of 3.8×10^4 N (the ultimate tensile strength (UTS) of the horizontal link unit, see section 2.II.C), is

$$\tau = \frac{Tension}{2A} = 39{,}000 \text{ psi},$$

where A is the cross-sectional area of the pin. The shear stress is greater than the ultimate shear strength of the standard 304 stainless steel (material strengths in shear are usually half as large as those in tension, and the UTS of 304 stainless steel is ~30,000 psi at 300 K). Titanium alloy pins were used, whose UTS is rated higher than 100,000 psi.

B Spring constants of the link system

For the stable coil support, the spring constant of the link assembly should be larger than that of the magnetic off-centering force. If this condition is not satisfied, the coil continues to de-center in response to an initial perturbation, and link breakage/coil damage would usually result. The spring constants of the link assembly and of magnetic off-centering forces due to the misalignment of the coil relative to the magnet center were estimated for both vertical and horizontal directions. The spring con-

stants were also measured as a function of current in the 8 T magnet system with all links connected, and are described in section 4.I.

For a rough first approximation, the vertical off-centering force can be estimated using the image current method. When an infinitely long current filament (current: I) is placed midway between two ferromagnetic walls with infinite permeability, the off-centering force per unit length (F) was worked out by Hague [Moo84] as shown in the illustration below.

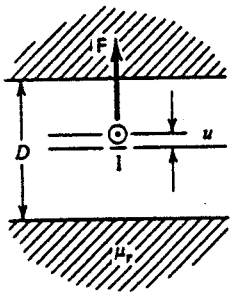

$$F = \frac{\mu_0 I^2}{4\pi} \frac{\pi}{D} \tan \frac{\pi u}{D} \quad \text{(N/m)}$$

$$(\mu_r \to \infty)$$

Because of the two walls, the image filaments due to one wall create image filaments behind the other wall, which results in an infinite array of filaments. The analytic formula was applied to the 8 T magnet case for a small displacement; $F/u \times 2\pi R \approx \mu_0 \pi I_{coil} I_{image}/4D^2 \times 2\pi R = 4.2 \times 10^7$ N/m, where R is the average radius of the coil, D (57.4 cm) is the yoke gap in the coil region, $I_{coil} = 3 \times 10^6$ A at 8 tesla, and $I_{image} = I_{coil}$. The approximation neglects effects of the cylindrical geometry, the partially saturated state of the iron, and the marked deviation from flatness of the coil cavity. The result never-the-less provides an initial order-of-magnitude sense for the spring constant needed in the support system design.

For a more accurate result, the program POISSON was used to calculate the vertical off-centering force by directly introducing an axial coil displacement. Table 2.8 shows the forces and spring constants from this study for two different coil displacements at the maximum design current. The off-centering forces are almost linear for different but small displacements, which agrees with analytic reasoning.

Table 2.8: Spring constants of a vertical off-centering force calculated by POISSON at 8 tesla.

Displacement	1.2 mm	2.5 mm
Off-centering force	1.4×10^4 N	3.1×10^4 N
Spring constant	1.1×10^7 N/m	1.3×10^7 N/m

To test the codes for the accuracy of force calculations, forces in the centered coils in the magnet were calculated with POISSON, and then compared to the TOSCA [Tos] calculations. Computations by the two different codes relatively agreed well in this case, but for the off-centered coils, significant differences in both calculated axial and radial off-centering forces were observed. Usually, accurate estimates of off-centering forces are difficult to achieve because: 1) off-centering forces are much smaller than the coil forces, and 2) grid sizes in the finite element analysis are often larger than the coil displacements so that the fields are not accurately described.

An analytic approximation was made for the radial off-centering force, which considers the yoke and poles to be a set of dipole moments. The interactions between the coil and yoke and between the coil and pole tip are independently considered.

The dipole moment of the yoke was subdivided into four effective dipole moments which interacts with the coil dipole ($M_{yoke} \simeq \frac{1}{4} J_{saturation} Ah$, where A is the total yoke cross-sectional area, h is the yoke height, and $J_{saturation} = 1.7\times10^6$ A/m). The force between two anti-parallel dipoles is given in text books ($\vec{F} = (\vec{m_1}\cdot\nabla)\vec{B}$, where m_1 is the dipole moment, and B is the dipole field from m_2, see p.182 in [Jac75]). Then the off-centering force due to two yoke dipoles, which are located across the coil in the direction of coil displacement interacting with the coil dipole is given below to first order;

$$\delta F_h = M_{coil} M_{yoke} \frac{\mu_0}{4\pi} \frac{12}{r^5} \delta r, \tag{2.13}$$

where M_{coil} is the dipole moment of the coil at 8 tesla, and δr is the coil displacement relative to the magnet's center. The spring constant ($\delta F_h/\delta r$) by this approximation is about 0.9×10^7 N/m.

The spring constant due to the interaction between the pole and coil is also calculated using the equation, $\vec{F}= (\vec{m}\cdot\nabla)\vec{B}$. However, in this case, the gradient of the coil field was numerically obtained with POISSON, and the dipole moment, m, comes from the off-centered portion of the pole tips with respect to the coil center. Assuming saturated pole tips at 8 tesla, the spring constant estimate is about 0.6 $\times10^7$ N/m. Therefore, the spring constant of the radial magnetic off-centering force including both the coil/yoke and coil/pole tip interactions is 1.5 $\times10^7$ N/m.

The spring constants of the link assembly were calculated or measured for the vertical and horizontal links, respectively, to compare to the spring constants from the magnetic off-centering forces. The spring constant of an entire vertical link assembly (composed of a single link unit at the cold end and a doubled link unit at the warm end) is related to the spring constant of a single link by the following equation;

$$1/k_{cold} + 1/2k_{warm} = 1/k_{link\ assembly}, \tag{2.14}$$

where k_{cold} is the spring constant of the cold end, and k_{warm} is of the warm end. The $k_{vertical}$ of a link assembly is about 1.5 $\times10^7$ N/m, and for six link assemblies together (three upper, three lower), k_{eff}=9 $\times10^7$ N/m, which is comfortably higher than the spring constants in Table 2.8 for either displacement. The spring constant of a horizontal link unit was measured using a strain bolt and two dial indicators in a test stand, The spring constant of an entire link assembly which was computed using Eq.2.1 was 2.0×10^7 N/m. The overall spring constant for the three link assemblies

together at 120° spacing is then k_{eff}=3.0 $\times 10^7$ N/m, which is larger than the dipole approximation.

C Test of sample links

Irrespective of the spring constant, a maximum on the allowed coil displacement is set by the breaking strength of the links. Usually this is limited by the strength at the link attachment point where the stress concentration resulting from the discontinuity on the joint is the key factor requiring optimization. To confirm this detail of the design, the G-10 vertical link was studied by testing two kinds of joints [Kim90] shown in Figure 2.14: 1) bolted and bonded (combination) joint, and 2) pin joint. The measured tensile strength of the combination joint was no higher than that of a pin joint. Arrangements of bolts and bolt sizes in the combination joint were not throughly optimized since the pin joint was generally preferred for the 8 T magnet due to its pivot action.

To reduce the stress concentration around the joint area, the link attachment region is shaped as seen from the test link configuration in Figure 2.14. The pin-hole size (d), the width of the link attachment region (w), and the shortest distance (h) from the hole to the end of the link are the parameters which are related to stress concentration factor. Considering the 2.5 cm wide link body, which was roughly decided from the strength requirement, the pin-hole size (d) was first set at 1.27 cm, and then w was optimized; the breaking strength of each vertical link assembly was decided to be 4×10^4 N, which would allow more than 5 mm off-centering without link breakage. Several different widths were tried, and it was concluded that there was no significant tensile strength increase beyond the width of 3.8 cm with h of 2 cm (h was roughly determined as a minimum distance not to greatly reduce the link strength for d/w$\simeq$0.4). This optimization was rather approximate, and could be improved by

Applied load	Pin joint
1400 kg	No samples are damaged. Linear and reversible up to this point.
1530 kg	Pin hole becomes elongated. Prefracture stress concentration lines are dimly shown.
1670 kg	High stress region appears clearly. All samples seem to be damaged
1760 kg	Several samples are broken
1800 kg	All samples are broken
	Combination joint
1400 kg	Broken, no observation is made since the breaking location is behind the fixture

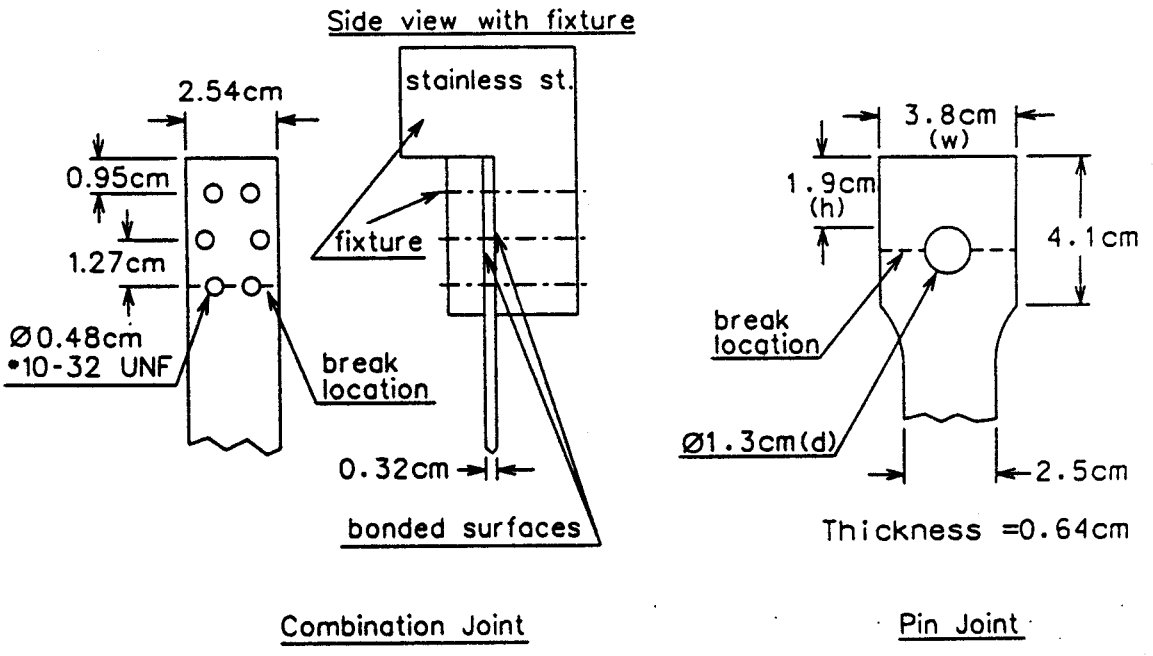

Figure 2.14: Configurations of tentative G-10 links with a combination joint and a pin joint. Tensile strengths of the links for both joints were tested, and are summarized in the table. Only one sample was tested for the combination joint, and six samples for the pin joint.

adjusting the d, in addition to the w and h.

Six G-10 link samples with a pin joint shown in Figure 2.14 were tested, and general characteristics are summarized in the table in Figure 2.14. The stress concentration factor [Coo85]) of the link joint is about 3; K= σ_{max}/ σ_{nom}, where σ_{max} is the ultimate tensile strength of G-10 ($\simeq$ 49 kpsi), and σ_{nom} is the average tensile stress at the link breakage ($\simeq$ 16 kpsi).

Since stress concentration data on the pin joint were not available for composites such as G-10, the link design was performed by experimental tests rather than by computations. However, a simple design evaluation of the test link was made using the homogeneous material data before finalizing the actual link design for the 8 T magnet. The stress concentration curve in reference [Fro40] was fitted by polynomials of d/w for h/w$\simeq$0.7: K=30(d/w)^2-33(d/w)+11, and the joint strength is given as follows;

$$\text{Strength of joint} \propto \frac{w-d}{K} \tag{2.15}$$

When using the above equations, the optimum w is 2.8 cm for a d of 1.27 cm, which means that the width of the tentative link (w=3.8 cm) is wider than the optimized one, which is usually useful for the strength.

To ease the design and fabrication, however, the actual 8 T magnet vertical links differ from the tested sample links; the link width (w) was reduced to a uniform 2.85 cm without enlarged pin joint area, the thickness was increased to 0.79 cm, and G-10CR instead of G-10 was used to keep the breaking strength near 2×10^4 N at 300 K (the tensile strengths are 49 kpsi, 56 kpsi for G-10 and G-10CR, respectively [Spa]). The tensile strength of the actual G-10 link was not measured because of the consistent test results for different sample links, which allowed confident use of inferred tensile strength of 2×10^4 N without further testing.

The horizontal links were designed to be the same links used for the SC-ECR [Ecr]. Therefore, a particular study to find the optimum shape was not made. The tensile strengths of two samples which had different number of layers (7 and 12) were measured and compared to results from the ECR group. A tensile breaking stress of 130,000 psi was obtained with the 7 layer link, which was the same number of layer with the ECR link and similar in breaking stress. (The 12 layer link broke at 50,000 psi at which the outer layers initiate the breakage; the link might not be properly fabricated.) All of the horizontal links actually used for the 8 T magnet were checked by a 70,000 psi stress, and no damage was observed. Each link can support up to 3.8×10^4 N (at room temperature – it would presumably be higher at 80 K), but the maximum load is preferably limited to below 2.6 $\times10^4$ N because some fibers seem to break at higher loads, which may cause the tensile strength reduction after many loading cycles.

D Median plane structure of the 8 T coil

The design of the midplane structure in a superconducting cyclotron magnet needs to meet a contradictory requirement; it must support large axial clamping forces, and yet allow space for room temperature penetrations into the main field region and for thermal insulation of these penetrations. The midplane structure of the 8 T magnet follows the design concept utilized for other MSU cyclotron magnets: strong support of the axial force and minimal allowance of room temperature penetrations (see [Ago86] for different design). A technical difficulty involved in the usual MSU design is that the space for thermal insulation is quite restricted, which might introduce a large heat leak.

Another design feature of the midplane structure is related to the coil motion. A low friction slip plane is frequently employed to allow coil sliding against the midplane

support when coils are energized. The method needs a thermal barrier between superconductor and slip plane since the heat generated by frictional motion must diffuse away; a low friction, smooth slip plane is also essential. In reality, it is however quite difficult to insure smooth low friction sliding. Rather than resorting to this uncertain design scheme, the midplane structure of the 8 T magnet is designed to be weak for radial expansion so that it moves together with the coil. Stacks of the 1.6 mm thick aluminum plates fill the space in the midplane as shown in Figure 2.15, and they are sandwiched between two thin G-10 plates (1.2 mm thick). The resulting radial stiffness of the median plane structure is determined by two G-10 plates rather than by aluminum stacks (since the stacks can freely stretch azimuthally and radially).

Though it is clearly probable that the G-10 plate will expand with the coil by frictional force without coil sliding, numerical calculations are made to analytically demonstrate this. The body force in the plate (F_r), which radially expands the plate, originates from the frictional force due to the axial magnetic pressure, P_a; $dF_r = \mu P_a 2\pi r dr$ on the area of $2\pi r dr$, where μ is the frictional coefficient. The differential equation of force equilibrium (see p.90 of [Coo85]) is established by the radial, hoop stresses in the plate ($\sigma_r(r)$, $\sigma_\theta(r)$), and by the radial body force, with P_a assumed to be independent of r;

$$\frac{d\sigma_r}{dr} + \frac{\sigma_r - \sigma_\theta}{r} + \frac{\mu P_a}{t} = 0, \tag{2.16}$$

where t is the plate thickness.

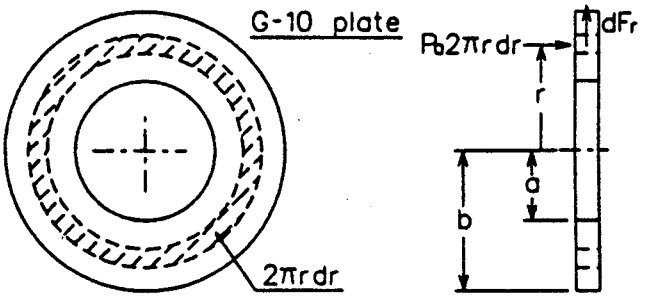

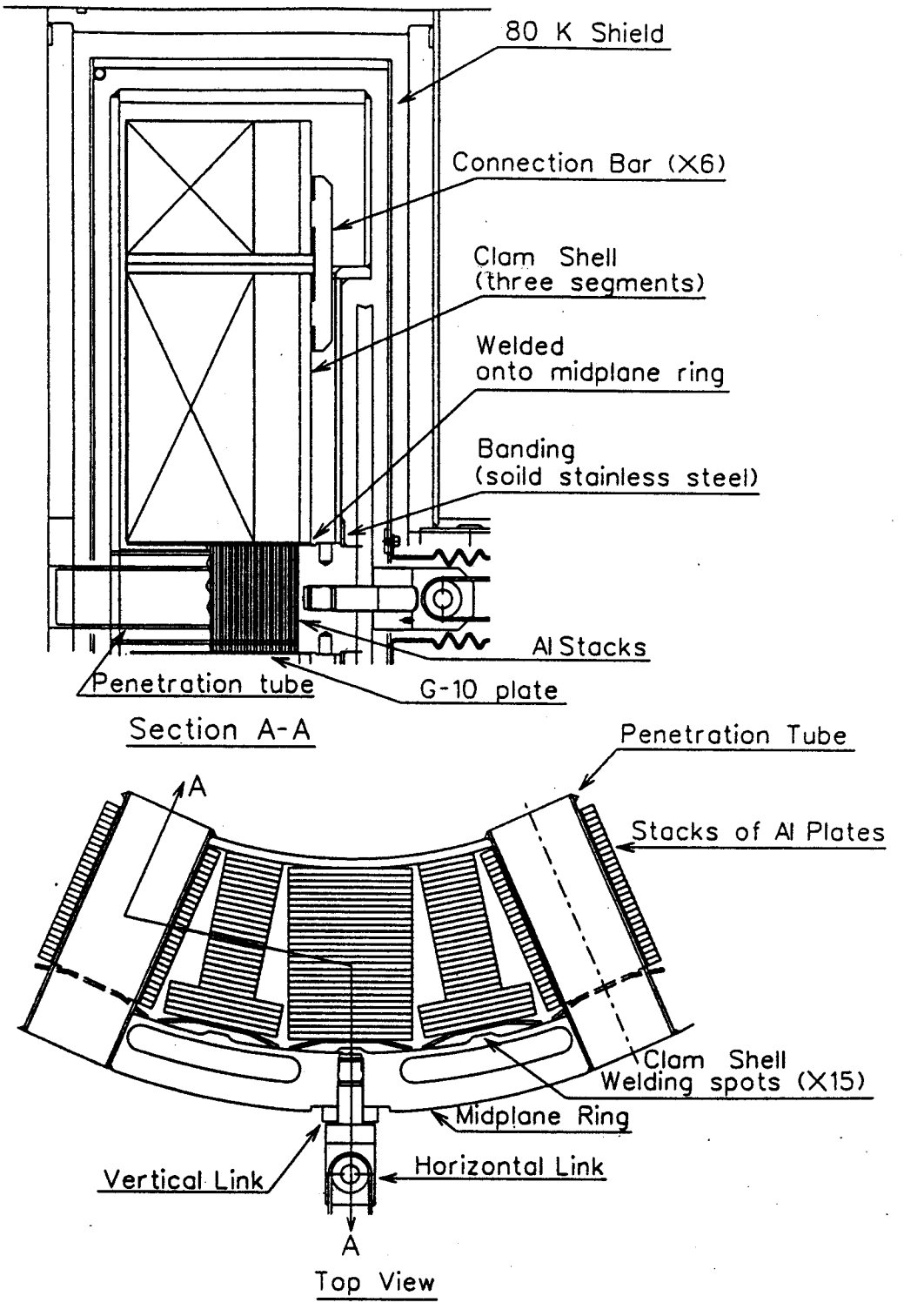

Figure 2.15: Top view of a section of the midplane structure, and a side view to show its attachment to the coil. There are twelve penetration holes.

From Hooke's law, the relationships between stress and strain are written below [Coo85];

$$\sigma_r = \frac{E}{1-\nu^2}(\epsilon_r + \nu\epsilon_\theta) \qquad \sigma_\theta = \frac{E}{1-\nu^2}(\epsilon_\theta + \nu\epsilon_r), \tag{2.17}$$

where ν is the Poisson's ratio. The strains are determined by displacements, u(r);

$$\epsilon_r = \frac{du}{dr}, \qquad \epsilon_\theta = \frac{u}{r} \tag{2.18}$$

Substitution of Eq.2.17 and Eq.2.18 into Eq.2.16 yields

$$\frac{d}{dr}(\frac{1}{r}\frac{d}{dr}(ur)) = -\frac{1-\nu^2}{E}\frac{\mu P_a}{t} \tag{2.19}$$

The solution is then

$$u = C_1 r + \frac{C_2}{r} - \frac{(1-\nu^2)\mu P_a}{3Et} r^2 \tag{2.20}$$

From the boundary conditions, $\sigma_r(a) = \sigma_r(b) = 0$, the coefficients C_1, and C_2 are obtained;

$$C_1 = \frac{(1+\nu)(2+\nu)}{E}\frac{\mu P_a}{3t}\frac{a^3-b^3}{a^2-b^2} \qquad C_2 = \frac{(1+\nu)(2+\nu)}{E}\frac{\mu P_a}{3t}\frac{a^2b^2}{a+b} \tag{2.21}$$

The displacements of the G-10 plate can be obtained from Eq.2.20 for a given axial pressure, P_a (~3000 psi, at 8 tesla). Calculations approximately predict that the plate displacements by the stationary frictional force are larger than the coil displacements at any excitation, which means that the plate will certainly expand together with the coil without sliding against each other. The frictional force with μ=0.3 for instance can expand the plate roughly by 0.8 mm at 8 tesla, while the coil expands only 0.25 mm by radial magnetic force due to its high stiffness, which was calculated by the program STANSOL.

E Current leads

Current leads are available as commercial products. However, the one used in the 8 T magnet was designed and built in house because commercial leads are bulky,

requiring larger holes in the yoke of the 8 T magnet (a standard commercial lead pair rated at 500 A is in two separate tubes of 1.27 cm O.D.- American Magnetics Inc., while an 8 T magnet current lead pair is in a tube of 1.59 cm O.D.).

Mechanical details of the 8 T magnet current leads are shown in Figure 2.16. The leads are made of superconductors like leads of many other magnets in this lab [Pur] (Cu:SC=2:1, 3 bundles of twisted 0.25 mm thick conductors, each bundle containing 147 individual wires cabled first into 3 wire clusters and then into two successive seven cluster groups (one surrounded by six)), rather than plain copper, which is in more frequent use in other institutions. Since the temperature at the cold end of current leads would be lower than the critical temperature, that section of the leads is in the superconducting state, reducing the ohmic heat. This feature would reduce the heat leak rather insignificantly, but it is still worthwhile to use.

An optimized shape of the leads which transfers minimum heat into LHe can be obtained for a given lead material when the thermal equilibrium equations are solved, as detailed in reference [Wil83]. For the copper which is the matrix material for superconductor, the optimum length to area ratio is given by M. Wilson;

$$\frac{I_0 X_0}{A} = 2.6 \times 10^7 \text{ A/m},$$

where I_0 is the maximum current, X_0 is the lead length, and A is the cross-sectional area. The configuration of the 8 T magnet current leads approximately corresponds to an optimized shape at 400 A if the twisting effect of the conductors is not considered (X_0= 100 cm, A= 14.9 mm^2, where A is only for the copper component of the superconducting strands). To calculate the optimal shape factor, a complete heat exchange between lead wires and boil-off helium gas is assumed, which is applicable when a sufficient cooling surface area is allowed. Using many stranded wires in the lead, a minimum cooling area is easily met, however, a longer and larger lead configuration is preferred to extend burnout time in the case of an accident which

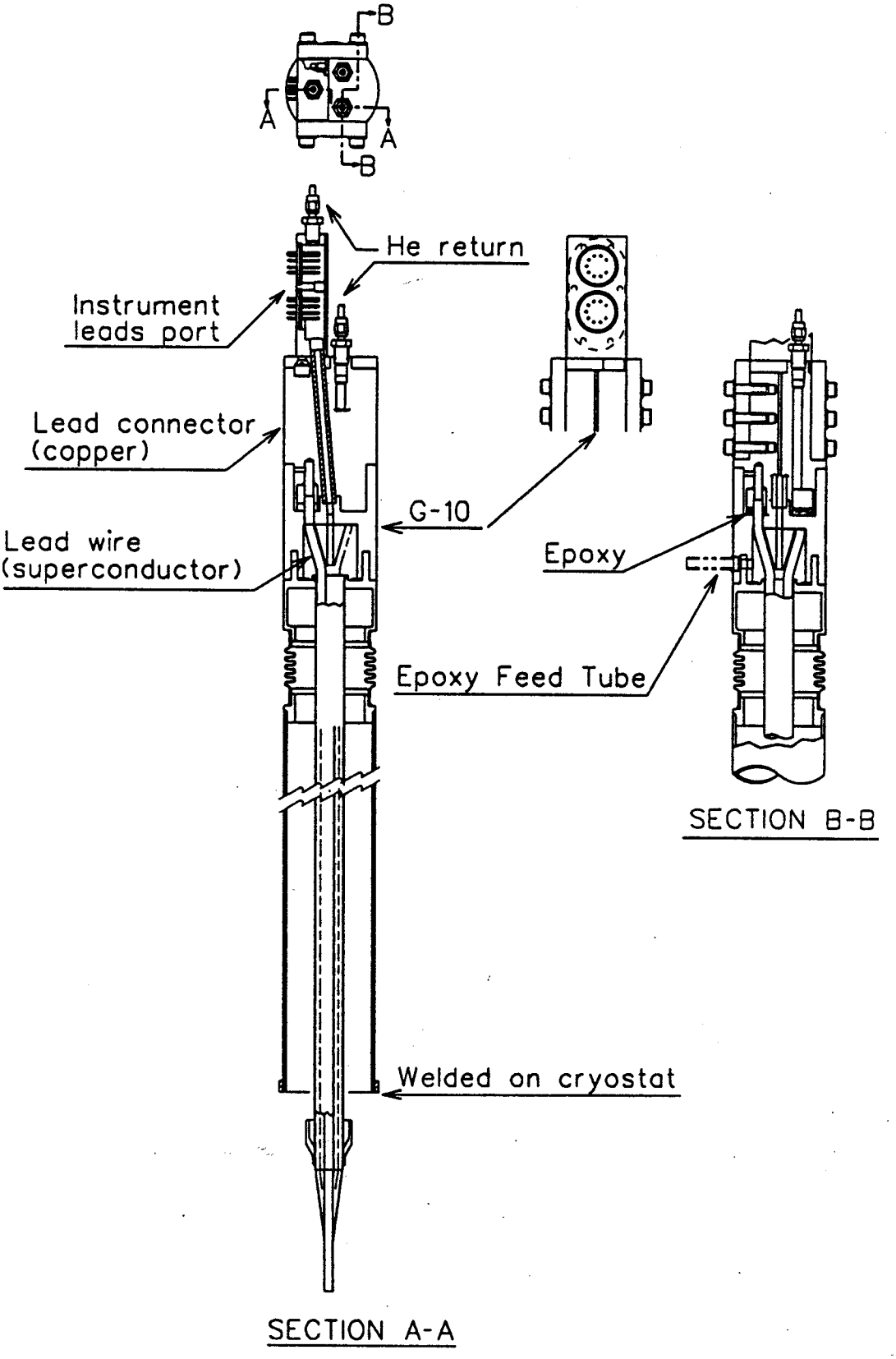

Figure 2.16: Cross-sectional views of the current leads of the 8 T magnet. Mechanical details are shown and noted.

cuts off helium flow. The length of 1 meter used for the 8 T magnet leads provides a robust lead as known from with other superconducting magnets.

A current leads with the same design as the 8 T magnet leads was built and tested in a 50 liter liquid helium vessel. The heat leak was measured as a function of current, and is plotted in Figure 2.17. The measurement includes the heat leak into the vessel itself, but it is not subtracted in the figure because of uncertain magnitude; the heat leak into the vessel sensitively depends on the pressure fluctuations in the return line of boil-off helium gas (a measured heat leak without pressure fluctuation effects is less than 0.1 W) [Kim92b]. The heat leak on a typical commercial 500 A current leads from American Magnetics Inc. [Ame] is also shown in Figure 2.17.

As an effort to reduce the heat leak through the current leads, high temperature superconductors (HTS) have been tried and reported as having promising results by other researchers [Nie93][Ued93]; the heat leak in HTS current leads with an intermediate heat sink was reduced 40 % compared to that in conventional optimized leads designed to carry 1 kA [Wu91]. Accessing the advanced technology involved in such leads would however have delayed the 8 T magnet project by a considerable amount, and so use of conventional leads was selected as the best system for the 8 T magnet situation.

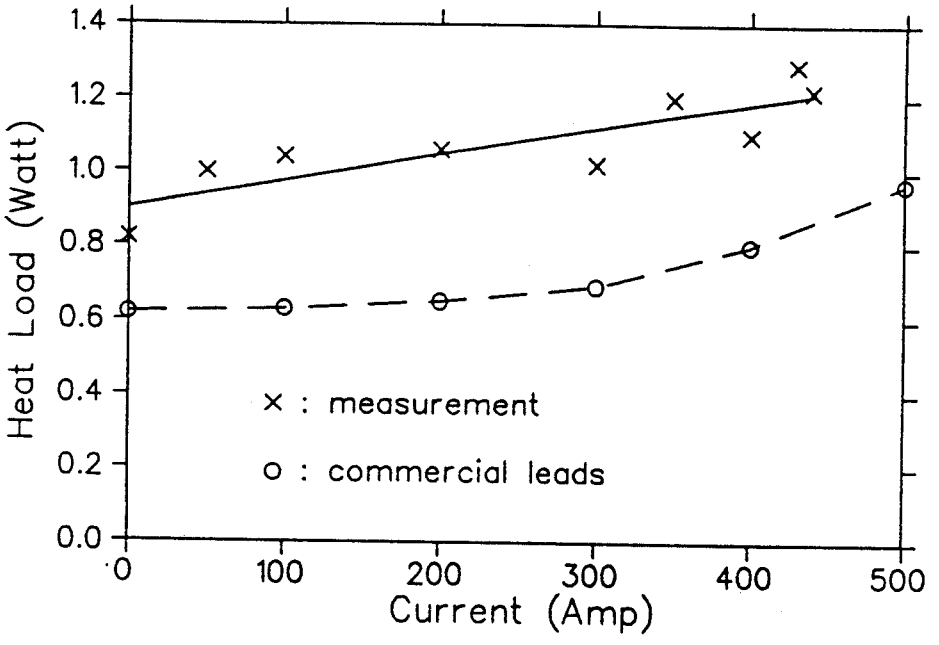

Figure 2.17: Heat leak as a function of current was measured in a 50 liter liquid helium vessel (cross). The heat leak of the vessel itself is included since its contribution was difficult to accurately estimate (roughly 0.1 W). The solid line is a fitted curve. The dashed line with circles is the heat leak of a typical commercial 500 A current leads [Ame].

Chapter 3

Construction of the 8 T magnet system

I Materials in the coil

The main constituents of the 8 T potted coils are the layer-to-layer insulation, the epoxy adhesive, the conductor insulation, and the metallic composite NbTi in Cu superconductor. In this section, properties of these materials are reviewed.

The coil to bobbin insulation is composed of five layers of 0.13 mm thick Mylar. Multiple layers are employed to utilize the superior dielectric strength per unit thickness compared to a thick insulator of a single layer (pin holes are unlikely to line up in successive layers). To cover the corners of the coil effectively, 'angled' layers of Mylar were formed by a heated forming die (Figure 3.1), which shapes the Mylar into a circular 'bracket' (cylinder plus plane). Before the pressing process began, the aluminum forming tool was heated to 200°C which is close to the melting temperature of Mylar. This method was originally suggested by Dupont Corp. which noted that the stability of formed mylar is established only when heated close to its melting temperature. Some layers of Mylar were glued together with EPON 828 epoxy to increase their rigidity.

Between each layer of the coil, a sheet of epoxy impregnated paper was inserted

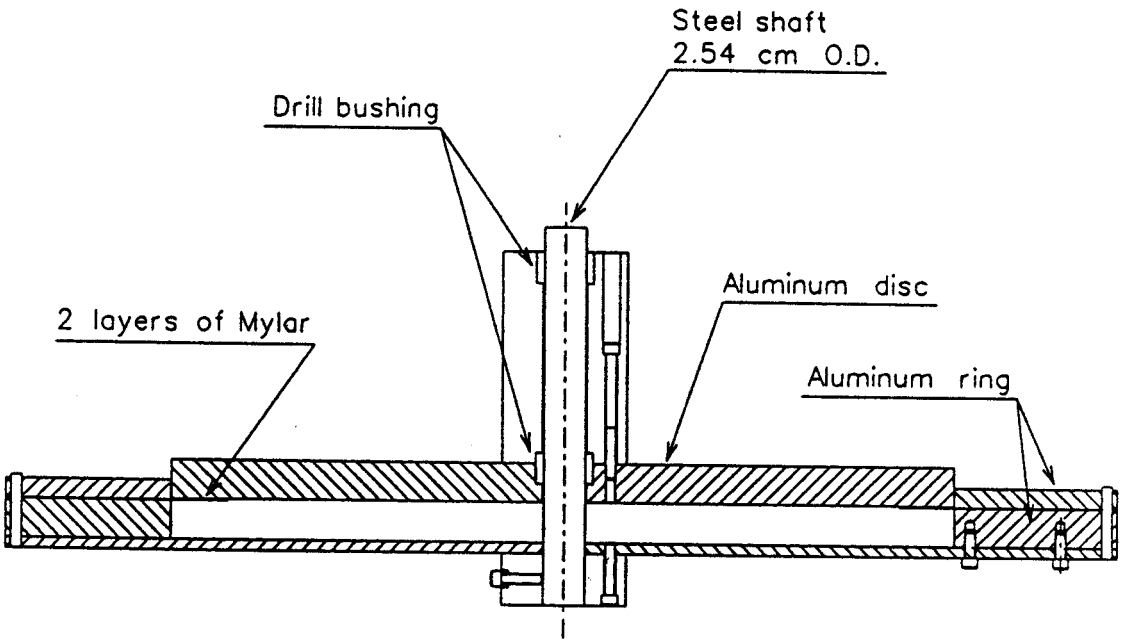

Figure 3.1: Mylar forming die. To cover the corners of the coil effectively, layers of Mylar were thermally formed.

Table 3.1: Properties of the 8 T conductor

Superconducting Alloy Composition	Nb–46.5 w/o Ti
Matrix material	OFHC Copper
Volume ratio Cu/SC	1.90 : 1
Twist length	2.54 cm
Bare Wire Size	1.05 mm × 2.03 mm
Insulated Wire Size	1.14 mm × 2.13 mm
Filament size and number	139 μm, 54
Critical current at 8 tesla, 4.2 K	650 A

to reinforce the conductor insulation. To control the amount of epoxy added on the paper, the paper was passed through a 0.25 mm wide slit after being soaked with Stycast 2850FT [Sty] epoxy in a pot.

Another function of the paper is to inhibit the propagation of epoxy cracks produced by thermal and electromagnetic stresses. In large scale magnets, fiberglass cloth pre-impregnated with epoxy has been used to achieve similar goals. That option was considered, but the crossply cloth commercially available was thicker (0.3 mm) than paper so that the overall current density decreases. (It was also more expensive.)

At each end of each layer, tapered G-10 pieces were used as layer transition spacers. They were cut from a sheet of G-10 stock with a saw blade installed in a horizontal milling machine, and hot formed so they would conform to the cylindrical curvature of the bobbin without significant added force. Reference [Kim92a] describes more details involving these spacers. With these spacers, the resulting coil winding is a true helix on every turn.

The major portion of the coil is filled with superconducting wire, the total volume of conductor in the coil (the packing factor) being about 75%. Table 3.1 lists properties of the conductor.

II Coil winding

The coil is the most delicate component of a superconducting magnet, and for the 8 T magnet significant effort was invested in carefully controlling each step of the coil winding process. Winding devices were carefully prepared and checked before the actual winding; a small test coil was first fabricated and many coil tests were made as winding progressed.

The central element of the winding system was a large lathe (82 cm diameter × 3.0 m bed length), which rotates the winding form and moves the tool carriage carrying the winding arm at the same speed as the winding layer advances; the lathe tool carriage supported both the conductor tensioner and a 'pusher' arm which compressed each turn against the previous turn. Other winding devices include the epoxy pot, a paper cutting device, the turn counting system, etc.

The tensioner is a device arranged to provide a constant winding tension which matches that of a reference spring. The operating principle is that a hydraulic motor feeds conductor onto the rotating coil form at a rate which holds the position of the tensioner carriage constant with respect to the constant force spring using the feedback signal from a linear potentiometer. As a result the wire, held by two V belts on the carriage, is always pulled on by the springs and therefore tensioned by the spring load in just the same way as it would be if the springs were solidly attached to the wire.

The pushing arm powered by pneumatic cylinders pushes the wire against the layer beneath it, and also laterally against the previous turn to wind tightly. The pressures in both directions are controlled by regulators. A downward (radial) pressure of about 10-15 psi was used, and 15-20 psi was for the side pressure (regulators are connected with air cylinders of 3.2 cm diameter and 3.8 cm diameter for downward and lateral

Table 3.2: Work days per coil set spent on actual winding

Work	Work progress rate	Days taken
Superconductor winding	6 layers/day	16
Lead outlet and insulation		2
Banding	9 layers/day	5
Preparations between two coils		2
Winding one coil set		25

pressures, respectively). The large lateral pressure is rather unusual compared to other MSU coils, but was thought to help tightly packing the wires.

The epoxy pot was borrowed from the coil winding tools used for the Harper Hospital cyclotron, but modified to accommodate the rollers to soak the paper with epoxy more thoroughly. The paper cutting device was newly built and employed a slide with a lead screw to control the cutting length as shown in Figure 3.2 The conveniences added to the new system improved overall efficiency in the lengthy winding process.

The number of turns was counted with a counter whose shaft spins together with the lathe spindle (located at the end of the spindle), which allowed an exact turn counting. A step type counter triggered by a cam on the lathe spindle was also employed for mutual checking.

The Stycast epoxy was mixed with 4.5 % of Catalyst 11 by weight and poured into the epoxy pot. During the winding process, the pot was cleaned and refilled with fresh epoxy every 5-6 hours. While impregnating paper in the epoxy pot, the pot was warmed to 35 °C using a heater in order to reduce the epoxy viscosity.

A test coil was wound before the actual winding, to test the winding devices and to develop the winding technique. After practicing winding and unwinding, a test

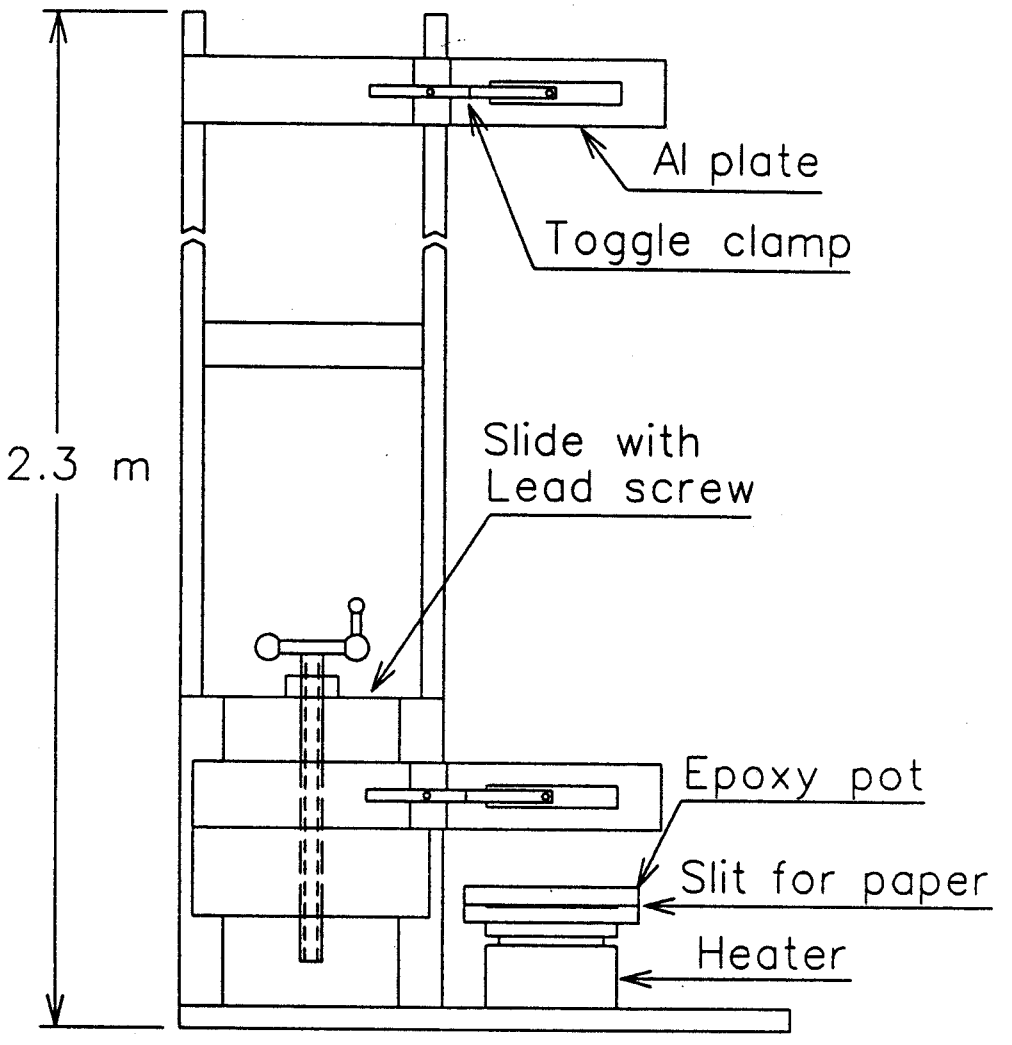

Figure 3.2: The paper cutting apparatus employing a slide with a lead screw. Two aluminum plates set the paper length, and a razor blaze was used to cut the paper. The heater and epoxy pot are also sketched.

coil 28 cm in diameter and 4 layers was finally wet wound and cured. The thickness of epoxy paper between each layer was measured, and the overall thickness of the 8 T coil with 48 layers was accurately estimated.

The progress of the actual winding strongly depends on the preparations made and unexpected problems. For instance, a day was spent to replace the tensioner V belts after they were contaminated with oil from the banding wires. As the coils are potted, it is important to keep the winding period as short as possible, to avoid changes in epoxy characteristics prior to the hardening cycle. The first coil set, involving the small and large coils in the same side of the median plane, is shown in Figure 3.3. The small coil already has its banding in place, and the large coil is being wound.

The coil was cured in a large bakery oven. It took about 20 hours to completely cure the whole coil body due to its mass (peak temperature: 140 °C). The coil temperature was monitored with a thermometer attached on the banding.

The winding took about a month for each coil set with two graduate students working for an average of 10 hours with support from the machine shop. Detailed analysis of workdays for the 8 T coil winding is given in Table 3.2.

III Test of coils in the liquid helium dewar

The coils were tested before being installed in their permanent cryostat in order to ensure basic coil performance before undertaking the many procedures involved in assembly of the cryostat. For this test, the coils with their banding and their welded banding (calm shell structure), were welded onto the midplane structure described in section 2.II.D. The leads were connected, and level gages installed. The coil package was then mounted in a small cylindrical LHe container to reduce the quantity of LHe required for a test, and the whole assembly installed in a large commercial

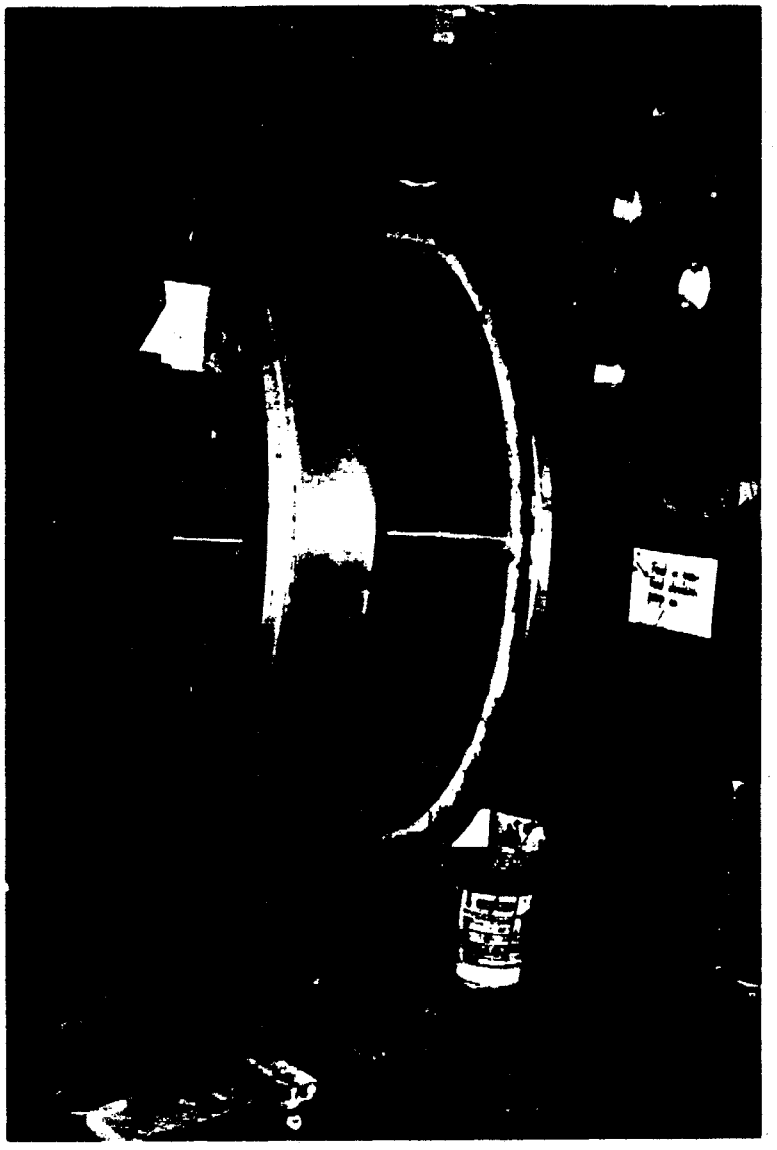

Figure 3.3: The first coil set under winding. The small coil already has its banding in place, and the large coil is being wound.

dewar (Figure 3.4). A relatively long current lead (4 meters) was needed to make a connection from the coil to the existing 500 A commercial current leads at the dewar top. The connection leads were made of four parallel conductors, obtained from spare superconductors for the K500 cyclotron.

In the first test run, the large coils quenched at 250 A. The quench occurred at a LHe level of 75% of the entire coil height. At this level the current leads going to the upper coil were not directly cooled by the liquid helium. One probable explanation of this quench is that the normal zone at the joint propagated into the coil. The heat generated on the joint is roughly estimated as 10^{-4} W at 200 A, which is usually negligible under good cooling conditions. However, this normal region can propagate into the coil when the liquid helium level is below the joint and the leads into the coil. The next test was done with the helium container completely filled. The large coil was operated at 350 A without a quench. A higher current was not tried to avoid the strong magnetic forces induced on adjacent iron structures in the test area. The hoop stress on the large coil at 350 A corresponds to the stress level at a 6 tesla excitation of the magnet with the iron yoke in place. The current was increased at the same rate as in the first test to see if the eddy current heating was the cause of the quenching in the first run, but this turned out not to be the cause.

The small coils were operated at a current of 430 A. To reach a higher current than in the big coil test without jeopardizing the current leads, the dewar pressure was raised to 3 psig from 1 psig for a short time allowing more gas flow through the current leads so as to maintain 150 mV voltage drop in the leads.

This test showed coil performance of at least 70 % of the design expectation, and since the adjacent iron structures made higher current testing hazardous, the testing was terminated and magnet assembly work was begun.

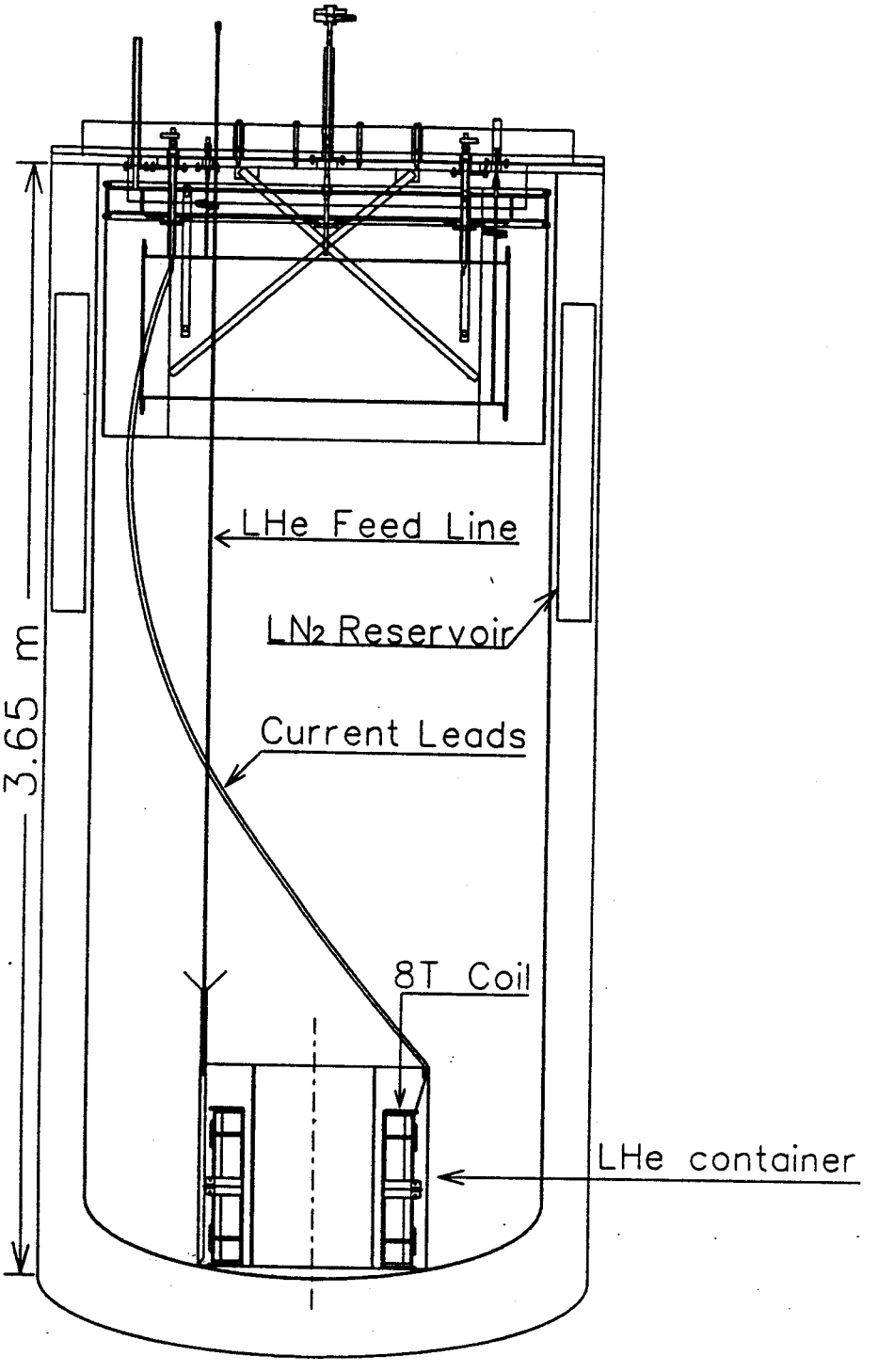

Figure 3.4: The schematic view of open dewar with 8 T coil package inside. The long current leads connecting the commercial 500 amp current leads to the 8 T coils, and the LHe feed line are shown.

IV Vacuum system

Superconducting cyclotron magnets usually have two separate vacuum chambers: a cryostat vacuum chamber for the thermal insulation of the liquid helium vessel, and a beam vacuum chamber for experiments. Vacuum requirements are somewhat different for the two chambers. Air leaks should be eliminated for the beam chamber, especially for the acceleration of heavy ions, but they are more tolerable for the cryostat vacuum because of strong cryopumping by the 4 K vessel. For the cryostat vacuum, however, a helium leak from the helium vessel can cause serious problems. After the magnet is fully assembled, it is very difficult to repair a helium leak, and even with a small leak, the heat load to 4 K increases dramatically; for the beam transport magnets in the MSU/NSCL with a helium leak, the heat load was doubled at 2×10^{-5} torr [Lau]. It was, however, not easy to check for leaks on the helium vessel because of difficulties in achieving a good vacuum due to the large impedance from the small diameter tube; 120 cm long tube with 1.5 cm O.D. designed for the helium gas return was the only pumping line available. Due to the limited conductance of the line, the pumping speed was not enough to make a good vacuum ($< 10^{-5}$) to operate the leak checker at a high sensitivity. The vacuum achieved and calculated considering the reduced pumping speed was at best about 2×10^{-3} torr with a 140 l/sec turbo pump. The RGA (Residual Gas Analyzer) in a bad vacuum mode and methanol were mainly used for leak detection. The coil tank was then cold shocked by filling with liquid nitrogen to reveal latent cracks in the welded regions due to the thermal shrinkage. The leak checking was resumed after the cold shock, and the vacuum reached the same level, which indicated that no leaks were developed by thermal shock.

The beam chamber is a vacuum space surrounded by the yoke and pole tips. The limited conductance is again the dominating factor in determining the vacuum level.

With a 7.6 cm wide and 50 cm long pumping line (rf hole in the magnet), the vacuum will be in the range of 10^{-5} torr with 300 l/s pumping speed for air at STP, which is obtained from the conservation law, $S_1P_1 = S_2P_2$, where S is the pumping speed, and P is the vacuum pressure; P at the pump side is assumed to be in the 10^{-7} range, and a constant virtual leak is assumed. But when the ion source is in operation at the rate of 1 atm cc/sec, the vacuum will deteriorate to a 10^{-4} torr range. To improve the vacuum, there needs to be more pumps added.

V Cryogenic system and radiation shields

To operate the 8 T superconducting magnet at 4.4 K, liquid helium is continuously supplied from the 500 liter dewar connected to the CTI 1400 refrigerator. The helium vessel usually operates at 1.1–1.4 atmosphere, which is determined by the helium gas return line pressure. The warm helium gas effusing from the current leads returns to the compressor operating at 1–2 psi inlet pressure, and the cold gas ($\leq$10 K) coming directly from the vessel returns to the heat exchanger of the refrigerator at 3–6 psi to increase the liquid production efficiency. Liquid nitrogen is also provided to the magnet to keep the radiation shields at 80 K. For the supply and return of these cryogens, a distribution box with the bayonet connections is located at the top of the magnet so that a U tube or flexible lines can transfer cryogens between the magnet and the refrigerator or the dewar.

The radiation shields which surround the helium vessel have to endure the forces induced during fast magnetic flux changes such as a quench. The resulting force may be strong enough to collapse the shields. This accident has actually happened to the K500 [Mar81] arousing caution in shield designing. While the induced force on the inner shield is directed radially outward, the outer shield takes an inward radial

pressure because of the B_z reversal across the coil. From experience of the K500 shield collapsing, the outer shield seems to be more easily subjected to the rupture, although the magnetic pressure is much higher on the inner shield.

The radial pressure on the outer shield of the 8 T magnet during a quench at 400 A is estimated with the equation below;

$$P_L = J_\theta B_z t = \sigma E_\theta B_z t, \tag{3.1}$$

where σ is the conductivity of the copper at 80 K ($\sigma \simeq 1/(2\times10^{-7}\ \Omega\text{cm})$), t is the shield thickness, and E_θ is the electric field on the shield induced at a quench ($E_\theta = \lambda A_\theta$, where λ is from $I(t) = I(0)e^{-\lambda t}$, and A_θ is the magnetic vector potential; $\lambda \simeq 0.3\ \text{sec}^{-1}$ calculated with QUENCH, $A_\theta \simeq 0.6$ T·m calculated with POISSON for a quench at 8 tesla). The pressure is a function of time, and the highest pressure appears shortly after the quench initiation as the flux changes speed up. The maximum pressure on the outer shield is calculated to be about 3 psi. Much higher pressure is induced on the inner shield due to the high B_z; $B_z \sim 6$ tesla on the inner shield compared to ~ 0.2 tesla on the outer shield. The calculated pressure on the inner shield is as high as 110 psi.

The collapsing pressure of the perfectly cylindrical shell is estimated by the formula in reference [Ava87];

$$W_c = KY\left(\frac{t}{D}\right)^3, \tag{3.2}$$

where Y is the elastic modulus of the material, D is the shield diameter, and K is the numerical coefficient related to the shell dimensions, which is graphed in [Ava87]. The estimated collapsing pressure of the outer shield using Eq.3.2 is about 10 psi ($K \sim 90$, D= 75.2 cm), and 20 psi for the inner shield. These estimations do not include the effects of the edge support and of stronger material properties at 80 K. Although the calculated magnetic pressure on the inner shield is higher than the collapsing pressure

during a quench at 8 tesla, there is no evidence of the shield damage after a series of quenches for the 8 T magnet; the measured heat leak was not affected by the quench events, although it is not an absolute indication of no shield damage. (If strain gages were installed on the shields, magnetic pressure could be measured during a quench.)

Chapter 4

Measurements of 8 T magnet properties

I Coil centering

The superconducting coils need to be centered with respect to the pole tips and the yoke to avoid large magnetic off-centering forces and unwanted field harmonics. While assembling the magnet, the coils were roughly centered. Fine adjustment of coil centering was then performed in the process of energizing the coils after the magnet was fully assembled. As the coils are energized, force imbalances measured on the strain bolts installed on all nine links were corrected by shifting the coils.

In section 2.II.B, the spring constants of links and of magnetic off-centering forces were independently estimated. In a magnet system with all links attached, if assuming that there is no interaction between horizontal and vertical links and that interactions with other attachments to the coils such as current leads are insignificant, the spring constants of both link assembly and off-centering force can be measured at the same time using force equilibrium equations in a disturbed link system; i.e. by displacing the links, and by measuring the incremental loads on all the links. A diagram of link systems in this analysis is illustrated in Figure 4.1.

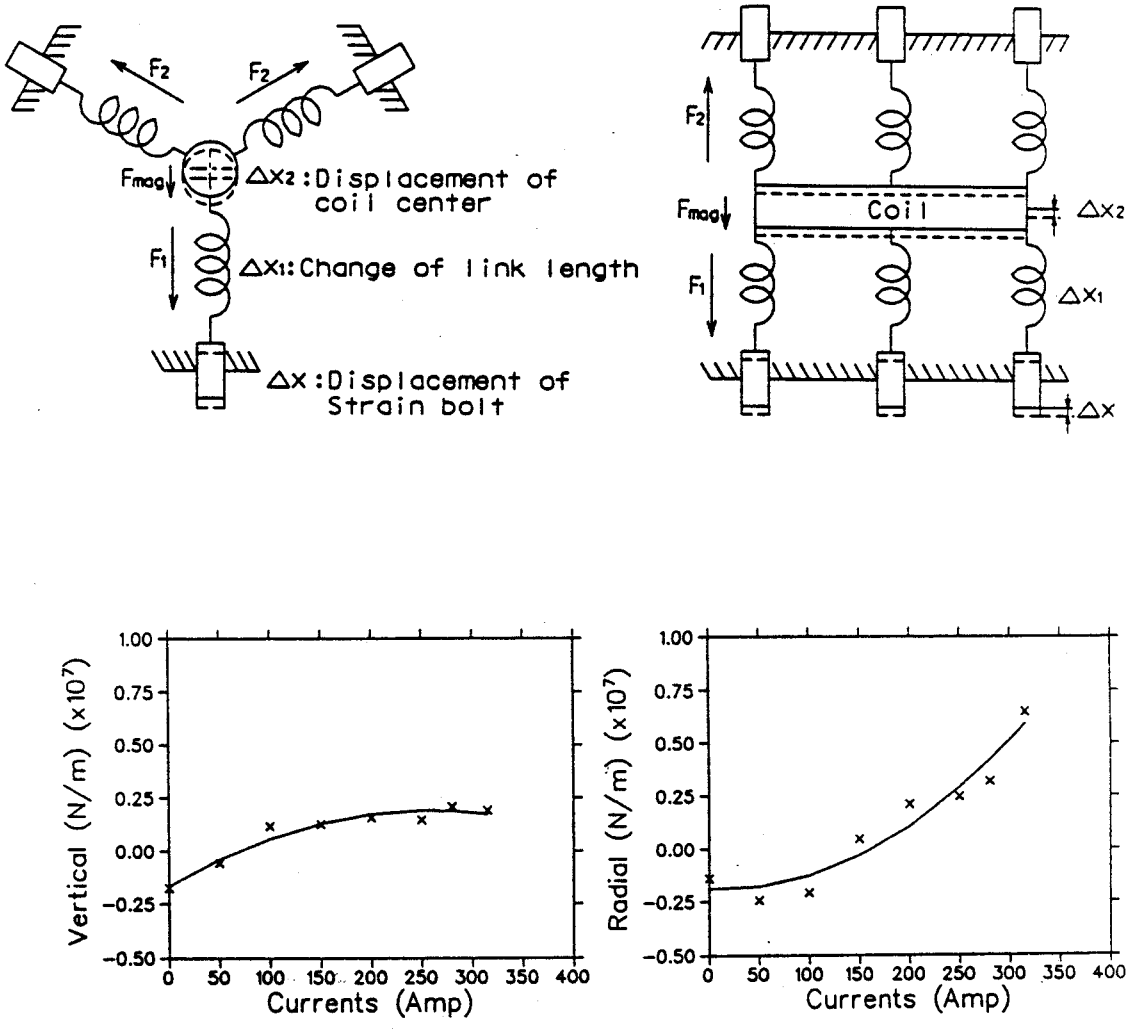

Figure 4.1: Link systems are idealized to obtain analytic expressions for measurements of spring constants. The spring constants of the magnetic off-centering forces were measured as a function of current, and are shown in the bottom graphs.

The equilibrium equations for the vertical links are given below;

$$\Delta X_1 + \Delta X_2 = \Delta X, \qquad F_{mag} + F_1 = F_2, \tag{4.1}$$

where ΔX is the displacement made equally on the three top or bottom links, ΔX_1 is the length change of the links, and ΔX_2 is the displacement of the coil median plane. The forces, F_1, F_2, and F_{mag} can be expressed by Hooke's law;

$$F_1 = k_{vertical}\Delta X_1, \qquad F_2 = k_{vertical}\Delta X_2, \qquad F_{mag} = k_{mag}\Delta X_2, \tag{4.2}$$

where $k_{vertical}$ is the spring constant of the vertical links, and k_{vmag} is the spring constant of the vertical magnetic off-centering force. After doing some algebra, the spring constants of the link and the off-centering force are written in terms of measured quantities:

$$k_{vertical} = \frac{F_2}{\Delta X}(1 + \frac{F_1}{F_2}) \tag{4.3}$$

$$k_{vmag} = \frac{F_2 - F_1}{\Delta X}(1 + \frac{F_1}{F_2}) \tag{4.4}$$

For the horizontal links, the spring constants are given by similar equations as shown below. The displacement in this case is made on only one link:

$$k_{horizontal} = \frac{2F_2}{\Delta X}(1 + \frac{F_1}{2F_2}) \tag{4.5}$$

$$k_{hmag} = \frac{F_2 - F_1}{\Delta X}(1 + \frac{F_1}{2F_2}) \tag{4.6}$$

In this analysis, the deformation effect of the bobbin and midplane ring is not included, which would result in smaller spring constants.

The spring constants of the link assembly obtained in section 2.II.B are compared to measurements made in the magnet system using Eq.4.3 & 5, and shown in Table 4.1. Another measurement was also performed by making equal displacements for all

Table 4.1: Comparisons of link spring constants calculated or measured using different methods

Measurements	Vertical (N/m)	Horizontal (N/m)
From section 2.II.B	1.6×10^7	1.4×10^7
Eq.4.3 & 5	1.0×10^7	1.1×10^7
Equal displacements	0.9×10^7	1.3×10^7

horizontal or vertical links as described in reference [Mil78] to eliminate the effects of other attachments to the coils such as cryogen lines or current leads, and the results are given in the last row of Table 4.1.

The spring constants of the magnetic off-centering forces were extracted using Eq.4.4 & 6, and displayed as a function of current in the lower part of Figure 4.1. (The restoring force at 0 A presumably implies the reaction of the entire system to the displacements because of the attachments to the coil which are ignored in deriving Eqs.4.3–6.) The spring constant of the vertical off-centering force calculated with POISSON (1.1×10^7 N/m, at 400 A, section 2.II.B) is larger than the measurements. For the radial off-centering, the spring constant of 1.5×10^7 N/m estimated by a dipole model at 400 A in section 2.II.B is also larger than the measurements.

II Accident during initial magnet operations

After the 8 T magnet was cooled down to 4 K during the initial operations, the magnet test was performed without a complete analysis of the test scheme. The large and small coils were in a series connection, utilizing only one of the two power supplies (Dynapower Corp. 20V/500 A). This scheme originated from the idea that by ramping both coils at the same rate, the coils could be tested without being affected by heat generated from relative sliding motion between small and large coils.

However, this connection led to a problem due to not considering the quench voltage. When only one of the small and large coil pairs quenches and the other stays in the superconducting state, for instance a large voltage is induced at the connection joint between the two coil pairs, where two terminals from each current leads for the two coil pairs make the joint (and the other two terminals are connected to the power supply). Normally, the maximum voltage on the current leads is limited by the power supply (20 V max.) when the two coil pairs are individually excited; i.e. the current leads are not designed against high voltages. The program QUENCH estimates that the voltage at the joint is about 500 V after a second ($\approx$ 100 kW at 200 A). (During a quench, a high voltage, which is estimated to be as high as 2.5 kV, can appear at the median plane connections between the image coil pairs. However, the insulation is designed for that voltage, using Teflon sleeves of 0.15 mm thick and Kapton tapes (3M) of 0.07 mm thick.)

Due to this large energy discharge, many instrument wires sharing the outgoing tube with the current leads (see Figure 2.16) were damaged, including all strain gage leads, and the large coil showed a short to ground. The short location, roughly verified by TDR (time domain reflectometry) was near the cold end of current leads where the current lead wires are bare and the insulation for the instrument leads is 0.03 mm thick Formvar only. Fortunately, however, two instruments important in basic magnet operation, a helium level sensor and a temperature sensor survived, and the short in the large coil appeared to be weak, the short resistance increasing after another magnet operation.

At present, the magnet itself is operational without much influence from the accident, but the loss of major instrumentation such as lead voltage taps, strain gages, spare temperature and helium level sensors, was substantial.

4.3 Strain gages for coil stress measurements

To compare actual stress with design expectations, coil stress measurements using strain gages bonded on the coils were tried. Since stress is a tensor quantity, it can not be measured directly except for special cases. With Hooke's equation, stress can be determined from strain measurements and material properties. A single gage configuration was mainly used to measure the principal coil strain, because its direction is clearly along the circumference of the coil. Strain gages with a rosette geometry (a group of three gages arranged in a 0°, 45°, 90° pattern) were also attached on the upper large coil, which can determine the complete stress distributions on the measurement plane [Ger90].

The strain gages can be subject to parasitic effects coming from installation, magnetic fields, and lead wires among other things [Han92]. A connection known as the three wire method (top part of Figure 4.2) was employed to avoid some of the lead problems by cancelling the false signal. The magnetic field effect was also taken into account by using a strain gage attached to a floating plate. The output due to the magnetic field can be measured by this gage.

To ensure the operation of strain gages at least at 80 K, an actual test was performed with the same apparatus used for tensile strength measurements of support links schematically shown in the middle of Figure 4.2. Two different types of strain gages purchased from Measurements Group Inc. were tested: CEA-06-125UR-120(Ω), and SK-06-125RA-350(Ω), where the operating temperature of the 'SK' type extends to 80 K, and possibly to 4 K, while the CEA type is mainly for room temperature use. The test results comparing the outputs of the strain bolt and gage are shown in the lower part of Figure 4.2. The strain bolt at room temperature is believed to give more reliable measurement. The comparison in the figure shows that the strain

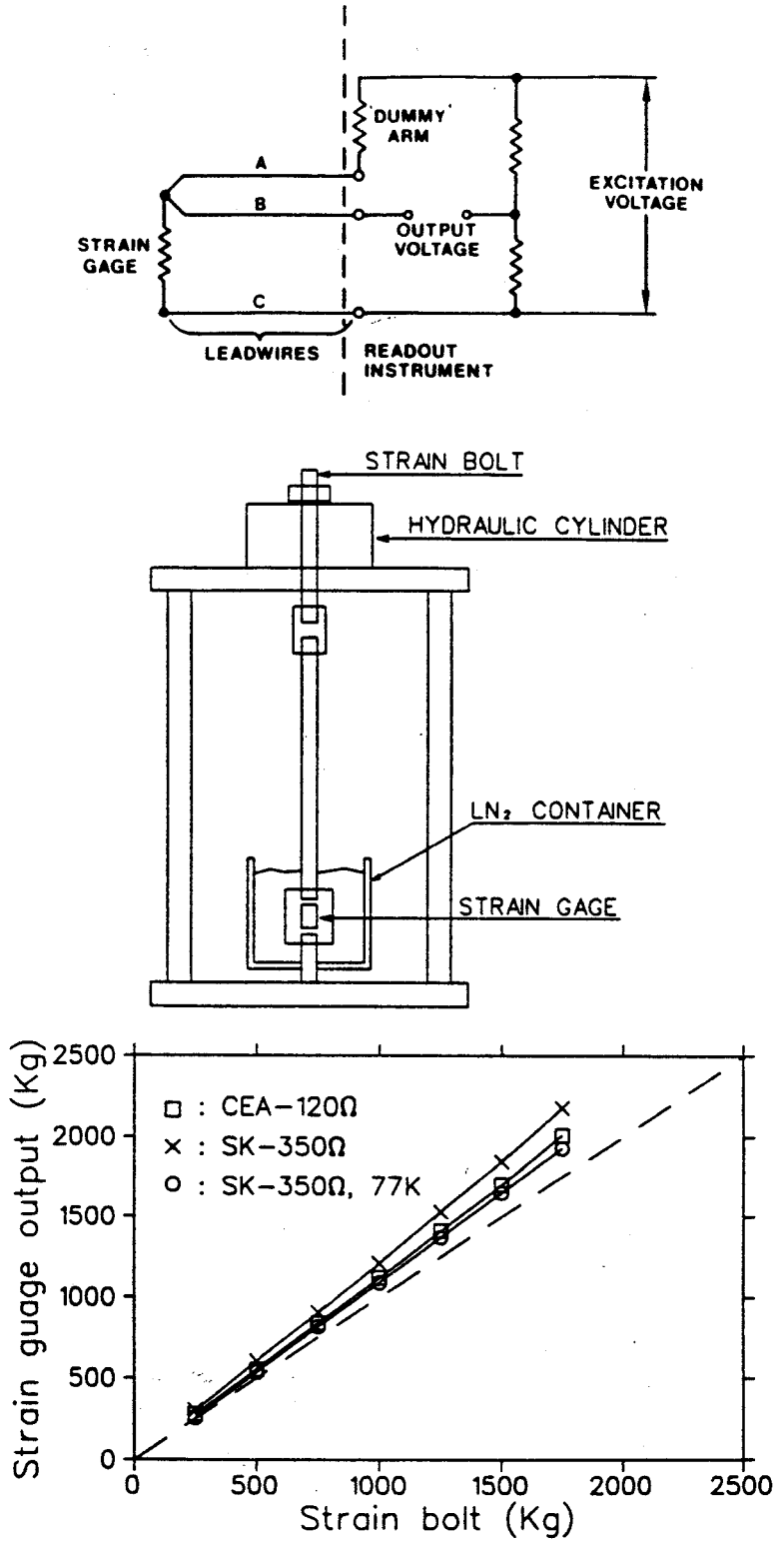

Figure 4.2: Top: a three wire method of strain gage connection to cancel out the false output induced in leads. Middle: experimental set-up to compare the readouts from strain bolt and gage at 300 K and 80 K. Bottom: the output comparisons of strain bolt and gage. The reading from the gage is higher than that of strain bolt, but the reason is uncertain.

gage outputs seem to be consistently higher than the strain bolt output. At 80 K, the output of the CEA type was very unstable compared to that of the SK type as expected.

When the strain gage is subjected to temperature variations, its resistance changes appear as 'apparent strain'. The resulting thermal output depends on the material to which the gage is attached. The stainless steel used in this test shrinks more than the 1018 steel for which Measurement Group Inc. provides the thermal output data ($(L_{293}\text{-}L_4)/L_{293}$ (%) is 0.19 for steel, and 0.31 for 304 stainless steel). After the correction of thermal shrinkage was made, the measurement agreed with the company's data within 5%, which showed the possibility of measuring the thermal stress in the coil.

The strain gages were attached to the clam shell structure of the 8 T coils, which surrounds the banding, because other places inside the coil are not easily accessible for gage installation. The stress on the shell structure can be used to deduce the coil stress distributions using STANSOL calculations; by matching the measurements and calculations on the shell, the coil stress distributions can be then inferred.

4.4 Coil stress measurements of the 8 T magnet

When the coil was cooled down and energized, the strain gages were used to measure the coil stress. Thermal outputs from different strain gages were not consistent, and they were drifting. The average strain (of three gages) was approximately 2000 $\mu\epsilon$ ($\pm$200), which is approximately the strain caused by the thermal shrinkage in a free body made of stainless steel (1800 $\mu\epsilon$). Since the coil shrinks away from the banding and clam shell structure, it is understandable.

The strain caused by electromagnetic forces was then measured. The first mea-

surement was made on the clam shell of the large coil. The strain reading was almost a constant until the current was ramped to 200 A. When the current was increased to 300 A, the hoop stress on the clam shell increased roughly by 1200 psi. This stress increase is much lower than 5100 psi from the STANSOL calculation in which a complete contact with the banding is assumed. If the contact is loose, the clam shell would be subjected to much lower pressure, as the measurement implies. The lower hoop stress could be due to the loose fit, but the possibility of the false output on the strain gage could not be excluded.

Since the lead wires of all strain gages were damaged during the accident described in section 4.II, coil stress data beyond that described here could not be obtained. In general, measurement of coil stresses at 4 K is not an easy task.

4.5 Magnet quench study

Quenches of the 8 T magnet were studied to understand the quench causes. Variations of physical parameters during a quench, such as the coil current decay and the coil temperature increase, were measured and compared with computations.

When the magnet quenches, it is difficult to actually measure the physical parameters such as the hot spot temperature and the IR drop in the coil because of the high voltage induced on the instrument lead wires and on the voltage taps, so that strong insulation is required for those wires to carry out measurements. The current is the only physical quantity, which can be easily measured. The decays of the coil currents were recorded with current transformers (HOLEC, 500 A), and compared with the QUENCH calculations for the large coil in Figure 4.3. A quench at low currents ($\simeq$200 A for both small and large coils) was induced by the depletion of

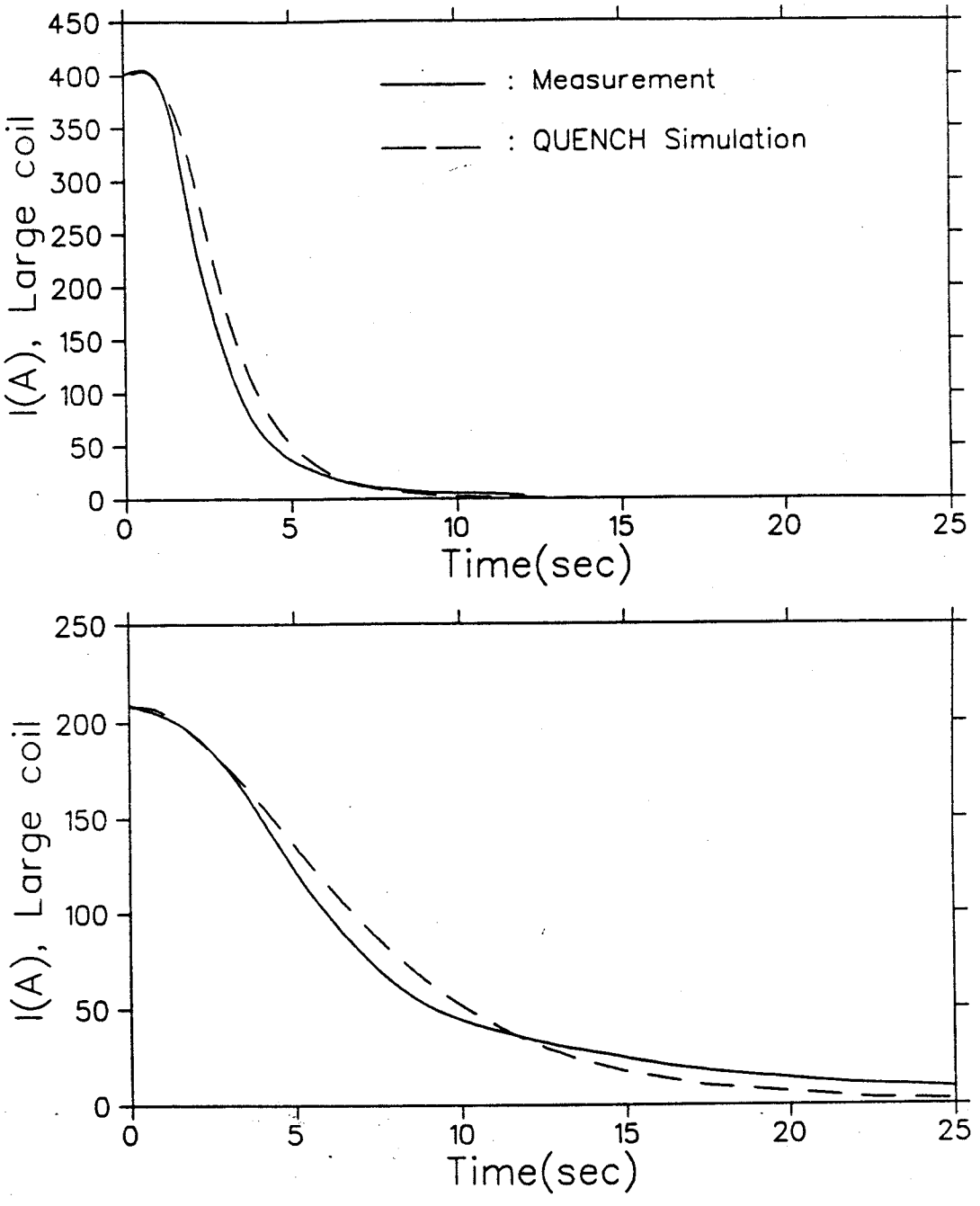

Figure 4.3: Current decays of magnet quenches were measured and compared with the QUENCH calculations (transverse velocity = 0.075 longitudinal velocity). Measurements were made for a large coil pair only in this case.

the liquid helium, and a quench around 400 A (small coil current: 300 A) occurred during the current ramping. The comparison shows that the actual current decay is faster during the first few seconds after a quench than the QUENCH simulation, and slower at low currents. This trend has also been observed in other magnet quench studies [Wil83]. The discrepancy between the simulation and calculation may come from the assumptions made in the calculation such as the quench origin (corner of the innermost layer), and the transverse velocity of quench propagation, as well as from uncertain material properties.

The coil temperature increase after a quench was measured with Allen-Bradley carbon resistors (500 Ω at 300 K) attached to the clam shell structure, from which the stored energy was estimated. This measurement method is however inaccurate because: 1) the resistor was not well calibrated, and 2) the equilibrium coil temperature differs from the resistor reading because the resistor is being continuously cooled by cold helium gas whose enthalpy is much higher than the enthalpy of the coil materials at low temperature. For instance, when the coils quench at I_{small}= 330 A and I_{large}= 400 A, the stored energy obtained with this method was only 60% of the energy calculated from magnet inductances (see the following section).

In the initial magnet operations, the magnet quenched at relatively low currents, and the currents at quenches varied (see Figure 4.4), which is typical for a quench induced by wire motion. However, it soon became apparent that the currents could be increased by following the particular current ramping paths; the large coil should be energized first up to 420 A before the small coil is energized over 300 A, which can be noticed from the current ramping procedures described in the table in Figure 4.4.

To reveal the cause of these quenches, the LHe bath temperature was lowered from 4.4 K to 4.2 K by venting the boiled-off helium gas to the air. If the quench occurs due to the wire motion, the current at a quench should be independent of

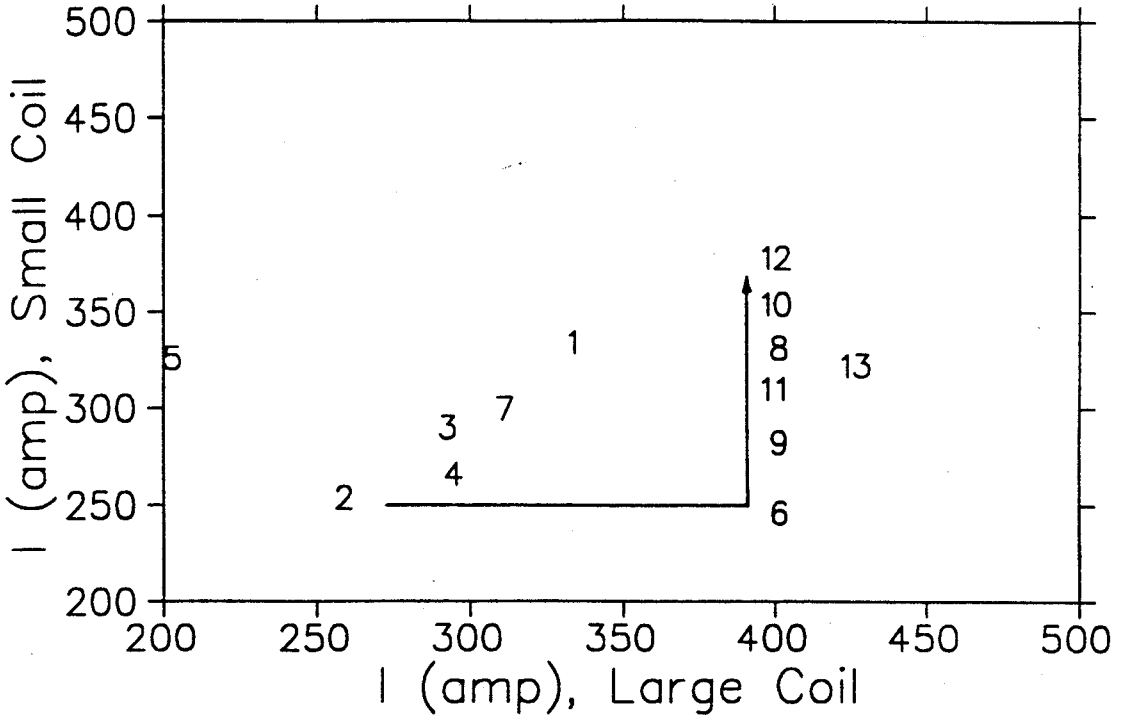

Quench #	Current ramping procedure before a quench
1-3	same rate for both coils (serially connected)
4	similar rate for both coils, large coil to 293 A and small coil to 270 A
5	1)both coils to 208 A, 2)small coil to 323 A
6	1)large coils to 400 A, 2)small coil to 250 A
7	1)both coils to 250 A, 2)small coil to 300 A, 3)large coil to 310 A
8	1)both coils to 250 A, 2)large coil to 400 A, 3)small coil to 330 A
9	1)both coils to 240 A, 2)large coil to 400 A, 3)small coil to 285 A
10	1)both coils to 240 A, 2)large coil to 400 A, 3)small coil to 352 A
11	1)both coils to 240 A, 2)large coil to 400 A, 3)small coil to 310 A
12	4.2 K, 1)both coils to 240 A, 2)large coil to 400 A, 3)small coil to 375 A
13	1)both coils to 240 A, 2)large coil to 420 A, 3)small coil to 325 A

Figure 4.4: The quench history of the 8 T magnet is displayed as a time sequence. To reach higher currents, it was necessary to follow a particular current ramping path as shown in the figure by an arrow. The magnet operating temperature was 4.4–4.5 K, depending on the LHe supply pressure which was difficult to regulate.

small temperature changes. On the other hand, when a critical current limit causes a quench, the current at a quench should react sensitively to temperature changes. By reducing the LHe bath temperature, the small coil current before a quench increased by 23 A compared to the previous quench points (see quench # 10 and 12 in the table in Figure 4.4). This could be explained as either 1) evidence that the present quench may be caused by the critical current limit, or 2) training that the currents at a quench continue to increase. (This test was performed only once because of the excessive LHe loss for each experiment; over 100 liters.) Another unexpected phenomenon is that the current ramping path influences the quench point, and that the small coil current has never reached 400 A while the large coil can be easily operated over 400 A.

The maximum currents at quench were I_{small}= 370 A, I_{large}= 420 A, and the highest field achieved in the magnet gap was 8.2 T. The current margin (m_i) defined in section 2.I.I is about 26%, since I_{cr} is 560 A at 8.1 tesla on the conductor at 4.4 K.

4.6 Inductances of the magnet

Inductances of a magnet employing steel are a function of iron saturation. As the iron progressively saturates, the magnet inductances approach the coil inductances. While the coil inductance is one of the design considerations, the inductance due to the magnet steel is not a main concern for DC magnets such as cyclotron magnets. High inductances slow down current ramping rates at low magnetic fields ($\leq$ 2.5 tesla), and contribute to the stored energy, which are usually considered to be unfavorable in magnet operation.

Since the 8 T magnet has the small and large coils, they are inductively coupled as below.

$$L_1\frac{dI_1}{dt} + M\frac{dI_2}{dt} = V_1 \quad L_2\frac{dI_2}{dt} + M\frac{dI_1}{dt} = V_2, \tag{4.7}$$

Table 4.2: Comparisons of measured magnet inductances to calculations with POISSON after iron saturation.

	L_1	L_2	M	Stored Energy
POISSON	22.0	6.68	5.03	3.1 MJ
Measurement	20.	4.4	5.9	

where, L_1 and L_2 are the inductances of each coil, M is the mutual inductance, and V_1, V_2 are the driving voltages. The L_1 and L_2 of each coil were measured by removing the mutual inductance term using two different methods: 1) ramping each coil individually with the other coil circuit opened, and 2) ramping only one coil with the other coil current regulated by power supply (results obtained from the two methods agreed within 20 % before iron saturation, and within 5 % after saturation). Unequal currents in the two coils were then converted to an equivalent current using $I_{eq} \simeq (I_{small}+2I_{large})/3$, which was obtained from the relative contributions of each coil to the total field [Hum89]. The mutual inductance was then measured by ramping both coils at similar speeds.

If the polarity of the power supply system were reversible, the inductances could be measured by using different combinations of the polarity in each coil, as demonstrated in inductance measurements of the K1200 magnet [Hum89]. The inductances of the 8 T magnet measured as a function of current are shown in Figure 4.5. When the pole tips are saturated at high fields, the measured inductances are compared to calculations with POISSON in Table 4.2. The measured mutual inductance is larger than the calculated one ($M^2 \leq L_1 L_2$ is the only condition to be satisfied).

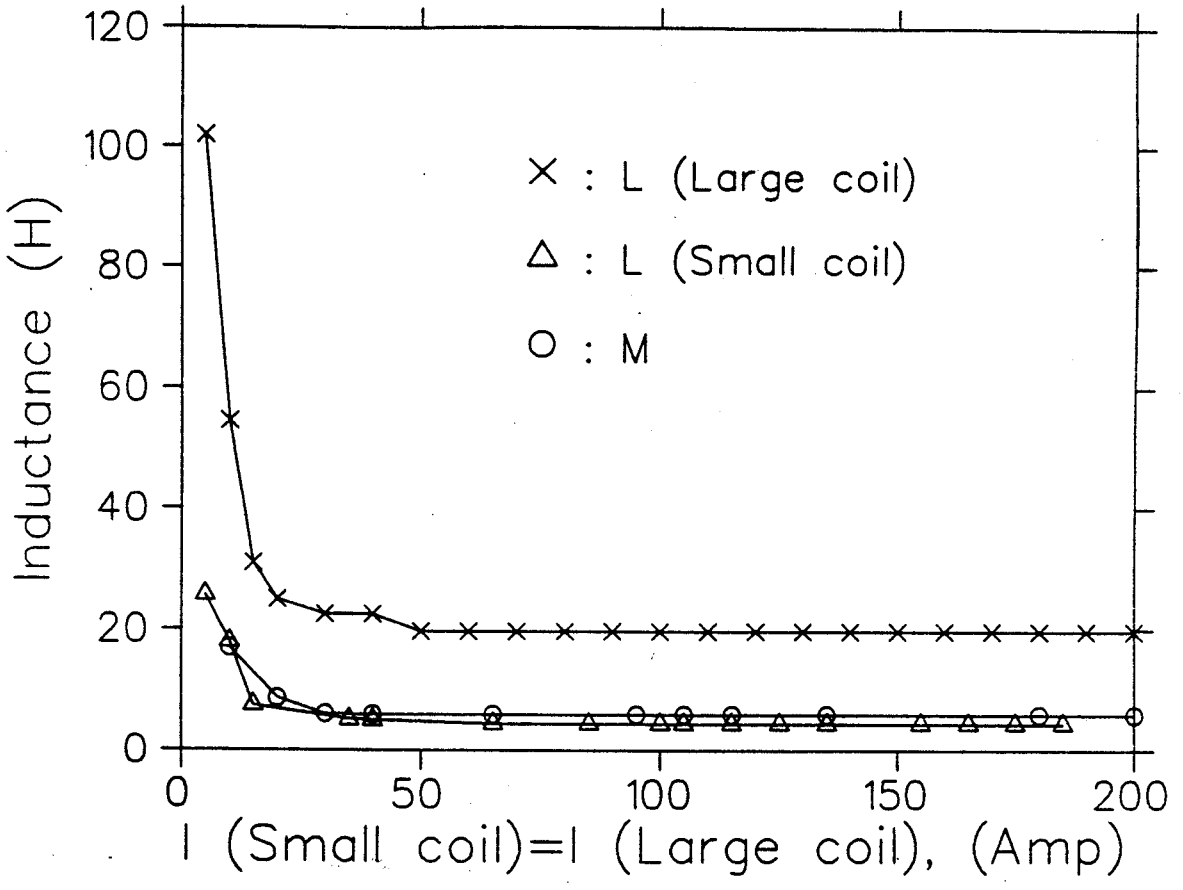

Figure 4.5: The magnet inductances measured as a function of currents. The currents of the two coils are converted to an equivalent current as described in the text. The inductances reach the saturated values around 2.5 tesla.

VII Heat leak in the magnet

The heat leak into the LHe was measured when the magnet was cooled down for the first time, and is displayed as a function of LHe level in Figure 4.6. Calculations, including the contributions of conduction, radiation, and the current leads were also made, and are compared to the measured heat leak in Table 4.3. The conduction contributes only a small portion of the total heat leak. The radiation heat leak was calculated using the experimental heat leak data between 4 K and 80 K surfaces covered with 3M aluminum tapes [Leu85] since superinsulation is not employed in that space.

The measured heat leak is much higher than the calculations in Table 4.3, and average heat leaks differ across the median plane. Two different heat sources may be added when the liquid helium level is over 50 %: 1) LHe loss due to the helium pressure change right after finishing the LHe transfer, and 2) large heat leak through the median plane structure due to the poor thermal insulation, which contributes less when LHe does not make direct contact with the structure.

When the liquid helium transfer is completed with the valve closed, the helium pressure usually decreases depending on the LHe transfer pressure. To reduce the boiling temperature according to the pressure drop, some LHe has to evaporate, carrying the heat away. However, the helium pressure effect was difficult to identify; variations of the LHe transfer pressure were not well correlated with the heat leak near the top of LHe level. (The possibility of thermal short between the helium vessel and the 80 K shield at the vessel top was also considered as a large heat leak source, although it is unlikely from the fact that the heat leak decreases rapidly with a small LHe level drop.)

In room temperature penetration holes, the gap between 300 K and 4.4 K is 0.6 cm

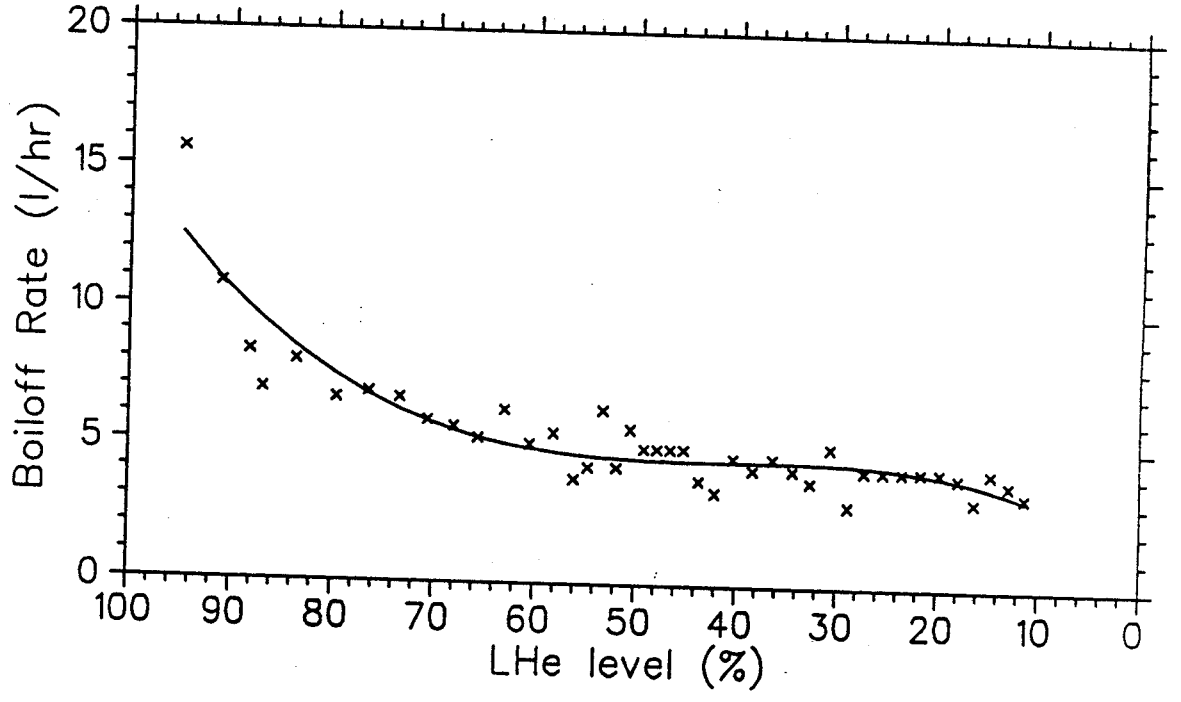

Figure 4.6: The heat leak to 4 K as a function of LHe level. The large heat leak near the vessel top may come from the helium pressure drop after stopping the liquid helium transfer

Table 4.3: Heat leak at 4.4K

	Items	Heat Load at 4.4 K
Estimation	Two current leads	1.4 W
	Radiation	0.04 W
	Conduction on links	0.15 W
	Total	1.6 W
Measurements	LHe level	Average Heat load
Without He leak	<50 %	3.0 W
	>50 %	4.8 W
With He leak	<50 %	4.8 W
	>50 %	11 W

so that only 15 layers of superinsulation were employed. In addition, those penetration holes could not be perfectly insulated because of the difficulties in connecting to the superinsulation in other regions, which could cause a large heat leak. It is believed that a larger overall heat leak than the calculation is due to this large heat load in the median plane structure even when the LHe level is below 50%. A similar heat leak problem has been observed for the K1200 magnet [Lau83].

After operating the magnet for about a week, a helium leak into the insulation vacuum was detected. It was noticed because of an enormous increase in heat leak; LHe loss became more than 100 l/hr after 2-3 hours without pumping the cryostat chamber. With continuous pumping, the helium loss was reduced to 18 l/hr, which barely allowed continuous operation of the magnet with the supply of LHe from the 500 liter dewar with a LHe production rate at 20 l/hr by CTI 1400 refrigerator. When the magnet was warmed to room temperature after the initial tests, suspicious joints of Cajon fittings were re-tightened, and the helium leak has disappeared.

The heat load on the 80 K radiation shields is usually not seriously considered because of the low cost of LN_2. The calculated heat load on the 8 T magnet shields is 3.5 W from radiation (1 W/m^2 with 18 layers of superinsulation [Shu86]), and 1.5

W from conduction. The total heat load of 5.0 W can be easily removed with liquid nitrogen, employing a 0.63 cm O.D. transfer line.

Chapter 5

Field mapping and analysis

Magnetic fields were measured using a Hall probe (F.W.BELL). The probe was installed in a copper tube, and the tube was inserted into a penetration hole at a fixed angle. The Hall probe was later calibrated by a NMR probe (SENTEC D_2O probe #7, range: 30–68 kgauss(kG)) which was located at the center of the magnet's axial hole, where the field is uniform enough to generate sharp resonance signals. Table 5.1 shows the magnetic fields measured by the two probes at the same location. The fields by the Hall probe were fitted to the fields by the NMR probe using second degree polynomial: $B = 0.0713 + 0.9932B_{Hall} + 0.5760\times10^{-3}B^2_{Hall}$, where the B and B_{Hall} are in units of kG. All measured fields by the Hall probe displayed in this section were corrected according to this equation. In the range of 35–64 kG where the NMR calibration was carried out, the error due to the fitting and significant figures in the Hall probe readout is estimated to be 0.05 %. (The NMR probe which can calibrate near 8 tesla was highly required to avoid extrapolation, but was not available during the measurements.)

Because of the symmetry of the twelve penetration tubes and of threefold symmetry of the yoke, there are two angles at which the magnetic fields are different if perfect symmetric fields are assumed. Measurements were made only at one angle since mapping at this stage was intended for a comparison with the calculation rather

Table 5.1: Calibration of the Hall probe by the NMR probe

Hall Probe (kG)	35.27	39.74	43.94	52.83	56.78	60.96	63.29
NMR (kG)	35.820	40.442	44.816	54.138	58.300	62.775	65.235

than for particular uses of magnetic field data.

The 3-d magnetic fields were calculated with the finite element program, TOSCA. The magnet model includes a twelfth of the yoke and all four coils as displayed in Figure 5.1. For three different excitations, magnetic fields were measured and compared to the TOSCA calculations in Figure 5.2. Measured fields in the flat region seem to be lower than the calculated fields by nearly a constant, insensitive to the radius and excitations. To explain this, it was thought that the saturation point of the steel used in the magnet may be lower than the saturation point in the BH table (B_{sat}= 2.14 T) for TOSCA. This is probable since the pole tip and the yoke are made of the 1020 steel while the BH table used in TOSCA may be more adequate for steel with lower carbon content. When the measured fields are subtracted from the calculated fields using $B_{saturation}$=2.14 T, a difference of about 500 gauss is visible as shown in the lower graph of Figure 5.3. When the saturation point of the BH table in the code was reduced by 500 gauss, the agreement appears better for high fields (upper graph in Figure 5.3), but it still seems unsatisfactory for lower fields, especially in the center region. The mesh size effects on TOSCA calculations were not thoroughly examined, but should be smaller than the present differences in the fields. Large differences near the center hole between measurements and TOSCA calculation were not thoroughly understood.

TOSCA fields are Fourier analyzed, and shown in Figure 5.4. The third harmonic component, B_3 which is important as a flutter for sector focusing in isochronous

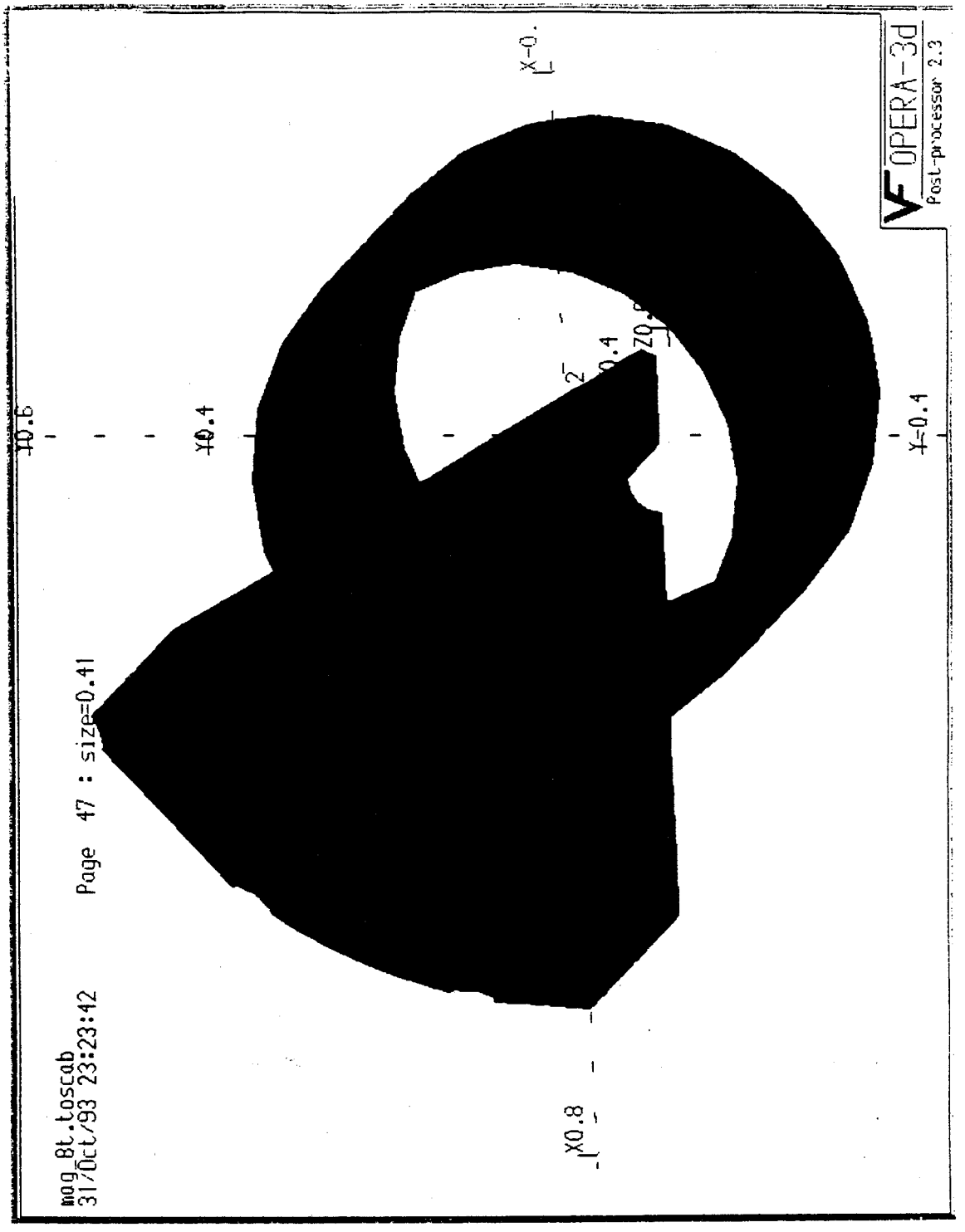

Figure 5.1: A magnet model used for TOSCA. One twelfth of the yoke and four coils are involved in the model. Some details of the magnet such as the rf holes and room temperature penetration holes are also included.

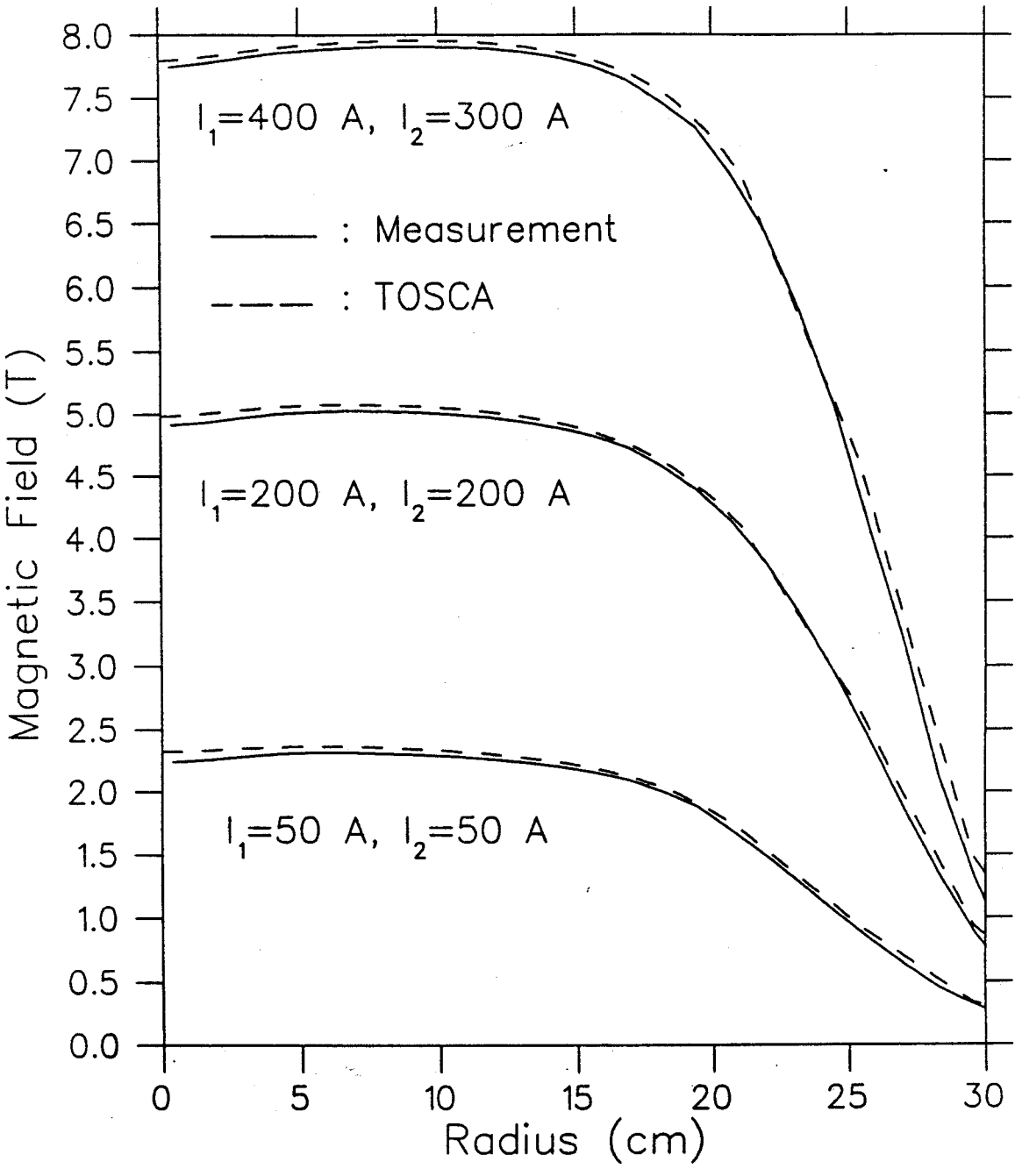

Figure 5.2: For three different excitations, measured magnetic fields are compared to calculations by TOSCA.

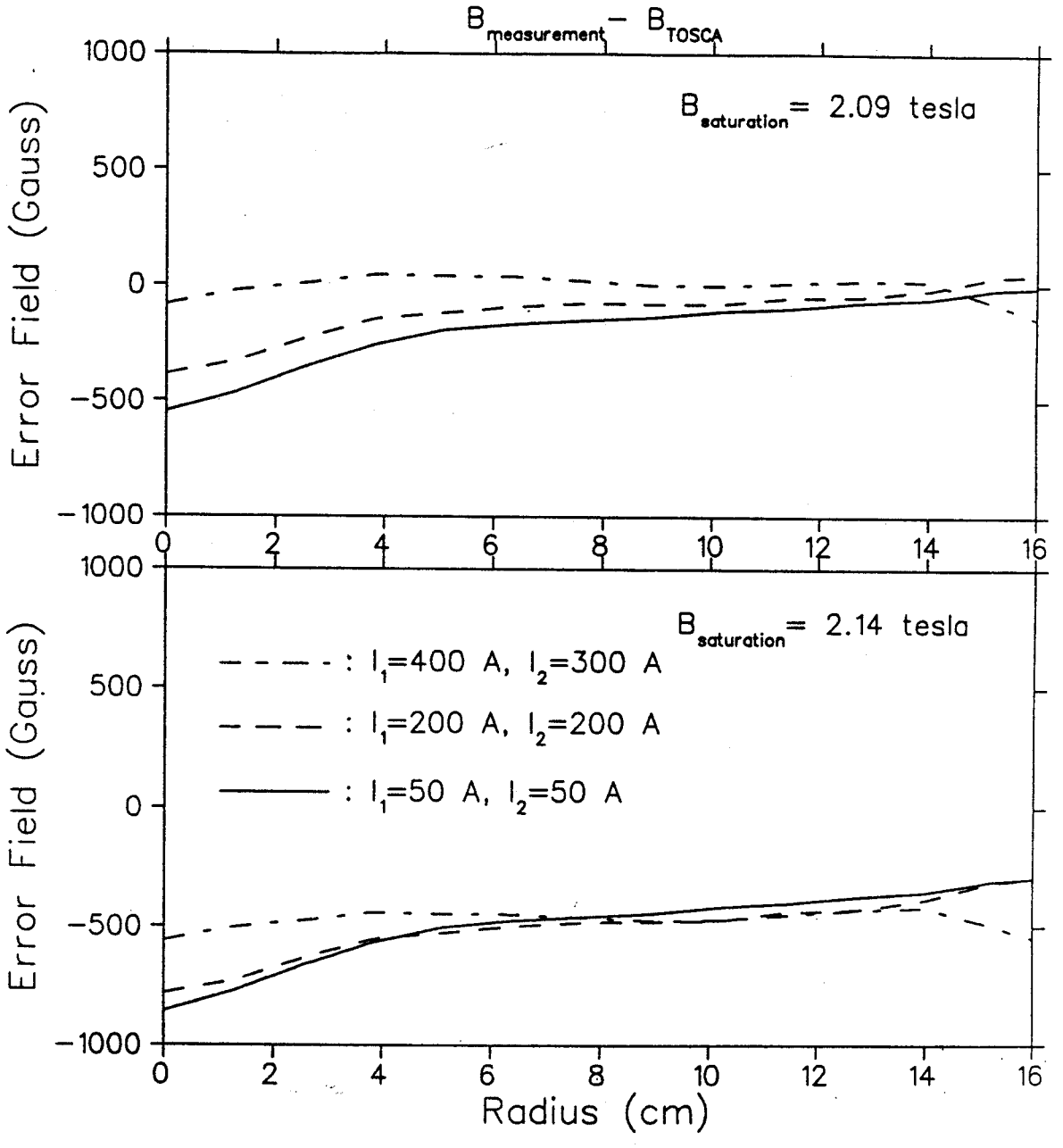

Figure 5.3: Differences between the measurements and calculations are plotted when the iron saturation point is 2.14 T in the lower graph, and 2.09 T in the upper graph.

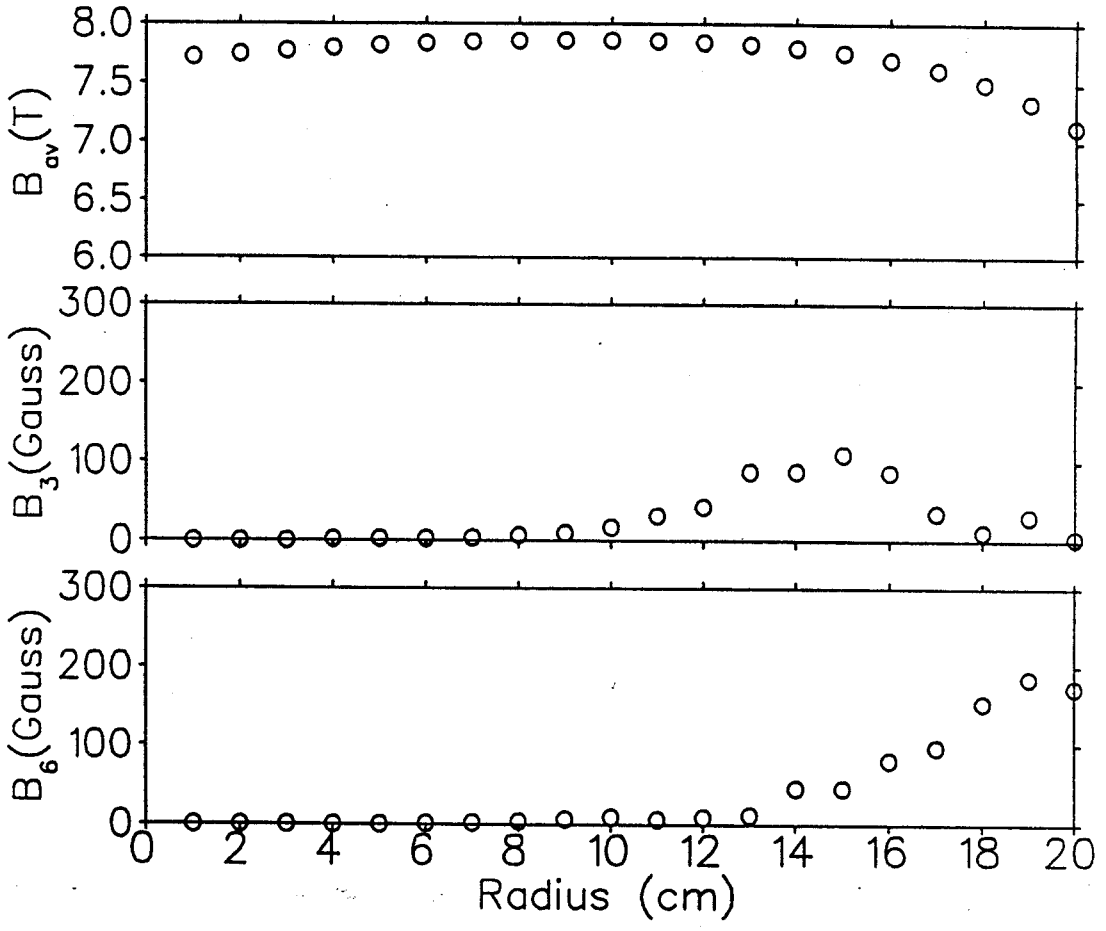

Figure 5.4: A field at I_{large}=400 A, I_{small}=300 A is Fourier analyzed to see the components of higher harmonics in the present magnet configuration.

cyclotrons, is weak. Higher harmonic fields in the present magnet configuration are mainly caused by rf holes and penetration holes included in the model. The pole tips do not have sector structures yet.

Chapter 6

Conclusion

The 8 tesla superconducting magnet was built and tested, mainly to study cyclotron related phenomena. Because of limited experience in constructing superconducting magnets using NbTi superconductor at 4.4 K to produce over 8 tesla on a large scale (with a bore diameter$\geq$ 0.5 m), it was uncertain that this 8 T magnet could be built to operate reliably. Long term operational results are not available yet, but the magnet has proven to be able to produce fields over 8 tesla. In retrospect, among the design options we have studied, the selection of the free coil could be the reason for the successful generation of an 8 tesla field. The free coil has been also studied by other groups [Bob85] [Ant89] for superconducting NMR magnets, which drew similar conclusions.

With the 8 T magnet completed, some utilization was planned. Ion source emittance measurements and a conversion to a cyclotron would be the probable uses of the magnet. These were studied by computations, as described in the appendix, to produce experimental schemes for the source emittance measurement and to explore cyclotron design parameters for a future cyclotron project. In one plan, the conversion project may proceed prior to source emittance experiments since the cyclotron project seems to be more interesting, with the 8 T magnet designed appropriate for an isochronous cyclotron.

The acceleration of heavy ions is less severely restricted by focusing difficulties in a high field isochronous cyclotron. Hence, it would be beneficial to build heavy ion cyclotrons using magnetic fields still higher than 8 tesla. A 10 tesla magnet could be built by employing the present 8 T magnet construction technique, with the addition of a cryogenic system which can reduce the LHe bath temperature to 1.8 K (for instance by reducing the helium pressure to 0.016 atmosphere). However, the coil stress due to the higher magnetic field and current density is much larger for a 10 tesla magnet; a thicker banding with higher preloads and special copper matrix whose yield strength is higher than 20,000 psi at the cost of resistivity would be required to withstand higher coil stress without degrading the critical current. (Also the refrigeration required to go from 4.5 K to 1.8 K is about twice as much). Superconducting magnets for over 10 tesla could be made using Nb_3Sn superconductors, but this would involve a much more difficult coil winding technique.

Compactness in a cyclotron is usually a more appealing feature in commercial applications than in academic research. Conventional commercial cyclotrons designed to produce isotopes, for instance mostly use room temperature magnets in a 1-2 tesla field range [Cyc92]. Uses of high field superconducting magnets for these commercial cyclotrons are often limited because: the overall system is more complex, and the coil construction is more difficult. However, commercial company such as the Oxford Instruments has already constructed a commercial superconducting cyclotron, and maybe more broadly used in the future. Hopefully, experience gained from the construction and the operation of the 8 T magnet and a future cyclotron conversion project will add significant reliability record to future high field superconducting cyclotrons.

The uses of superconducting magnets have been expanding for more than a decade, but rather more slowly than expected because of the complexity in supporting equip-

ments such as cryogenic systems. High T_c superconductor led to much optimism about eliminating the need for liquid helium systems. However, to date progress toward large scale several tesla magnet operating at liquid nitrogen temperature has been minimal.

Appendix A

Plan for the ion source emittance measurement

I Source emittance measurement under rf extraction

A plan was made to measure the radial emittance (r,p_r) of the internal ion source as a function of rf starting time in the center region of the 8 T magnet. The magnet will provide magnetic fields with a flat radial profile in a range of 2–8 tesla. The radial phase space information is important in designing a cyclotron because of the relationship with the orbit centering and extraction efficiency.

Initial conditions for tracking orbits in a cyclotron system are usually provided from measuring the ion source phase space. If ions are extracted from the source by dc electric fields (such as in an ECR source), source emittance can be measured using the two slit system [Tom72]. A cyclotron with an internal source, on the other hand, employs rf electric fields to extract ions. Source emittances for such a cyclotron, however, have not been measured to the author's knowledge using rf extractions, and initial conditions for the orbit codes have been inferred from dc extraction measurements. If the voltage at the moment of ion extraction can be indicated in a narrow range, the measured dc emittance can be used as initial conditions at corresponding

voltages.

A Central region designed for emittance measurement

The design goal of the 8 T magnet's center region for emittance measurement was to spread the beam for differing rf starting times so that the emittance could be compared for different rf ranges selected by slits. As suggested in reference [Kim92c], three slits can roughly separate three coordinates: 1) rf phase, and 2),3) radial emittance (r,p_r).

In a real system, however, one more physical parameter, initial energy, needs to be considered in designing the central region. The initial ion energy was first assumed to be fixed at 250 eV, and then different initial energy effects in orbit trajectories were considered. The initial energy of 250 eV was inferred from dc emittance measurement with a 30 kV extraction voltage [Tom72] using the phase space conservation law. If the momentum transfer from electron to ion is the only mechanism in determining the ion energy, however, the initial energy may be a few eV, which is acquired by collisions with electrons of a few keV emitted from a cold or hot cathode. Actually, ion energy of a few to a few tens of eV has been more frequently assumed in designing the central region of other MSU cyclotrons using an internal source [Blo63][Bai89].

In orbit tracking, ions are generally assumed to start at the source opening, where the plasma is at ground potential. In reality, however, rf electric fields penetrate into the plasma, and the plasma meniscus changes as a function of the rf phase [Ben72]. Fixing the initial location and energy for ions starting from widely different rf phases is thus difficult to be justified.

The central region shown in Figure A.1 provides a two gap acceleration with a flight path of about 90° between two gaps so that the orbits are spread in an orderly fashion in the ground region where the slits are located. Several such orbits are shown

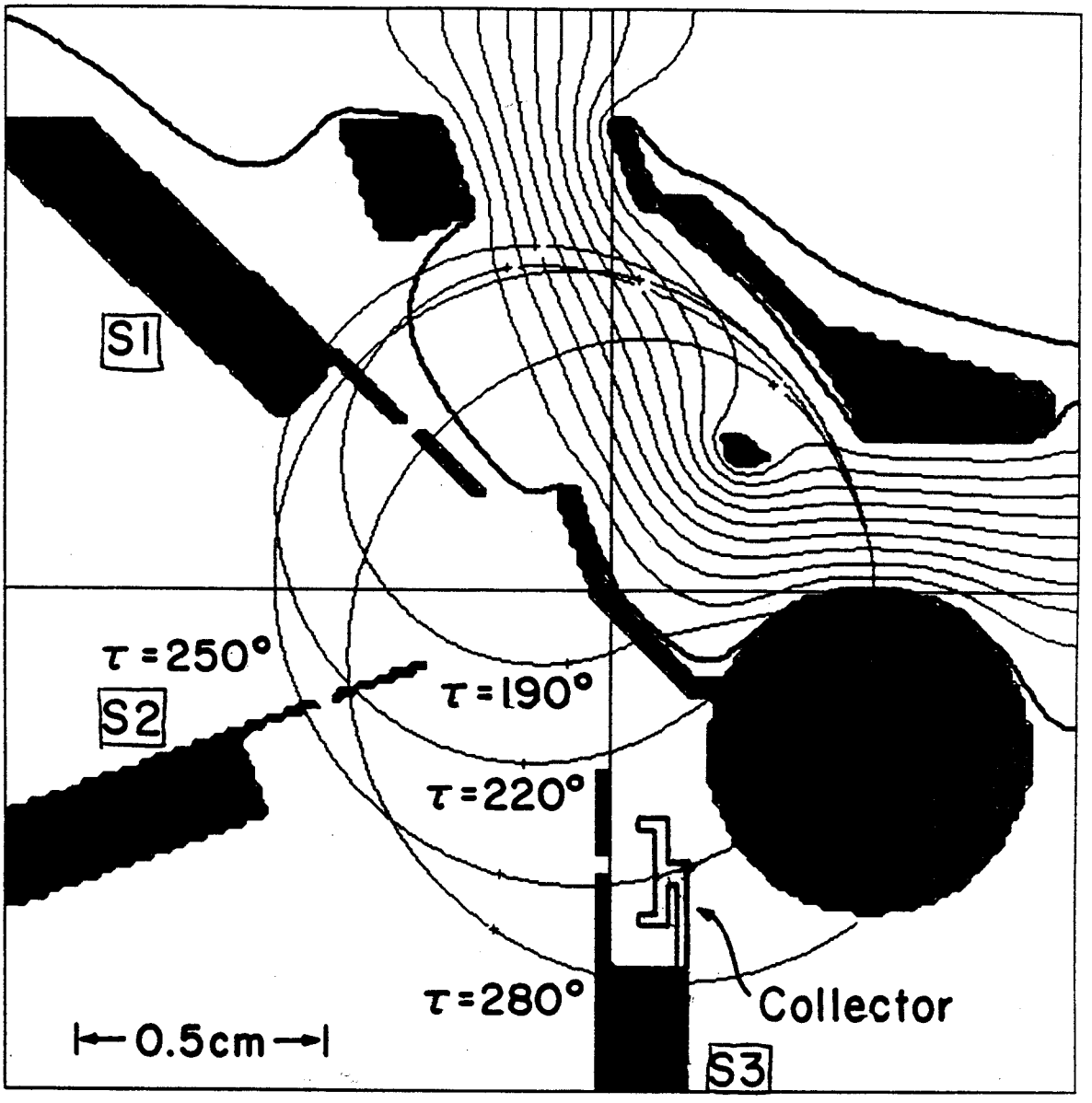

Figure A.1: A central region designed to measure the source emittance under the rf extraction. The orbits of D^+ are started with four different rf phases with 250 eV initial energy in an 8 tesla flat field. The three slits are shown in the ground region, which are approximately evenly spaced.

Table A.1: The initial conditions used for orbit calculations in Figure A.2 & 3: initial energy (E_i), source opening size, and normalized emittance, ϵ_n ($\epsilon_0\beta\gamma$)(mm·mrad). The α is the maximum incident angle of ions with respect to the normal to the source opening.

E_i(eV)	α	Opening	ϵ_n	Fig.A.2
250	±22°	0.38 mm	0.15	solid
250	±22°	0.76 mm	0.30	dash
250	±44°	0.76 mm	0.60	dot
35	±90°	0.76 mm	0.30	

in Figure A.1 for different rf starting times, using deuterons in an 8 tesla flat field. Part I of the CYCLONE program [Mar81] was modified to handle many particles and to include slit actions.

The relationship between slit coordinates and phase space in each defined rf time is needed to construct the source emittance from measuring the ion currents in slit space. For different emittances and initial conditions described in Table A.1, boundaries of rectangular source phase space are projected into the slit coordinate space as shown in Figure A.2 for starting times differing by 10°. The spread caused by larger emittance appears to include smaller ones in an orderly manner, and the ions having rf starting times differing by 10° go into fully separated regions in the slit space.

An initial ion energy (E_i) of 35 eV was then used to see the orbit distribution changes in the slit coordinate space from the 250 eV case; 35 eV, $\alpha = \pm 90°$ was chosen to keep the radial phase space area same with 250 eV, $\alpha = \pm 22°$ case as shown in Table A.1, where p_r and α are related by $p_r = \sqrt{2mE_i}\sin\alpha$. For two different initial energies, phase space projections on the slit coordinate space are shown in (a) of Figure A.3. The orbit distributions with E_i=35 eV (dashed line) are shifted to larger radii at the slit S3 than the distributions with E_i=250 eV (solid line), and more strongly focused at the slit S2. If the initial energy varies as a function of rf

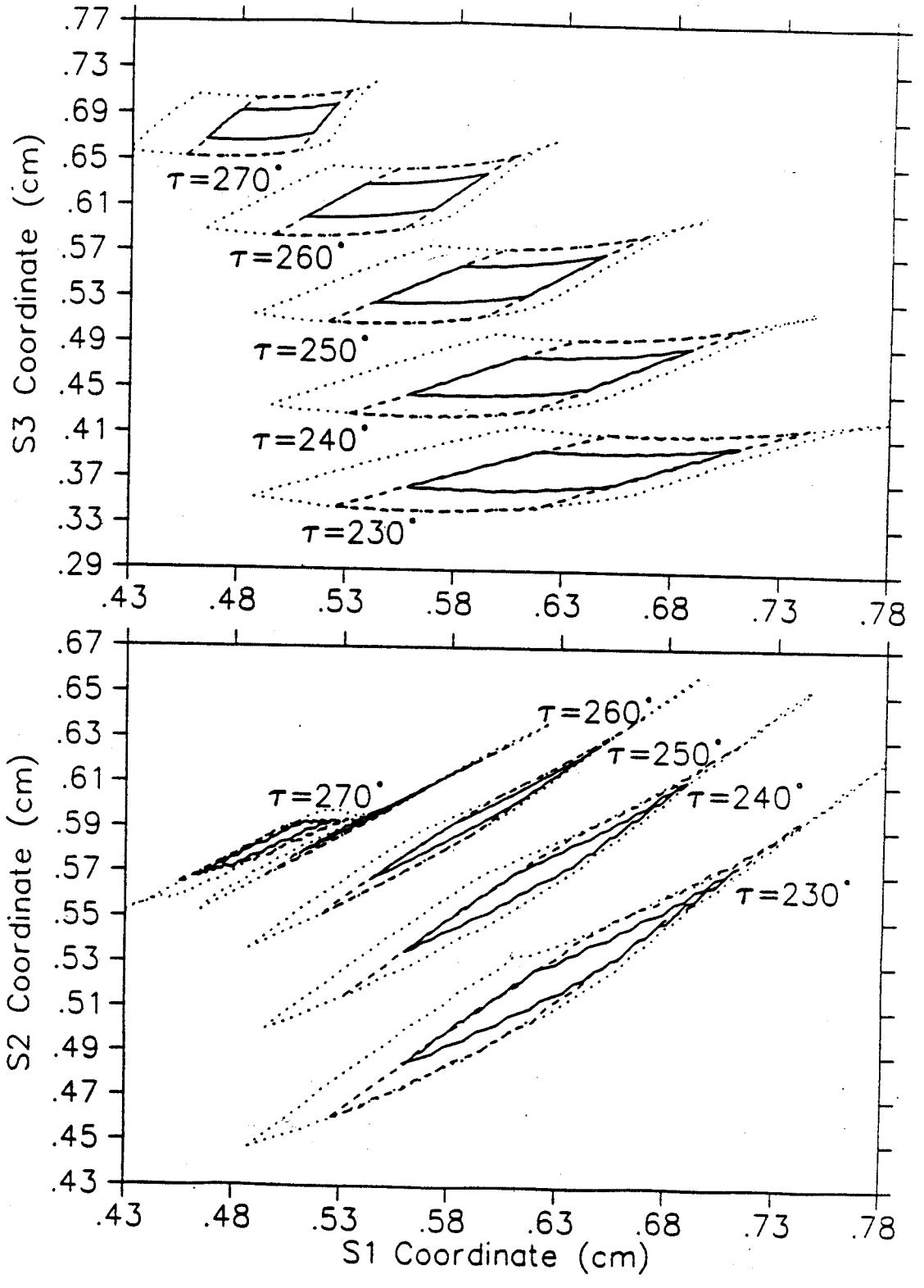

Figure A.2: Projections of rectangular initial phase spaces displayed in Table A.1 into the slit coordinate space. The emittances are separated in the slit coordinate space for rf starting times differing by 10°

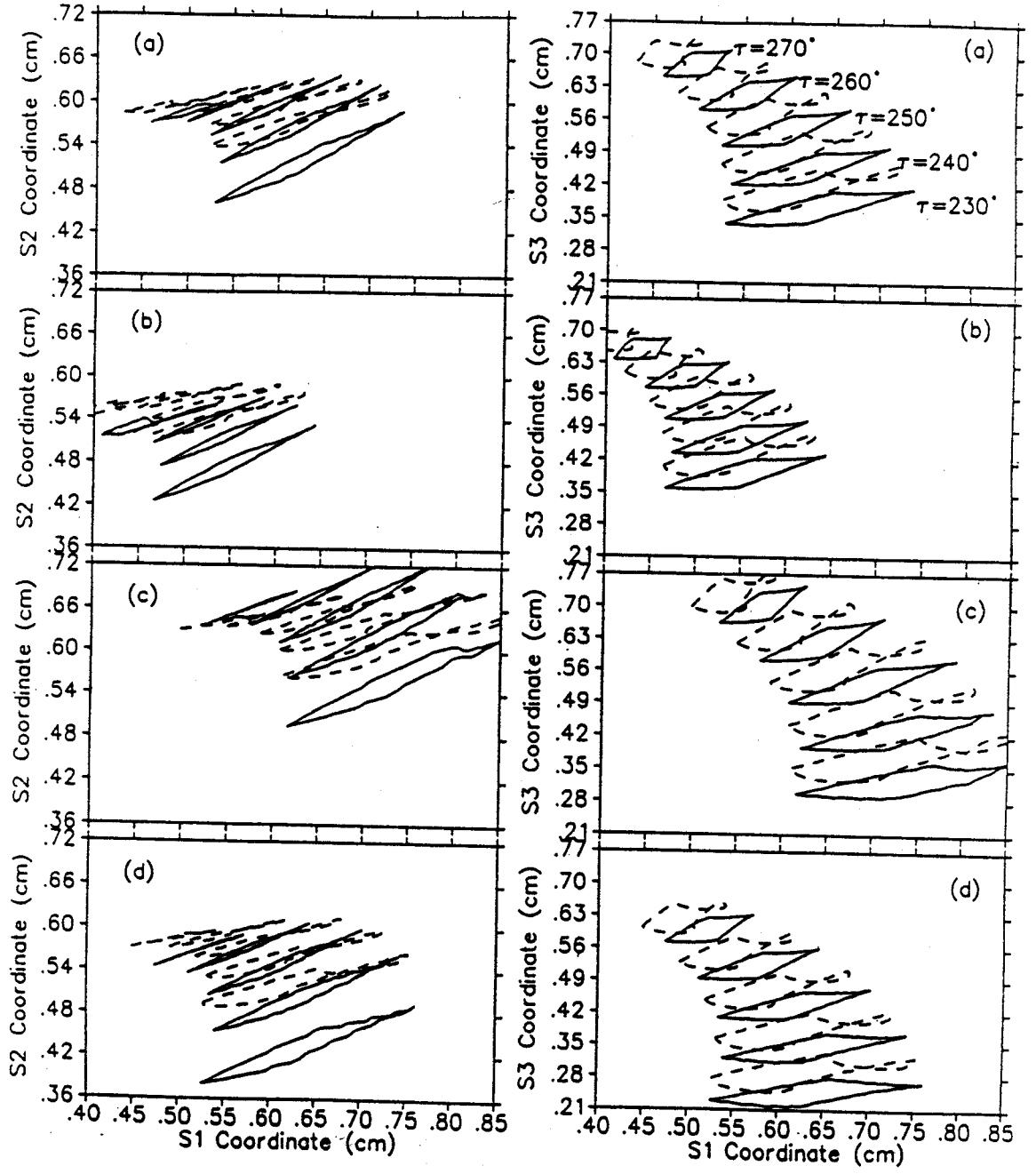

Figure A.3: Projections of rectangular phase spaces for different rf starting times into slit coordinate space with each of the three different parameters varied as described in Table A.2; a) is the case with no parameters changed, and parameter changes in b),c),d) are described in Table A.2. Two different initial energies (a solid line: 250 eV, and a dashed line: 35 eV) come from Table A.1 with the same ϵ_n(=0.30).

Table A.2: Parameter variations for the new orbit distributions in Figure A.3. One parameter is varied for each case.

Parameter	Old value	New value	Figure A.3
voltage	50 kV	45 kV	(b)
magnetic field	.8 tesla	7.5 tesla	(c)
rf frequency	61 MHz	55 MHz	(d)

starting time, the different initial energy would be difficult to separate from the orbit distributions due to the other three parameters (τ, r, p_r).

There are three parameters one can vary during measurements in a fixed central region and slit system: extraction voltage, magnetic field, and rf frequency, as displayed in Table A.2. With each of the three parameters varied, the orbit distributions are displayed in Figure A.3 for two different initial energies with the same ϵ_n (=0.3 mm·mrad) in Table.A.1. When the rf frequency is moved away from the resonance frequency by varying the magnetic field or the rf frequency itself (case (c) and (d) in Figure A.3, respectively), the orbit distributions seem to be more widely spread, especially at the slit S2, which allows a narrower slice of rf starting times. The frequency swing could be used to enhance resolution in a fixed central region configuration, but the swing range is limited by the acceptance of the puller electrodes since the puller is optimized at f_0 (61 MHz at 8 tesla).

B Conclusion

Since there is no good experimental information available on ion source phase space which includes rf electric field effects, it seems to be difficult to fully optimize this measurement system. A way to tackle this problem would be to measure the source emittance with the three slit system in the present design, and then better resolution could be achieved by further optimizing the slit system after the experiments.

A.2 RF resonator for ion extraction

As part of the ion source emittance measurement system, an rf resonator was built and tested. The resonator was designed to be actually used as an ion extractor with minor modifications after finishing the test. A plan view which includes the resonator, transmission line, vacuum feedthru, etc. is shown in Figure A.4.

For source emittance experiments in high magnetic fields, a high voltage on the extractor is preferred in order to increase the initial orbit radius, which allows more space for measurement devices. A peak voltage of 50 kV seemed to be acceptable with the initial orbit radius of approximately 0.5 cm for D^+ at 8 tesla (higher voltage entails larger power loss and larger distance to the ground to sustain the voltage). Peak electric fields are greater than 150 kV/cm under the magnetic fields perpendicular to the electric fields. A pulsed rf technique [Blo92] could be utilized to test the electric field limits.

To use for the ion source emittance measurement, a simple coil-type resonator was chosen, rather than a more complicated system such as dees with dee stems. The ac circuit analysis program, RESON, developed in this lab [Vin91] was used to determine the coil dimensions with a resonance frequency (f_0) near 60 MHz. For the 14 turn coil shown in the lower part of Figure A.5, inductance and resistance were roughly calculated to be 0.7 μH, 0.29 Ω, and capacitance of each turn was assumed to be 1 pF (as a check capacitance per unit length as calculated assuming two infinite parallel wires giving 2 pF/turn [Poz90]).

With these inputs, RESON computed the f_0 and power loss of the distributed circuit displayed in the upper part of Figure A.5, and the results are tabulated in Table A.3. The last row of Table A.3 shows the measured f_0 and Q value of the actual resonator, comparing with RESON calculations. The test resonator has only 8 turns

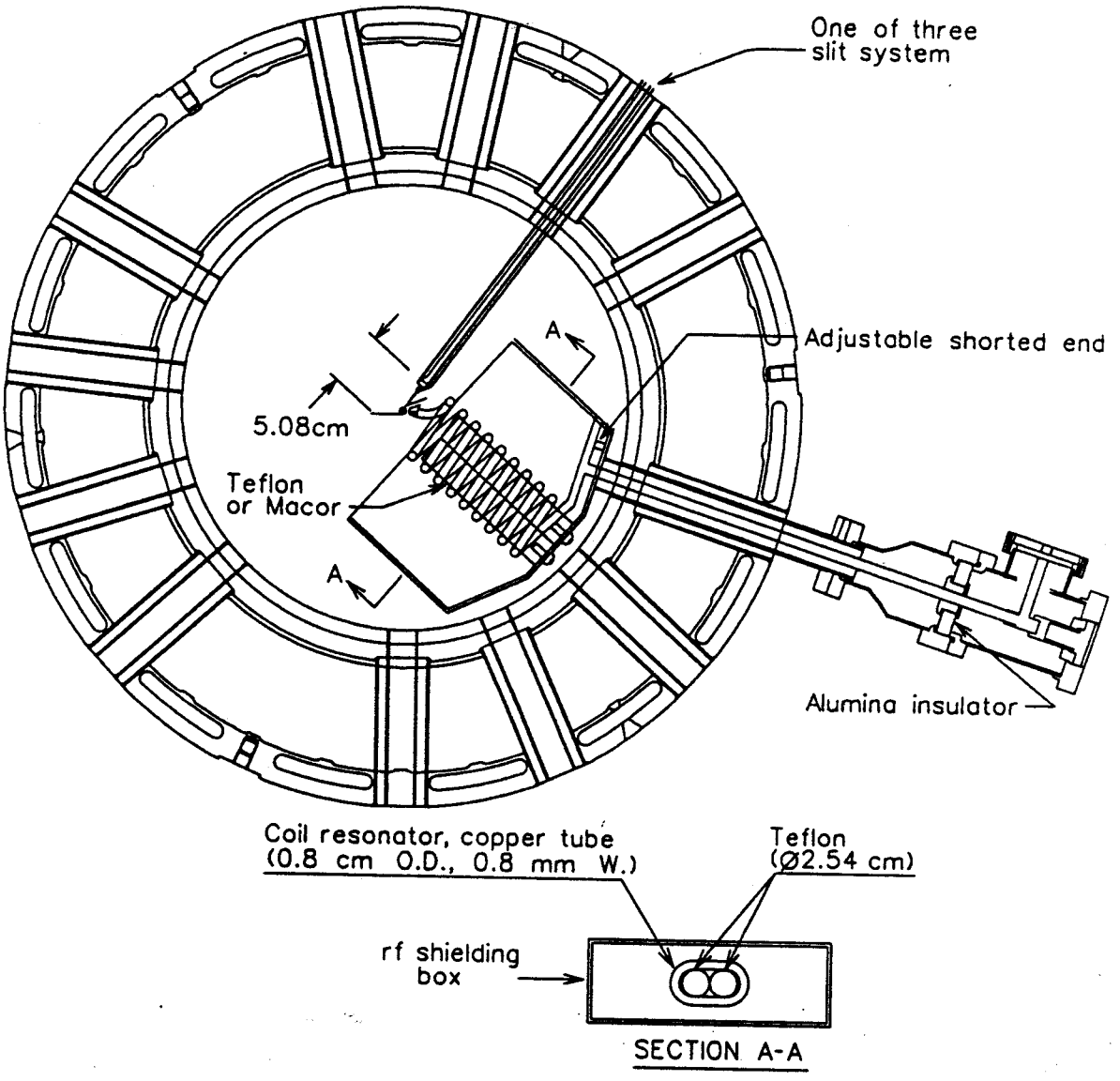

Figure A.4: A plan view for the ion source emittance measurement showing the resonator, transmission line, vacuum feedthru, one of three slits, etc. in the median plane of the 8 T magnet.

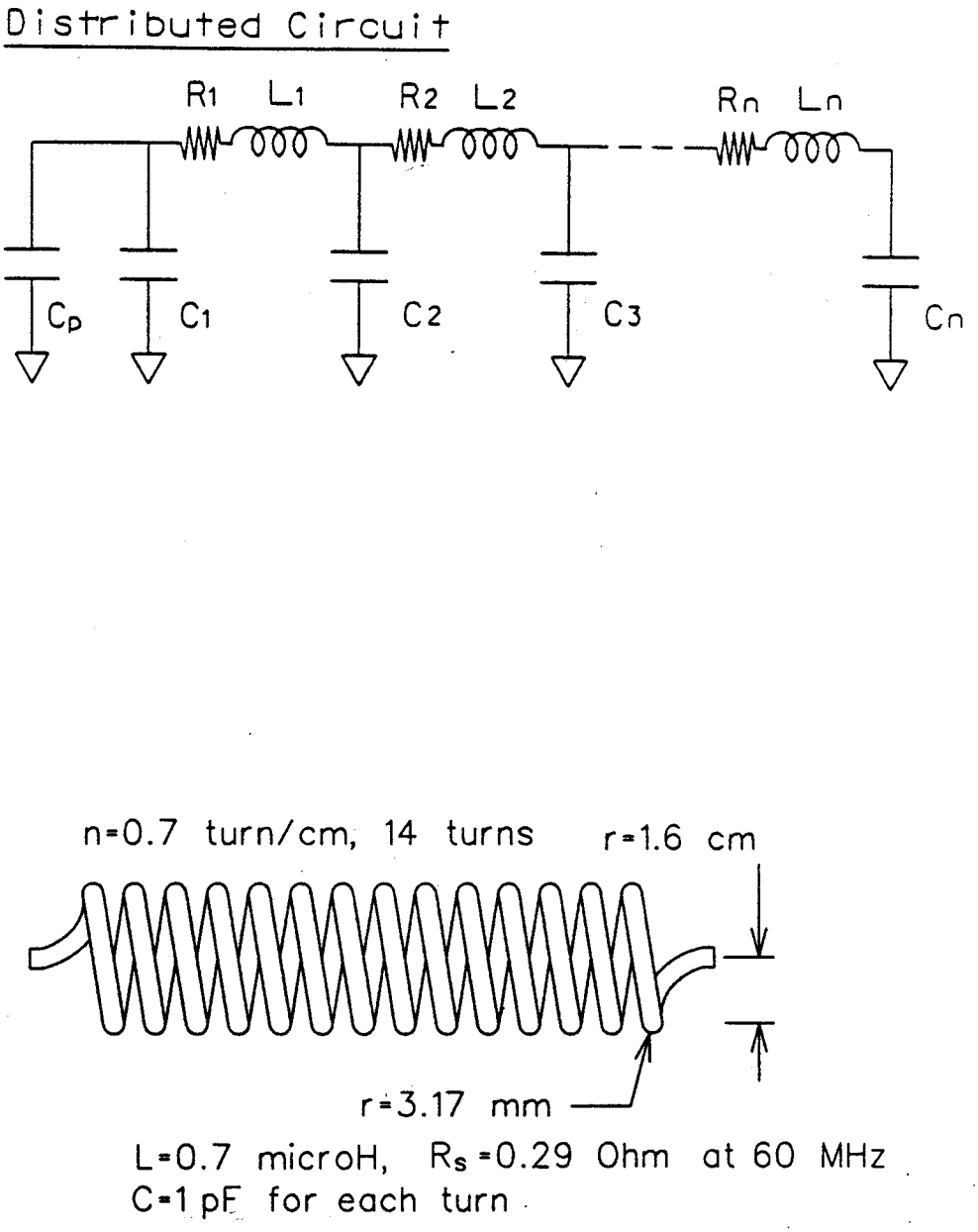

Figure A.5: The configuration of the coil resonator in the lower part of the figure, and an equivalent circuit for RESON calculations. The calculation results are given in Table A.3.

Table A.3: Ac analysis of the circuit shown in Figure A.5 with RESON. A measurement of the actual test resonator with elongated 8 turns to simulate the 14 turn coil resonator in Figure A.5., is displayed in the last row.

Circuit	Capacitance	f_0(MHz)	Power loss (kW)	Q
Distributed	C_n=1 pF, n=1~14	67.9	4.3	1020
Measurement		63.6		1200

so as to be accommodated inside the 8 T magnet (radius= 21 cm, gap height=8.1 cm), but the turns are elongated to match the total conductor (copper tube) length of the 14 turn coil in Figure A.5 as explained later in this section.

Along with computations, test resonators with different coil shapes were made, and the f_0 and Q value were measured with a vector impedance meter (HP 4815A). Since the impedance meter range was limited to 100 kΩ, Q value and resistance (R) at f_0 were obtained with Eq.A.1 [Poz90] written below, using the measured impedances (Z) and their phases (ϕ) at f near f_0.

$$R = Z\sqrt{1 + tan^2\phi}, \qquad Q = \frac{\gamma tan\phi}{1 - \gamma^2}, \tag{A.1}$$

where γ is f/f_0.

Three issues were mainly considered in designing the resonator: 1) mechanical rigidity, 2) resonance frequency (~60 MHz, at 8 tesla), and 3) coupling.

The rigidity of the coil resonator as a function of the tube diameter was investigated. The resonator was supported only at the grounded end by being soldered onto the rf shielding box wall (soldering is also for a good electrical connection). With this scheme, a tube as large as 1.27 cm O.D. could not be rigidly supported, and larger tubes are limited by the space available inside the 8 T magnet; supporting the resonator only at one end could not prevent mechanical vibrations of the free end. Since the resonator has to stay horizontal in the present plan, a supporting insulator

was added, although insulator contact to the high voltage region of a resonator in a vacuum is usually avoided because of the probable voltage breakdown through the insulator. Two Teflon rods (2.54 cm O.D.) were inserted inside the coil, and screwed to the wall as shown in Figure A.4; Teflon will be replaced by Macor to utilize the higher stiffness. In this arrangement, electric fields in the insulators are lower than when they support the coil from the outside.

To study the dimensional effects of the coil resonator on the resonance frequency, different tube sizes and lengths were tested and the results are displayed in Table A.4. In the test, the coil was installed into a copper box which is similar to the rf shielding box in Figure A.4. It was observed that a quarter wavelength of the f_0 is about 5-10% shorter than the actual tube length, which occurs due to capacitive loading. Because of the space problem again, the maximum coil turn number was limited to approximately eight with use of a 0.8 cm O.D. tube. The turns had to be elongated to acquire the length needed to maintain the f_0.

The resonator assembly in the final design was installed into a rectangular vacuum box (61×30×38 cm). The vacuum was kept better than 1×10^{-5}. The resonance frequency and Q value were then measured using a 100 W solid state rf amplifier (ENI 3100L), and later using the K500 rf system. (The K500's rf system was temporarily used for the test. This system however could not be used for future emittance experiments as the rf system will be needed for the coupling project between K500 and K1200 cyclotrons.) The block circuit diagram is displayed in Figure A.6. The f_0 was around 65 MHz in the initial test, which is close to the upper limit of the K500 rf system; the frequency limit of the rf system with a $3/4\lambda$ mode in the rf cavity is about 65 MHz unless some modifications are made to the capacitor or inductor [Mal87]. The f_0 was reduced to 63 MHz by increasing capacitance at the high voltage end, in fact simulating the ion source.

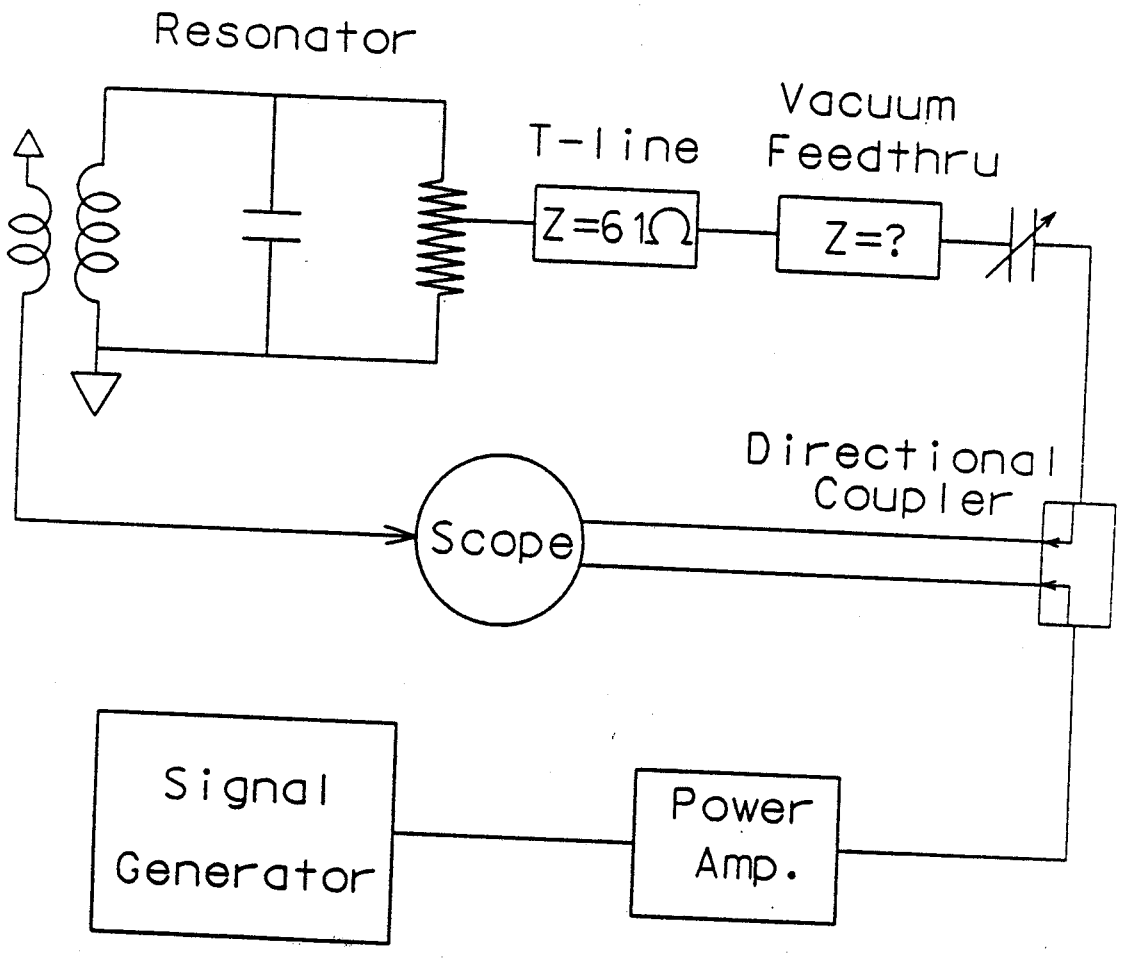

Figure A.6: A circuit diagram for testing the resonator. The power amplifier was an 100 W solid state model in the initial test, and later the K500 rf system was used.

Table A.4: Resonance frequency depending on the coil dimensions.

Tube O.D. (cm)	Tube length(cm)	f_0(MHz)	λ /4(cm)
0.64	170	46.8	160
0.78	223	35.9	209
1.3	134	60.9	123

An inductive coupling between the resonator and the transmission line was considered, which could be realized by loops often employed for cavity excitations. However, the mechanical mechanism needed to adjust the loop location was too complicated to be implemented for the test resonator. A direct contact coupling was then chosen. Since the characteristic impedance of the transmission line (Z_0) was 61 Ω (coaxial tubes with the inner tube of 0.95 cm O.D., and the outer tube of 2.61 cm O.D.), it was necessary to find the same impedance point on the resonator at f_0. The resonator impedance at the coupling point (Z_L) was calculated by measuring Z_{in} at the end of the transmission line with the resonator coupled, using the transmission line impedance equation below (see p.79 of [Poz90]),

$$Z_L = Z_0 \frac{Z_{in} - jZ_0 tan\beta l}{Z_0 - jZ_{in} tan\beta l}, \tag{A.2}$$

where $\beta = \frac{2\pi}{\lambda}$, and l is the length of the transmission line. By adjusting the location of the shorted end of the resonator (see Figure A.4), the coupling impedance was matched to 61 Ω (±1 Ω) at 63 MHz.

Some impedance mismatches on the transmission line occur in the vacuum feedthru and in the cooling water outlet sections. This effect was however neglected since that section length was short (25 cm) compared to a quarter wavelength of the f_0 (120 cm). For fine tuning, an adjustable matching element, a variable capacitor, is serially connected between the transmission line and the 50 Ω coaxial line from the rf amplifier as shown in Figure A.6.

The resonator was tested first with low power. With a 1.6 W forward power, 1 mW was reflected, and the reflected wave was spectrum analyzed. The second harmonic component was the largest when the impedance was well matched. The resonator was tested up to 80 W at which the peak voltage is estimated to be 6 kV. (The K500 rf amplifier was used a few times with low power, but the power higher than 100 W was not successfully tested.) Higher power tests would continue if the project to measure the ion source emittance is resumed (~5 kW for 50 kV).

Appendix B

Conversion of the 8 T magnet to a cyclotron

A conversion of the 8 T magnet to a cyclotron was planned after the magnet was successfully tested, and a design study was performed. The 8 T magnet was assumed to become a single ion and fixed energy cyclotron.

The deuteron (D^+) which is often employed to produce neutrons for cancer therapy by (d,Be) reaction [Blo89], was used as a projectile in the present calculations. However, computations revealed difficulties in achieving good axial focusing when such a light ion is accelerated in an 8 tesla average field. The central magnetic field was reduced to 7.2 tesla to enhance the axial focusing and to increase the initial orbit radius.

The central region of the 8 T magnet with a PIG (Penning Ion Gauges) source was designed to accelerate D^+ at h=3. Because of the desire to utilize the full magnetic field produced from the 8 T magnet and to ease the cyclotron design and construction, He^+ has lately been considered as a design ion.

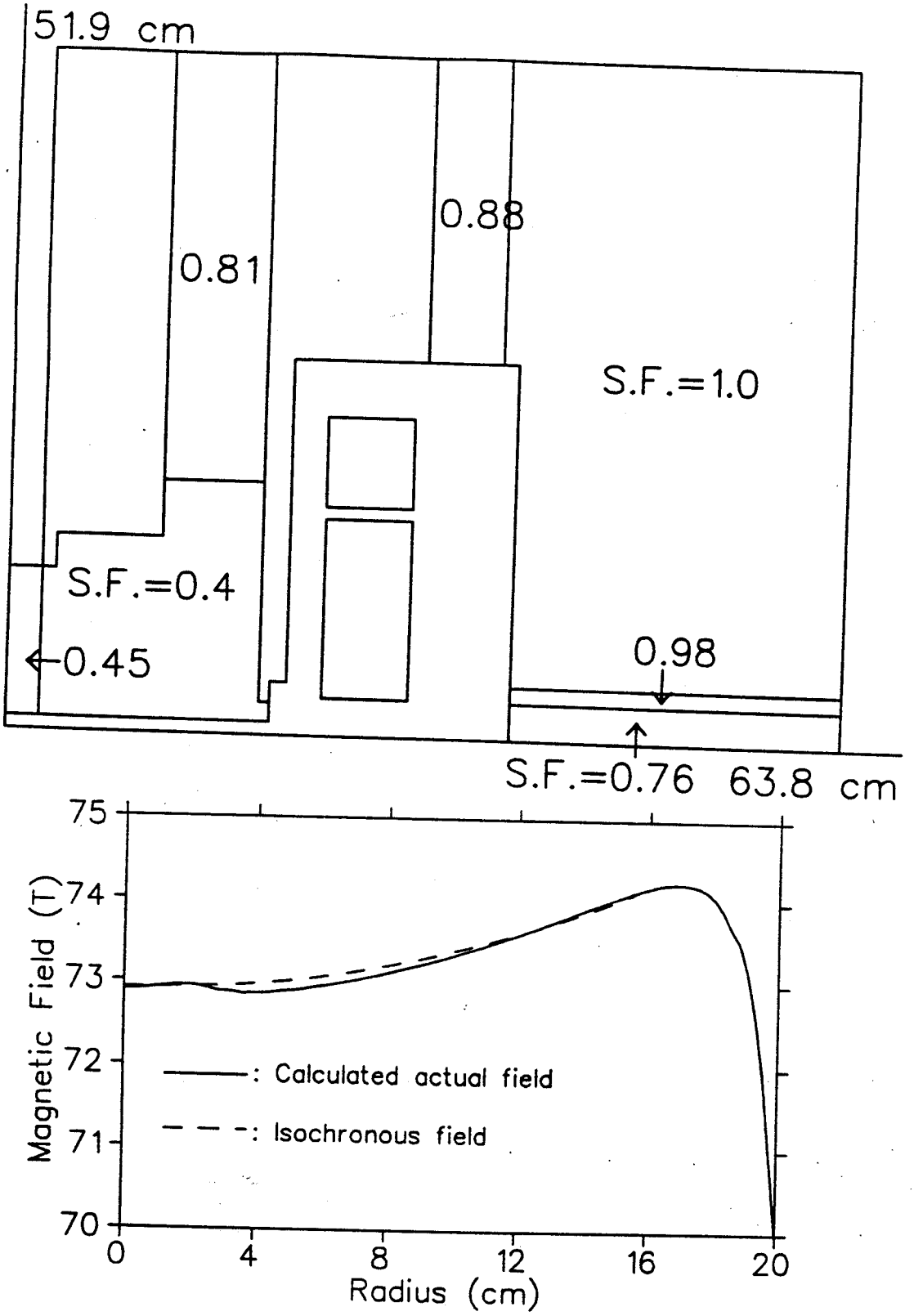

Figure B.1: The configuration of the 8 T magnet as a cyclotron to accelerate deuterons at a central field of 7.29 T. Stacking factors of each iron region used for POISSON calculations are shown in the figure. The computed magnetic field is compared to a prefect isochronous field.

B.1 Magnetic fields

The 8 T magnet configuration with Bρ= 1.2 T·m for accelerating D^+ is shown in Figure B.1. The sector structure in the pole tips is formed by contouring hills and valleys as in other isochronous cyclotrons. The lower part of Figure B.1 displays computed and perfect isochronous magnetic fields; a finer field profiling is usually accompanied by full field mapping. As the yoke already has three rf holes, three-sector structure was assumed without considering different sector number effects on focusing characteristics (see [Blo74]). The magnetic fields were calculated using the same method that has been used for designing other MSU cyclotrons; the program POISSON calculates the average field, and the current sheet program calculates the azimuthal field profile assuming saturated pole tips [Gor80].

Figure B.2 shows the contour map of the total field in the median plane. The spiral structure of hills and valleys is clearly visible. Focusing frequencies of the isochronous field, ν_r,ν_z, were calculated with the EO code [Gor84], and are plotted in the lower part of Figure B.2 as a function of energy.

B.2 Central Region

The central region of the 8 T magnet was designed to accelerate D^+ in the third harmonic of the cyclotron frequency ($\omega_{rf} = 3\omega_{cy}$, f_{cy}= 55.56 MHz at 7.29 tesla). For the orbit code, electric fields in the central region were calculated with the program RELAX3D [Kos], and the isochronous magnetic field obtained in the previous section was used. The ion source chimney has a diameter of 3.2 mm, which is only a half as large as that of the Harper hospital cyclotron. (the Harper cyclotron design significantly influenced this design study because of the similarities in operation mode; h=3, 30 kV at 4.5 tesla). The reduction of the source chimney size was necessary to

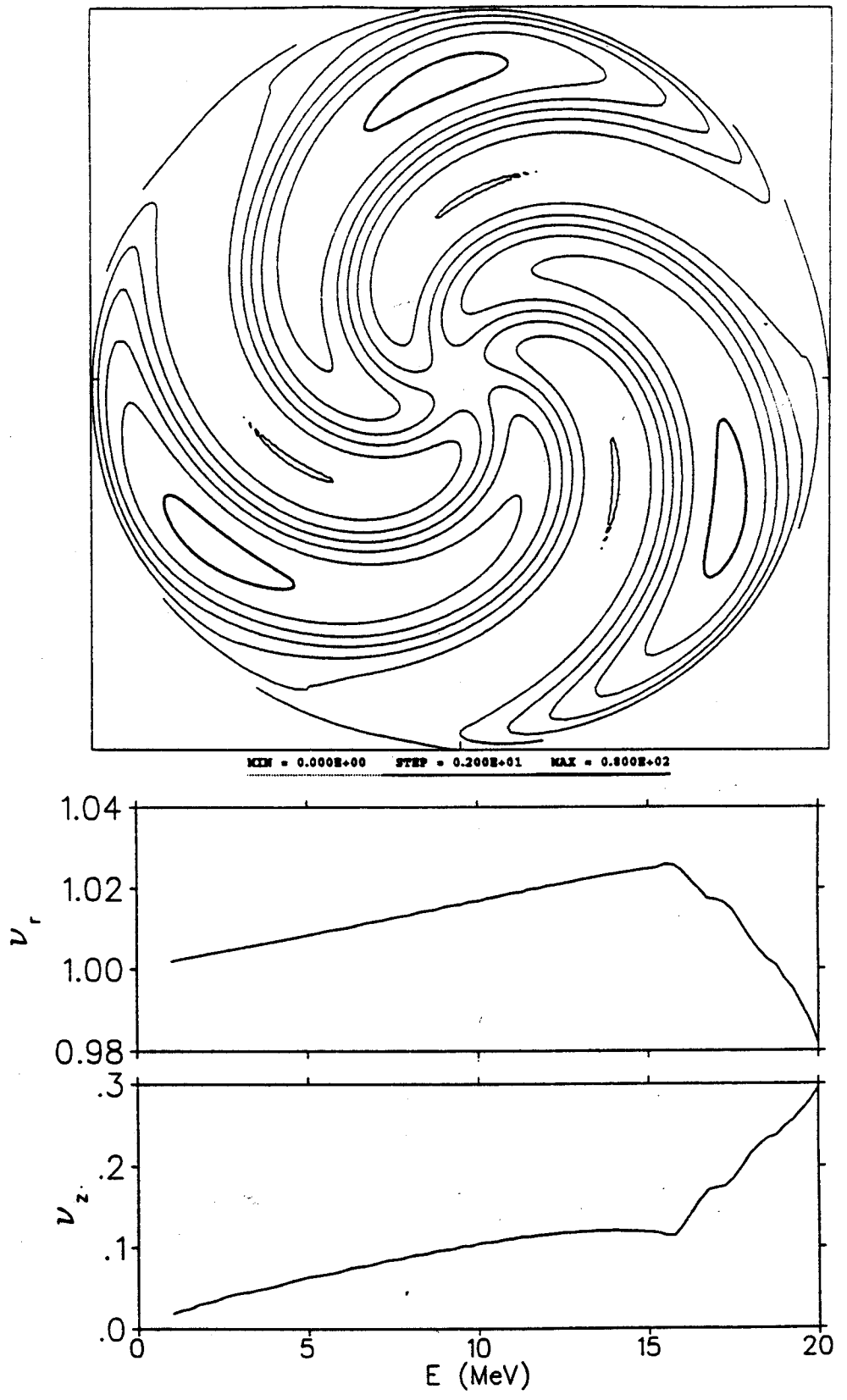

Figure B.2: (Top) Contour map of the field in the median plane. The maximum field at the hill is about 8.1 tesla. (Bottom) The focusing frequencies of the isochronized field.

clear the orbits and to accommodate the acceleration voltage of 50 kV at 7.2 tesla without increasing the maximum electric field beyond 150 kV/cm.

The orbits in the central region were calculated using the CYCLONE program. The starting time (τ_0) of the roughly centered ray is 220° (the peak rf voltage is at 270°, and the initial energy is assumed to be 100 eV). The orbits starting at τ_0 together with $\tau_0 \pm 10°$ are shown in Figure B.3. The energy gain in the first few turns is efficient so that the ions pass through the central region as quickly as possible.

III Conclusion

Design studies of the 8 T magnet conversion to a cyclotron are presented. At a central field of 7.29 tesla, axial focusing for D^+ is provided with large spirals in the sector structure, and the central region is designed to operate at h=3. Since the 8 T magnet was not designed to extract beam out of the magnet, extraction mechanisms were not studied. When the design ion is fully decided, further field shaping and orbit calculations will follow.

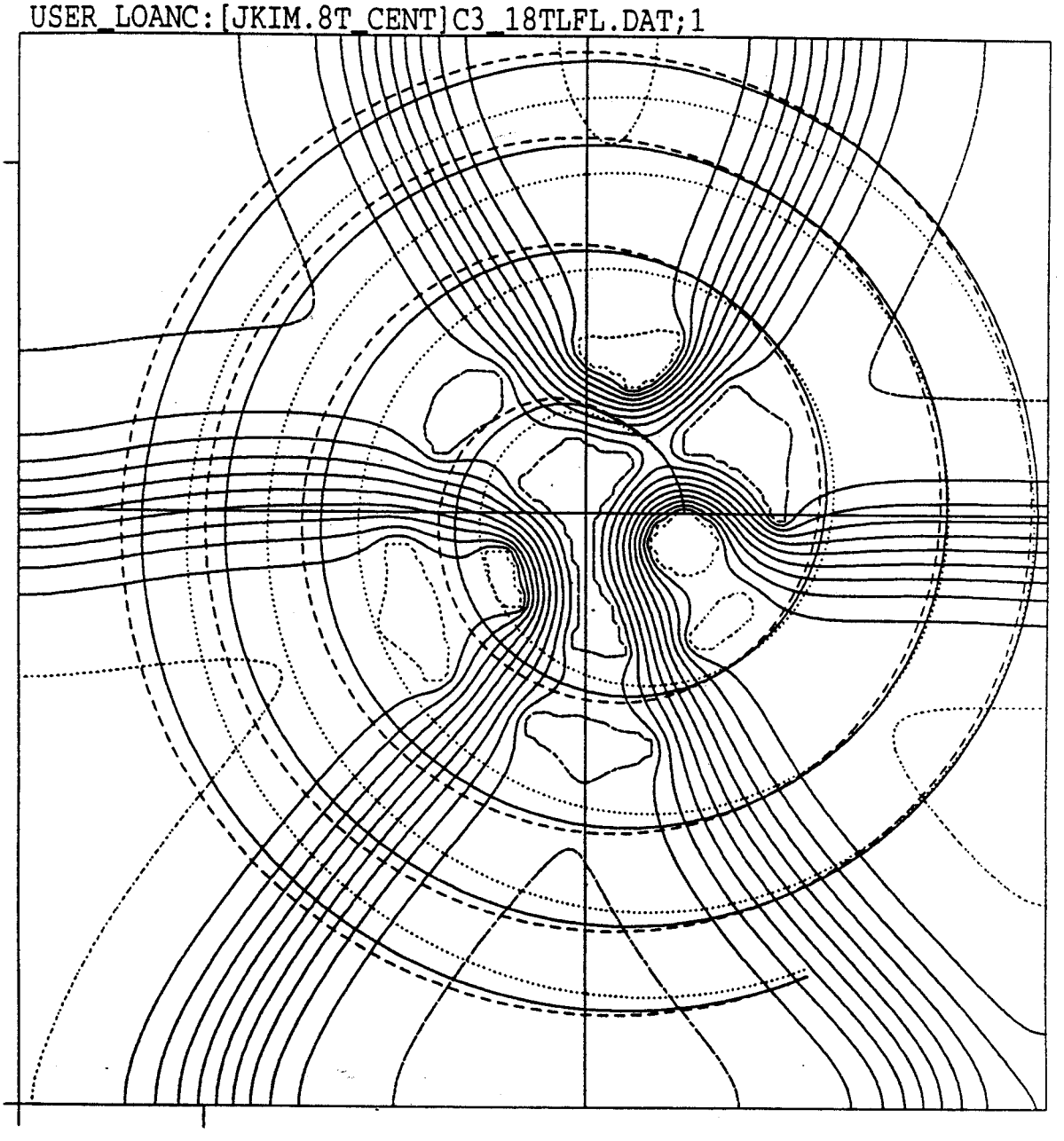

Figure B.3: Central region of the 8 T magnet designed to accelerate D^+ at h=3 in the central magnetic field of 7.29 tesla. The starting rf phase is 220° along with 210° and 230°, represented by solid, dashed and dotted lines, respectively

Bibliography

[Ago86] AGOR Cyclotron Design Report (1986), Orsay, France

[Als] SCOK 28k, Alsthom Intermagnetics (France), many other products also have similar critical current densities.

[Ame] from catalog of American Magnetics, Inc., Oak Ridge, TN

[Ant89] T. Antaya and A. Zeller, et al., Magnetic structure for a superconducting variable frequency electron cyclotron resonance ion source, IEEE Trans. on Mag. V.25, No.2, 1671 (1989)

[Ava87] E. Avallone, et al., Mark's Standard Handbook for Mechanical Engineers, Mcgraw-Hill Book Company (1987)

[Bai89] J. Bailey, et al., Central region studies for the Harper hospital cyclotron NSCL Ann. Report, 170 (1989)

[Ban91] H. Bansemir and O. Haider, Basic material data and structural analysis of fiber composite components for space application, Cryogenics V.31, 298 (1991)

[Ben72] J. R. J. Bennett, A review of PIG sources for multiply charged heavy ions, IEEE Trans. on Nucl. Sci., NS-19, No 2, 48 (1972)

[Blo63] H. Blosser, M. Gordon, and M. Reiser, Central-region studies for the MSU cyclotron, International Conference on Sector-Focused Cyclotrons and Meson Facilities, CERN 63-19, 193 (1963)

[Blo74] H. Blosser and D. Johnson, Focusing properties of superconducting cyclotron magnets, Nucl. Instr. and Meth. V.121, 301 (1974)

[Blo89] H. Blosser, et al., Superconducting cyclotron for medical application, IEEE Trans. on Mag. V.25, No.2, March, 1746 (1989)

[Blo92] H.G. Blosser, et al., Performance of the Harper Hospital Cyclotron; effect of pulsed radio frequency, Proceedings of the 13th international conference of cyclotrons and their applications, 133 (1992)

[Bob85] E.S. Bobrov, Experimental and theoretical investigation of mechanical disturbances in epoxy-impregnated superconducting coils, Cryogenics, V.25, 307 (1985)

[Bub] Bubble Chamber Group, BNL

[Com88] C. Commeaux, Status report on the design of the superconducting coil system for the AGOR cyclotron project, IEEE Trans. on Mag., V.24, No.2, March, 1323 (1988)

[Coo85] R. Cook and W. Young, Advanced Mechanics of Materials, Macmillan Publishing Company (1985), pp 91

[Cyc92] Proceedings of the 13th International Conference of Cyclotrons and their Applications, 852 (1992) Macmillan Publishing Company (1985), pp 91

[Dek] J. DeKamp, private communication

[Des79] H. Desportes, J. Le Bars, and G. Mayaux, Construction and test of the cello thin wall solenoid, Adv. Cryo. Eng., V.25, 175 (1979)

[Dev89] A. Devred, Quench characteristics of full-length SSC R&D dipole magnets, SSCL-234 (1989)

[Dev90] A. Devred, Quench origins, SSCL-255 (1990)

[Dre82] L. Dresner, Quench energies of potted magnets,III, Adv. Cryo. Eng. V.31, 365 (1981)

[Ecr] J. Moskalik, SC-ECR fiberglass link testing, NSCL, (1990) not published.

[Fro40] M. Frocht and H. Hill, Stress concentration factors around a central circular hole in a plate loaded through pin in the hole, Journal of applied mechanics, V.17, No.1, PA-5, March (1940)

[Ger90] J. Gere and S. Timoshenko, Mechanics of Materials, PWS-KENT Publishing Company (1990)

[Gor80] M.M. Gordon and D.A. Johnson, Calculation of fields in a superconducting cyclotron assuming uniform magnetization of the pole tips, Particle Accelerators, V.10, 217 (1980)

[Gor84] M. Gordon, Computation of closed orbits and basic focusing properties for sector-focused cyclotrons and the design of 'Cyclops', Particle Accelerators, V.16, 39 (1984)

[Gre81] M.A. Green, et al., Ground plane insulation failure in the first TPC superconducting coil, LBL-12326 (1981)

[Gre84] M.A. Green, Quench back in thin superconducting solenoid magnets, Cryogenics, January, 3 (1984)

[Hag29] B. Hague, The principles of Electromagnetism Applied to Electrical Machines (originally Oxford University Press) Dover, New York (1929) Handbook, Society for Experimental Mechanics Inc. (1992)

[Han92] R.L. Hannah and S.E. Reed, Strain Gage User's Handbook, Society for Experimental Mechanics Inc. (1992)

[Haw90] D.C. Hawksworth, Development of superconducting magnet systems for MRI, Adv. Cryo. Eng., 529 (1990)

[Hum89] G.Humenik, et al., K1200 magnet status: Inductance measurement, temperature effects and modifications, NSCL Ann. report, 199 (1989)

[Ish87] A. Ishiyama, Shape optimization of iron shield for superconducting solenoid magnets, Trans. on Mag., Mag-23, No.2, March, 599 (1987)

[Jac75] J.D. Jackson, Classical Electrodynamics, John Wiley & Sons, Inc., 603 (1975)

[Joh76] N.E. Johnson, Stress analysis of inhomogeneous superconducting solenoids, Adv. Cryo. Eng. V.22, 490 (1976)

[Kad85] V. Kadambi and B. Dorri, Current decay and temperatures during superconducting magnet coil quench, Cryogenics V.26, 157 (1986)

[Kat90] H.H.J. ten Kate, et al., Development of a 10 T Nb_3Sn Twin aperture model magnet for the CERN LHC, Proceedings of the 2nd European Particle Accelerator Conference, 1157 (1990)

[Ken80] R.S. Kensley and Y. Iwasa, Frictional properties of metal insulator surfaces at cryogenic temperatures, Cryogenics, January, 25 (1980)

[Kim90] J. Kim, et al., Progress on the 8 tesla magnet, NSCL Ann. Report, 215 (1990)

[Kim92a] J. Kim, et al., Progress on the 8 tesla magnet, NSCL Ann. Report, 197 (1992)

[Kim92b] J. Kim, Experiments with the liquid helium cryovessel, NSCL Ann. Report, 201 (1992)

[Kim92c] J.W. Kim and H.G. Blosser, Plan for the ion source emittance measurement under the RF extraction, Proceedings of the 13th International Conference of Cyclotrons and their Applications, 357 (1992)

[Kim93] J. Kim, et al., Construction of 8 T magnet test stand for cyclotron studies, IEEE Trans. on Applied Superconductivity, V.3, No.1, 266 (1993)

[Kos] C. Kost, TRIUMF, U.B.C. Canada

[Kur88] K. Kuroda, et al., Quench simulation analysis of a superconducting coil, V29, 814 (1989)

[Lau] H. Laumer, private communication

[Lau83] H. Laumer, et al., The K800 coil cryostat during cooldown and steady state operation, NSCL Ann. Report, 244 (1983)

[Lec86] Lecture Notes of 1986 RCNP Kikuchi Summer School on Accelerator technology, Osaka, 39 (1986)

[Leu85] E.M. Leung et al., Techniques for reducing radiation heat transfer between 77 and 4.2 K, Adv. in Cryo. Eng., V.25, 489 (1985)

[Mal87] M.L. Mallory, et al., K500 rf limit studies, NSCL Ann. Report, 148 (1987)

[Mar81] F. Marti, et al., Design calculations for the central region of the NSCL 500 MeV superconducting cyclotrons. 9th International Conference on Cyclotron and their Applications, 484 (1981)

[MeB] K.H. Meβ and P. Schmuser, Superconducting accelerator magnets, DESY, Germany

[MeB87] K.H. Meβ, Quench protection at HERA, Proceeding of the 1987 Particle Accel. Conf., 1474 (1987)

[Men87] M.T. Menzel, H.K. Stokes, Poisson/Superfish Group of Codes, Los Alamos Nat'l Lab (1987)

[Mil78] P. Miller, et al., Centering of the coil and the cryostat in the K500 magnet, NSCL Ann. Report, 117 (1978)

[Moo84] F. Moon, Magneto-Solid Mechanics, John Wiley & Sons, Inc., 260 (1984)

[Nie93] P.C. Niemann, Y.S. Cha, and J.R. Hull, Performance measurements of superconducting current leads with low helium boil-ff rates, IEEE Trans. on applied superconductivity, V.3, No.1, March, 392 (1993)

[Nuc] Physics through the 1990s, Nuclear Physics, National Academic Press (1986)

[Poz90] D. Pozar, Microwave Engineering, Addison-Wesley Publishing Company Inc. (1990)

[Pur] J. Purcell, Advanced Cryo Magnetics Inc., private communication with H. Blosser

[Ree83] R.P. Reed and A.F. Clark ed., Materials at Low Temperatures, American Society for Metals, 496 (1983)

[Shu86] Q.S. Shu, R.W. Fast, and H.L. Hart, Adv. Cryo. Engr., V31, 455 (1986)

[Spa] from catalog of Spaulding Composites Co.

[Sty] Stycast is a product of Emerson and Cuming Inc.

[Tom72] M. Toman and M. Reiser, Emittance measurements for N^+ and N^{2+} in an ion beam from a cyclotron ion source, IEEE Trans. on Nucl. Sci., NS-19, No.2, 80 (1972)

[Tos] Vector Fields Limited, England

[Tri90] U. Trinks, Superconducting cyclotrons, Nucl. Instr. and Meth., A287, 224 (1990)

[Ued93] K.Ueda, et al., Design and testing of a pair of current leads using bismuth compound superconductor, IEEE Trans. on applied superconductivity, V.3, No.1, March, 400 (1993)

[Ura89] M. Urata, et al., Stabilization of superconducting dry solenoids, IEEE Trans. on Mag., V.25, No.2, 1528 (1989)

[Vin91] J. Vincent, et al., PC RESON: radio frequency circuit analysis for PC's, NSCL Ann. Report, 204 (1991)

[Wil68] M. Wilson, program QUENCH, Rutherford Laboratory Report, RHEL/M151 (1968)

[Wil83] M. Wilson, Superconducting Magnets, Oxford University Press (1983)

[Wu91] J.L. Wu, et al., Design and testing of a high temperature superconducting current lead, IEEE Trans. on Mag., V.27, No.2, March, 1891 (1991)